The Dissertation Committee for Nima Dabidian Certifies that this is the approved version of the following dissertation :

Active Graphene Metasurfaces for Optoelectronic Applications

Committee:

Gennady Shvets, Supervisor

Michael Downer

Xiaoqin Li

John Keto

Andrea alu

Active Graphene Metasurfaces for Optoelectronic Applications

by

Nima Dabidian, BSc; MSc

Dissertation

Presented to the Faculty of the Graduate School of
The University of Texas at Austin
in Partial Fulfillment
of the Requirements
for the Degree of

DOCTOR OF PHILOSOPHY

The University of Texas at Austin
May 2016

Dedication

Dedicated to my parents who are the center of my universe and
my wife who inspires me to be a better person every day even from
thousands of miles away.

Acknowledgements

I would like to thanks my supervisor Professor Gennady Shvets for his advices, encouragement and un-ending support over these years. I am also grateful to Professor Mikhail Belkin for giving me access to his lab and guiding me throughout the collaborative works.

Special thanks to Alexander Khanikaev for interesting ideas he brought to our lab and his unfailing support during these years.

I would like to thank my colleges Chih Hui Wu, Hossein Mousavi, Nihal Arju, and Maz, Jongwon Lee, Feng Lu and Mingzhou Jin for the interesting discussions and supports during all these years.

The experimental accomplishments in this dissertation would not be possible without the deep device knowledge of Babak Fallahazad who always made himself available.

Active Graphene Metasurfaces for Optoelectronic Applications

Nima Dabidian, PhD
The University of Texas at Austin, 2015

Supervisor: Gennady Shvets

Abstract:

Plasmonic metasurfaces are optical components that enhance the light-matter interaction and can control the flow of light. The scalability and universality of the metasurface design enables their deployment across the entire electromagnetic spectrum. Especially attractive are the metasurfaces designed to operate in the mid-infrared part of the optical spectrum. That is due to two factors: the variety of technological applications and the limited choice of conventional optical components in the mid-IR spectral region.

Graphene has emerged as a promising optoelectronic material because its optical properties can be rapidly and dramatically changed using electric gating. In particular in the mid-IR regime, graphene has plasmonic properties and can be utilized as a tunable inductor for active modulation of the light with an ultra-fast rate. However graphene's weak optical response, especially in the infrared part of the spectrum, remains the key challenge to developing practical graphene-based optical devices such as modulators, infrared detectors, and tunable reflect-arrays.

In this thesis, we take advantage of plasmonic metasurfaces to enhance the light interaction with graphene for crucial optoelectronic applications. The ability to modulate light at a high-speed is an important part of modern communication systems. We use the plasmonic properties of graphene in the mid-IR range to spectrally shift a narrow-width Fano resonance. Using this approach, we achieve strong modulation of amplitude and phase using plasmonic Fano-resonant metasurfaces integrated with graphene. We also demonstrate that the strong spectral shift of the plasmonic resonance can be used to extract one of the key optical parameters of graphene: the free carrier scattering rate.

Another interesting branch of optics is wave-front engineering. The ability to dynamically manipulate the phase, inspires interesting applications such as beam steering and holograms. We use a Michelson interferometry to measure the graphene-induced phase modulation. In particular, we show that it is possible to modulate the phase of electromagnetic wave while the amplitude is constant. We demonstrate proof of concept application of active phase modulation in motion sensing and polarization conversion.

An emerging area of optoelectronic is ultra-fast photodetectors based on graphene and other 2-D materials. We employ Full-wave and electrostatic simulations to study the performance of a metasurface-based photodetector. Circuit analysis is utilized to provide a mathematical relation for the responsivity of the metasurface-based graphene photodetector. It is shown that electrically-connected metasurfaces can dramatically enhance the collection efficiency of graphene photodetectors.

List of Tables

List of Figures

Chapter 1: Introduction

1.1 WHY OPTOELECTRONICS?

In the recent decades there has been a lot of research and technological advance in the field of optics and electronics. Semiconductor companies now are able to manufacture small chips with billions of transistors as the basic component for processing digital electronic data. At the same time, optical fiber communication has overtaken the data transfer between continents, countries and now it`s starting to reach directly to the consumer. This has increased the speed of communication in particular internet which billions of people depend on its reliability. Therefore, optics and electronic has changed out lifestyle in dramatic ways. On the other hand, the marriage of electronics and optics has created the very important fields of optoelectronic and electro-optics. Optoelectronics is the study and application of devices that source, detect and control light which are important elements of communication systems. Similarly named field of electro-optics deals with interaction of light with materials in different electronic states for controlling and manipulation of light. The advance in electromagnetics has brought in new mechanisms to manipulate and control light to produce devices relevant to technological need. One of the most important fields which is trying to address this problem is the field of metamaterials.

1.2 FROM METAMATERIALS TO METASURFACES

Meta means beyond in Greek and metamterial is a material with engineered optical properties that does not exist in naturally found materials. This field started in 1999 when Pendry et al. for the first time showed that it possible to engineer a material from periodic arrangement of metallic split ring resonators that can produce negative magnetic permeability[1] $\mu < 0$. This brought up the theoretical predictions of Veselago in 1960s that simultaneous negative permeability $\mu < 0$ and negative permittivity $\epsilon < 0$ can result in material with negative refraction[2]. In 2001 Shelby et al. experimentally demonstrated that light can refract negatively in the microwave regime by an arra that combines metallic wires and split rings resonators responsible for negative ϵ and μ respectively[3]. Pendry also theoretically predicted that by a slab of metamaterial with negative index of refraction can be used as a perfect lens. The resolution of a perfect lens is not hindered by the diffraction limit [4]. This was a promising start to the field of metamaterials which boomed in the early 2000s. Later on Shalaev et. Al was able to demonstrate the negative refraction of light at the telecommunication wavelength $\lambda = 1.5\mu m$[5]. Bringing the field of metamaterials to the optical and infrared regime increased the study of plasmonics. Plasmons are collective oscillation of free electrons in response to the incident light. These oscillations give rise to surface plasmon polariton (SPP) that are surface waves confined to the surface of the metal. The confinement of the electromagnetic energy to the surface of metal can enhance light amplitude by orders of magnitude with interesting applications in biosensing and green energies. However the field enhancement comes at a price: metallic losses from electron-electron scattering which is the main obstacle for the progress of metamaterials in the optical and IR regime. Additionally, due to difficulty in nanofabrication of 3-D metamaterials, the field of metamaterial changed direction toward engineering 2-D metasurfaces [6,7] which are single-layer metamaterials. Plasmonic metasurfaces are already finding applications in a variety of areas such as light manipulation [8–15], biochemical sensing[15–17], nonlinear optics [18,19] and spectrally-selective thermal emission[20] to name just a few. Ultra-thin optical components such as optical lenses[21,22], wave-plates[23] and beam steering devices[8,24] are some of the recent examples of employing metasurfaces for molding the flow of light.

1.3 TECHNOLOGICAL OPPORTUNITIES IN THE MID-INFRARED RANGE

The scalability and universality of the metasurface design enables their deployment across the entire electromagnetic spectrum. Especially attractive are the metasurfaces designed to operate in the mid-infrared (mid-IR) part of the optical spectrum. That is due to two factors: the variety of technological applications and the limited choice of conventional optical components in the mid-IR spectral region. For example, the $2\mu m - 20\mu m$ spectral range hosts important bio-molecular and chemical fingerprints[16] that are being exploited for ultra-sensitive fingerprinting and characterization of molecular monolayers[9,12]. In addition, the atmospheric transparency windows of $3\mu m - 5\mu m$ and $8\mu m - 12\mu m$ are exploited for a variety of thermal imaging applications[25,26] . These unique properties of infrared radiation are now used to address crucial health, security, and environmental applications [14,27–30], but more rapid progress is impeded by the limited availability of passive and active mid-infrared devices and components such as sources and detectors [31–35], as well as optical modulators and switches[36–43]. This niche can be potentially filled by active plasmonic metasurfaces.

1.4 ACTIVE METASURFACES

Plasmonic enhancement of light-matter interaction improves the performance and reduces the sizes of detectors[44–46] , sensors [47–49] and lasers[50]. When integrated with electrically or mechanically tunable materials or substrates, plasmonic metasurfaces can assume the role of a versatile platform for developing dynamically tunable optical devices, thus paving the way for a variety of technological applications in hyper-spectral imaging[51], single pixel detection[52], and 3D imaging[53], as well as optical modulators and switches [36–43].

1.4.1 Response time

Active control of light required an active material with tunable index of refraction. Slow physical processes result in slow devices. Examples are materials where index change is due to change in temperature or alignment. A few examples are devices that operate based on liquid crystals[36], advanced materials exhibiting metal-insulator phase transitions[38], and mechanically stretchable elastomeric materials[54]. On the other hand, if the tunability comes from the electronic properties of material, the response could be potentially high-speed. Semiconductor interfaces controlled through electrostatic carrier depletion [40,43,55] and graphene are two important examples.

1.4.2 Semiconductors as active materials:

Semiconductors have been used as active materials to modulate the terahertz waves. By fabricating electrically connected metrasurfaces on top of a doped semiconductor, it was possible to modulate the charge carrier concentration of the semiconductor below the metasurface[55]. This can be achieved by applying a voltage between the metasurface and the doped semiconductor. This concept was also used in the mid-infrared regime but resulted in a weaker modulation[43].

1.4.3 Graphene as an active material

An emerging material is graphene, a 2-dimentional monolayer of carbon which has a linear electronic dispersion that makes it a unique material with exotic properties such as large mobility and zero energy bandgap. Graphene charge concentration can be tuned by electrostatic gating with an ultra-fast speed limited to the circuit time constant. However graphene as well as depletion type semiconductor devices have small effect in the near infrared and mid-infrared regime and an optical modulator based on these materials would have shallow modulation depth and narrow bandwidth. The limited effect of the single layer graphene (SLG) on plasmonic metasurfaces in mid-IR is due to two factors: (i) relatively broad plasmonic resonances in that spectral range [56], and (ii) weak absorption of graphene in mid-IR due to the absence of interband transitions [57]. However due to small loss in the mid-IR graphene has a plasmonic response and behaves primarily inductive in this regime[57].

In this dissertation, we use graphene as our active material and study the amplitude and phase modulation as well as detection of mid-IR light using graphene-based active metasurfaces. By integrating graphene into a plasmonic metasurface, it is possible to enhance the light-matter interaction by orders of magnitude and observe stronger modulation of amplitude and the phase and photo-responsivity.

1.5 APPLICATION OF MODULATORS AND PHOTO-DETECTORS IN HIGH-SPEED COMMUNICATION SYSTEMS

As previously mentioned, fiber optics is becoming the dominant method of the high-speed communication systems. In Fig. 1.1, the block diagram of a fiber communication system is shown which consists of a transmitter, a receiver and optical fiber as the transmission medium.

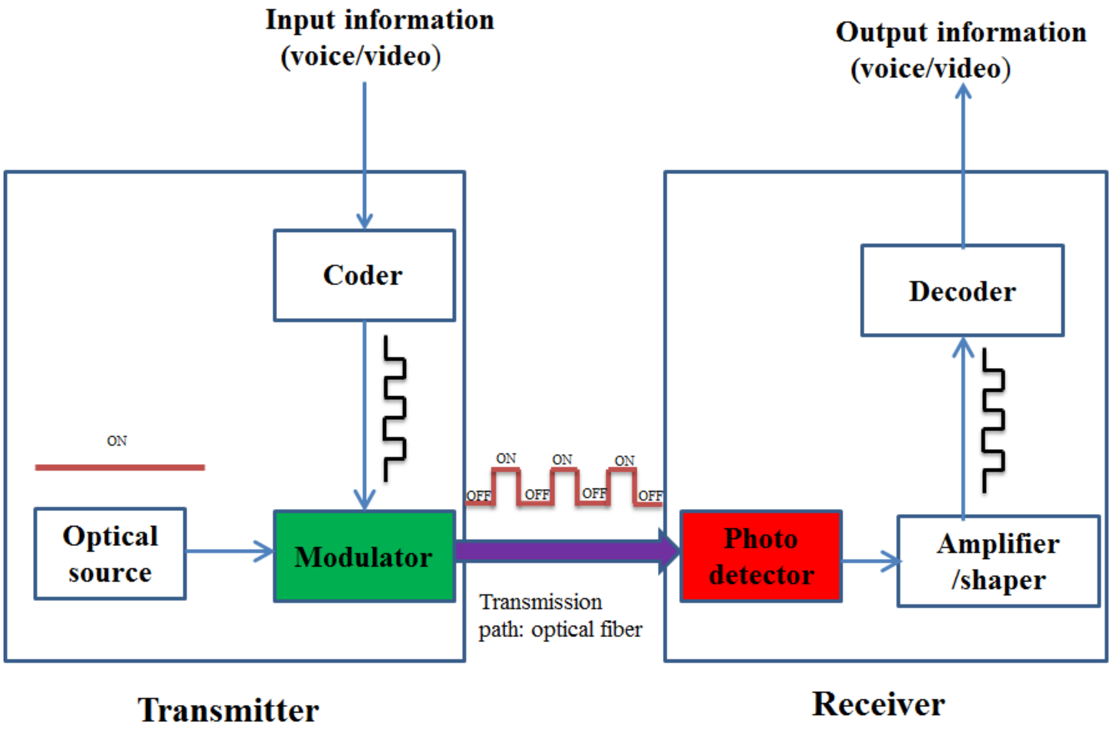

Figure 1.1: The block diagram of optical fiber communication system. A transmitter consists of an optical source, a coder and an optical modulator whereas a receiver is comprised of a photo-detector, and amplifier/shaper module and a decoder.

As the figure suggests, optical modulators and photo-detectors are the heart of the transmitters and receivers. The following summarizes data transmission on fiber optics network. First a coder, convert the analog data e.g. audio/video to digital pulses. Next an optical modulator converts the digital data (electrical) to optical pulses which transmit over the fiber and are detected by a photo-detector. The detected signal is amplified and shaped to recover the original digital data. Finally a decoder reproduces the input audio/video data.

A transceiver is a dual-purpose equipment that consists of a transmitter and a receiver. The extension of the fiber to the end-user is possible by high-speed transceivers which will boost the downstream and upstream speed of communication and internet systems dramatically.

1.6 OPTOELECTRONIC APPLICATIONS OF GRAPHENE-BASED ACTIVE METASURFACES; OPPORTUNITIES AND CHALLENGES

1.6.1 Amplitude modulators

Amplitude modulator is an important module in optical transceivers which are a necessary component of fiber communication systems. The artwork in Fig. 1.2 is an example of a graphene based active metasurface which functions as a modulator: converts the coded electrical signal (showed by green numbers) to optical pulses. A fiber is used to bring a continuous beam of light to the device as shown on the left. The device is a plasmonic metasurface integrated with graphene similar to a MOSFET transistor where the gate voltages tunes the channel (graphene) properties. The plasmonic metasurface enhances the light interaction with graphene, thereby the gate voltage can tune the light amplitude. Strong modulation allows switching of the light which can be of great interest if it is done at high-speeds of telecommunication systems.

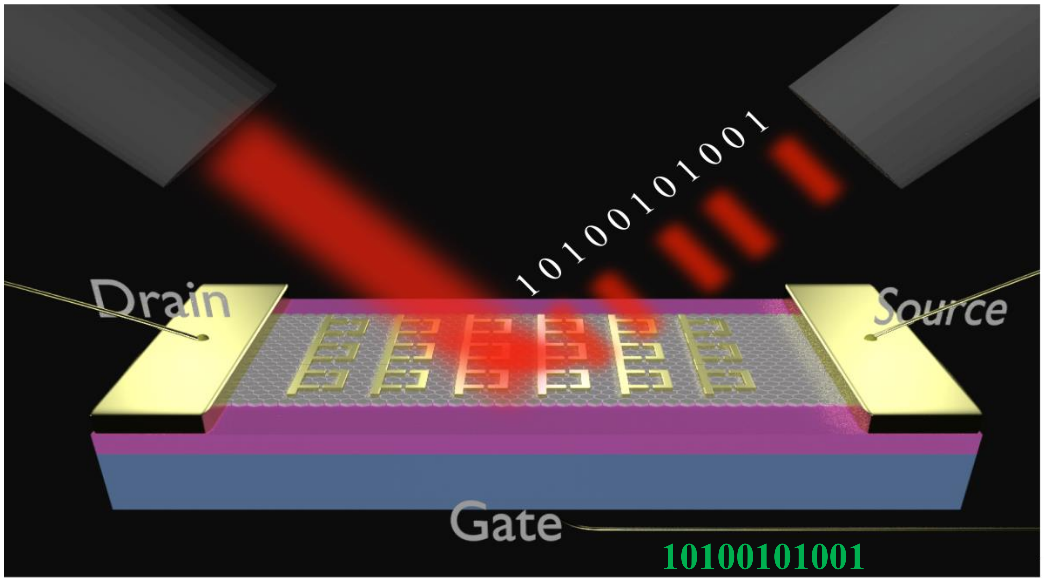

Figure 1.2: An optoelectronic device that can strongly modulate (switch) the incident light and functions as a transmitter. The device is a graphene-based active metasurface similar to a MOSFET transistor with graphene playing the role of the channel. The device functions as a transmitter that converts the coded electrical voltage of the gate (shown by green numbers) to optical pulses.

Modulators are also important in high-speed tuning of the power of a light source i.e. a laser, without altering the laser input power. It has been shown that tuning of the mid-IR light using graphene-based active metasurfaces can be broad and ultra-fast[58,59]. However the modulation depth in these works did not exceed 30% calling for new designs that allow higher modulation depth of 10dB and higher required for switching of the light.

1.6.2 Phase modulators

Another application of metasurfaces is in shaping the wave-front of the electromagnetic waves. This requires local control over amplitude and phase. Conventional optics uses propagation effect to gradually modify the light beam e.g.

metamaterials with spatially varing indices can steer and control beam in applications such as optical cloaking[3,60] and superlens[61]. Metasurfaces on the other hand are able to introduce an abrupt change in optical properties which originates from the interaction of light with subwavelength antenna arrays. These arrays can have spatially varying optical response which provides great flexibility in molding the wavefront with applications in holograms[62–66] ,beam steering[67] and optical devices such as lenses[21], axicons [68] and waveplates [23]. The recent progress on active metasurfaces is promising to bring dynamics to these applications making them more even appealing for technological use. To achieve this goal, it is necessary to use a design where the properties of the active material can be independently modulated across the array. An array of graphene ribbons with each ribbon attached to a separate voltage can be an example of in-homogenous gating of an active metasurface. But as a first step, we study active metasurfaces with homogenous gating.

Although there has been a few experimental demonstration of phase modulation in the terahertz regime using terahertz time-domain spectroscopy[55,69], to our knowledge there has been no experimental study on phase modulation using active metasrufaces in the mid-IR. Liquid crystals are the common technology for phase modulation in the mid-IR range due to their ability to induce 2π phase shift at high transmission amplitudes. However liquid crystals have several fundamental molecular vibration bands and overtones in the mid-wave Infrared $(3-8\,\mu m)$ and long-wave Infrared $(8-15\,\mu m)$ which contribute to high absorption coefficient and hinder its widespread application. More importantly, the response time of this class of active material is limited to milliseconds[70]. Therefore, graphene-based active devices can be an interesting alternative due to their high-speed potentials, lack of intrinsic absorption bands and possibility of high-transmission. However as mentioned before, graphene has weak effect in the mid-IR range. The integration of graphene to a plasmonic metasurface can potentially solve this problem. In this dissertation, we report the measurement of graphene-induced phase modulation in the mid-IR range which to our knowledge is the first time. The graphene is integrated into a plasmonic metasurface to enhance the phase modulation in the wavelength of our interest.

1.6.3 Photo-detectors

Graphene can also be used as a photoconductor. Graphene photo-detectors are interesting for two reasons (i) graphene has zero energy bandgap therefore can be utilized as a wide-band detector. (ii) photodetectors based on graphene can be ultra-fast. Several mechanism have been suggested for photodetection using graphene including photovoltaic effect[71], photo-thermoelectric effect [72], bolometric effect[73] and photogating effect[74]. I will focus on the photovoltaic effect in this dissertation that is based on separation of photo-generated electron-hole pairs by the built in electric field at the junction between n or p-doped graphene and metallic contacts. A source-drain bias can achieve the same effect through external electric field although it will generate a dark current since graphene is a semi-metal.

A single layer graphene (SLG) can absorb 2.3% of the incident light which is remarkably high for an atomically thin material. However for applications such as photodetectors it is highly desirable to enhance the absorption. SLG has been integrated into optical microcavities[75,76], planar photonic crystal cavities[42], optical waveguides[77] and plasmonic nanostructures[78] to enhance the absorption of light. In another work, the graphene plasmons on an array of nano-ribbons were employed as a photodetector due to large field enhancement that originates from the confinement of the plasmons to a graphene surface[79]. In a recent article, it was shown that a metasurface can enhance the absorption and collection efficiency of graphene photodetectors[71]. However the photocurrent generated in this work was less only 12mA/W which cannot nearly compete those achieved via graphene photo-transistors $1AW^{-1}$ [74] and regular silicon photodiodes $\approx 0.5\ AW^{-1}$(although that detects $\lambda < 1\mu m$). This calls for better metasurface designs with higher responsivities.

1.7 THE ORGANIZATION OF THE DISSERTATION

In chapter 2, I review the physics of graphene and its exotic properties. In particular the optical properties which is relevant to this dissertation will be studies in depth.

In chapter 3, Fano resonance will be discussed. Electromagnetically induced transparency as a special case of Fano resonance will be reviewed.

In chapter 4, I study amplitude modulation of mid-IR light by graphene integration into plasmonic metasurface. A Fano-resonant metasurface is used to enhance the light matter interaction. It is shown that by changing the graphene charge concentration the amplitude can modulate by 10 times resulting in 10 dB modulation depth. A new method for determining the collisional time of graphene charge is proposed which matches the results of electrical transport measurement. Substrate effect on the quality factor of the the Fano-resonant mode is studied.

In chapter 5, I use a Michelson interferometric system for measuring the phase modulation induced by an active graphene metasurface. I show that it is possible to use the device for potentially ultra-fast electrical calibration of a laser interferometric setup. Such a system can be used for high-speed motion detection. I finally demonstrate the tunable ellipticity of the reflected wave for a 45° incident polarization with potential applications in polarization-division multiplexing and ultrathin tunable waveplates

In chapter 6, a Fano-resonant metasurface is designed to improve both the absorption and collection efficiency of graphene photo-detectors. The metasurface has a drain and source electrode on each unit cell which facilitates the immediate collection of the photogenerated electron-hole pairs. Numerical simulation can estimate the the dark current flowing on graphene and the absorption enhancement. A circuit analysis can provide an analytic expression for responsivity. A comparison between a graphene photodetector with and without metasurface can calculate the responsivity improvement by the metasurface.

In chapter 7, I will study the substrate effect on the quality factor of the fano resonances and I will demonstrate the possibility of all optical measurement of carrier scattering rate.

In Chapter 8, I go over the simulation process used in this dissertation, show the simulation domain and provide details about data analysis used for calculation of spectral response of metasurfaces.

In chapter 9 I conclude the dissertation by summarizing the findings and discuss the prospect for future works.

Chapter 2: Graphene properties

Since being introduced in 2004[81], graphene has been an important frontier in science due to interesting electronics, optical and mechanical properties which makes them relevant to these fields. These properties has been studied in the literature in depth. Here I focus on the electronic and optical properties that are relevant to my research.

2.1 ELECTRONIC PROPERTIES

2.1.1 Electronic dispersion

Graphene has a hexagonal lattice of sp^2 hybridized carbon atoms with two atomic basis A and B in a unit cell as shown in Fig 2.1. The size of C-C atomic bound a_0 and the lattice constant a are $a_0 = 1.42\ \dot{A}$ and $a = 2.46\ \dot{A}$ respectively and the primitive lattice vectors are $a_1 = a\left(\frac{\sqrt{3}}{2}, \frac{1}{2}\right), a_2 = a\left(\frac{\sqrt{3}}{2}, -\frac{1}{2}\right)$.

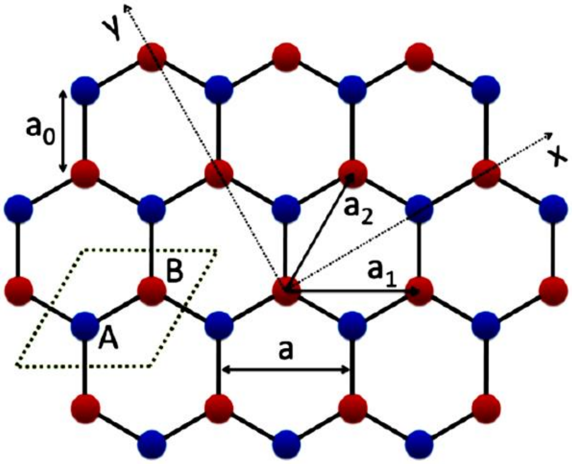

Figure 2.1: Graphene lattice with two atomic basis A and B shown by the blue and red. The closest atomic distance $a_0 = 1.42\ \dot{A}$ and the lattice constant is $a = 2.46\ \dot{A}$. Picture taken from Ref[82]

Starting from these lattice vectors and using tight binding approximation, the band structure can be derived as[83]:

$$E = \pm\gamma_0\sqrt{1 + 4\cos\left(\frac{\sqrt{3}}{2}ak_x\right)\cos\left(\frac{a}{2}k_y\right) + 4cos^2(\frac{a}{2}k_y)} \qquad (2.1)$$

Where γ_0 is the hopping energy between nearest carbon atoms and k_x and k_y are the momentom in x and y directions. The energy band diagram is shown in Fig 2.2a which shows a hexagonal Brillouin zone. The conduction and valence band cones meet at 6 points in the reciprocal lattice known as K points as shown in Fig. 2.2a. The energy band is linear close to the K points and can be described by:

$$E(k) = \pm\hbar v_F|k| \qquad (2.2)$$

where $\hbar$ is the Planck constant, $\upsilon_F = \frac{\sqrt{3}}{2}a\gamma_0/\hbar = 1 \times 10^6\ \mathrm{m/s}$ is the Fermi velocity in graphene and k is the momentum reference with respect to K point. This linear dispersion implies that the effective mass of charges are zero in monolayer graphene which is the reason behind the novel electronic and optical properties of graphene i.e. the large mobility and wideband interband absorption of graphene. Fermi energy which is the energy of the highest level of occupied quantum state at the absolute zero temperature can be described by $E_F = \hbar v_F\sqrt{\pi n_g}$ where n_g is charge carrier concentration on graphene. Graphene is electron-doped if electrons are occupying the conduction band and is hole-doped otherwise as shown in Fig. 2.2b.

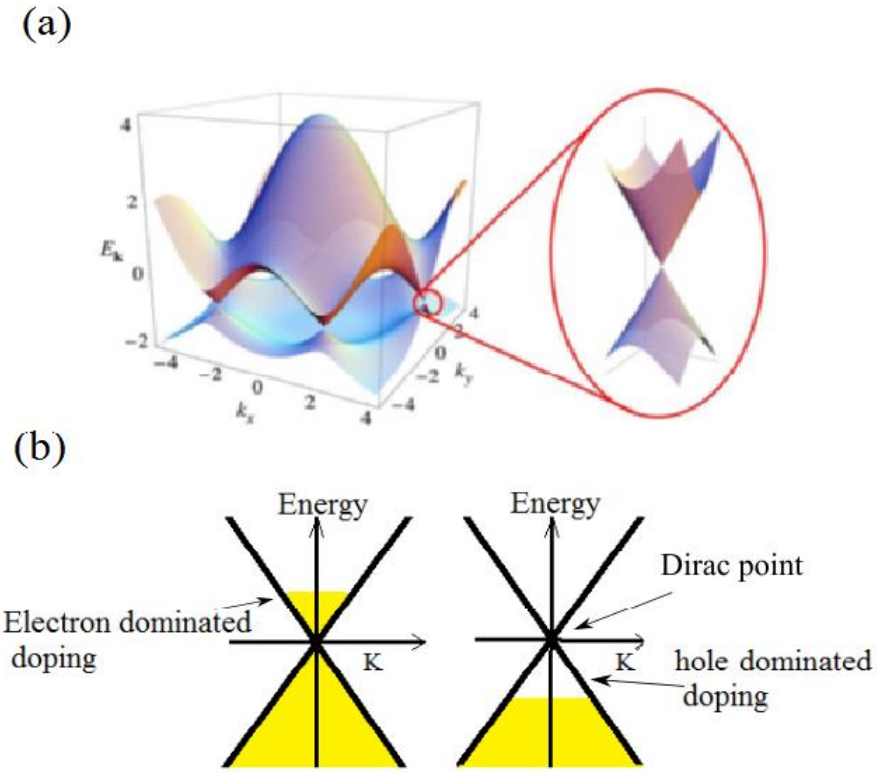

Figure 2.2: (a) Energy-momentum dispersion of monolayer graphene (in units of $\boldsymbol{\gamma_0}$) calculated using tight binding method with γ_0=2.7 eV. The magnified view of the energy bands shows the energy-momentum dispersion is linear close to the Dirac point (Figure and caption adapted from Ref [84]) (b) Energy band for electron-doped graphene (left) and hole-doped graphene (right)

2.1.2. Electrical transport

Graphene exhibits excellent transport properties. The ballistic transport occurs when the charges are not impeded by substrate impurities and phonons and experience no backscattering. The charges move at a velocity of $\upsilon_F = 1 \times 10^6$ m/s with elastic mean free path of few hundreds of nanometers in clean samples. For graphene, the electron scattering from acoustic phonons is weak and the scattering from optical phonon is only important for energies higher than $E_F > 0.2\ eV$. In long graphene channels however, the transport becomes diffusive[85] due to elastic and inelastic scatterings. The elastic scattering are due to coulomb scattering from charged impurities (mainly the trapped charges in the insulating substrate[86]), defects and adsorbates, surface roughness and ripples of graphene[84]. Graphene phonons result in inelastic scattering[87]. In addition the insulating substrate`s surface phonons which are thermally excited can generate electric field that extends away from the surface and can couple to graphene carriers which leads to scattering[88]. The semi-classical diffusive conductivity of graphene can be described by[86]:

$$\sigma = \frac{g_s g_v e^2}{\hbar}\frac{E_F \tau}{2\hbar} \qquad (2.3)$$

In eq. 2.3, $g_s = g_v = 2$ are the spin and valley degeneracy factors and τ is the scattering time. By measuring the conductivity of graphene as a function of the Fermi-energy (I-V measurement) the scattering time can be estimated.

2.2 OPTICAL PROPERTIES

The electrical and optical properties of materials are closely related. The optical absorption in graphene depends on the Fermi energy of electrons as detailed in this section. The absorption of un-doped graphene at zero kelvin temperature is frequency independent and can be described by $A = \pi\alpha \approx 2.3\%$ where $\alpha = e^2/\hbar = 1/137$ is the fine structure constant[89] (see Fig. 2.3a).

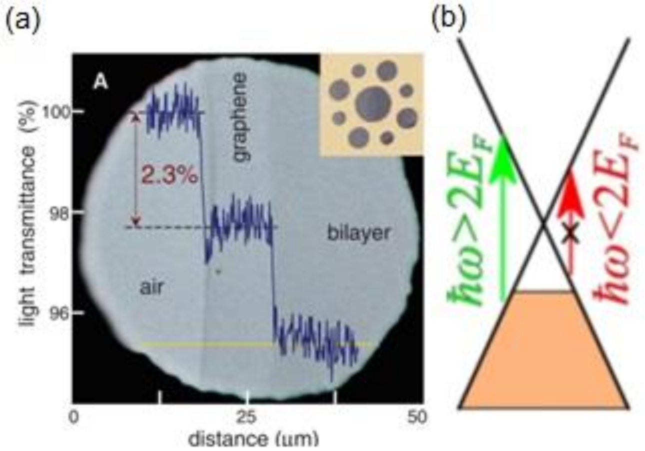

Figure 2.3: (a) Transmission through a monolayer and bilayer of graphene along the yellow line. The picture is taken from Ref [89] (b) interband transition for photon energies higher than $2E_F$ (green arrow). Pauli blocking for energies smaller than $2E_F$.

The light-graphene interaction is strong, for comparison 20 nm of InGaAs would be required to absorb the same amount of telecommunication wavelength, $\lambda = 1.55\mu m$. Optical losses of graphene strongly depend on the carrier concentration (Fermi energy) and mainly originate from two distinct mechanisms:

1) **Interband losses:** If the energy of the photon is larger than $2E_F$ ($\hbar\omega > 2E_F$), the photon can excite an electron from the valence band to the conduction band which is called interband transition as shown in Fig 2.3b.
2) **Intraband losses:** Graphene plasmons lose energy to electrons scattering from charged impurities, defects and phonons as detailed in 2.1.2. This transition will keep the electron in the conduction band and is called intraband transition. The random phase approximation[90] provides an analytical expression for these two transitions:

$$\sigma_{inter}(\omega) = \frac{e^2}{4\hbar}\left[\frac{1}{2} + \frac{1}{\pi}\tan^{-1}\left(\frac{\hbar\omega - 2E_F}{2k_BT}\right) - \frac{i}{2\pi}\ln\frac{(\hbar\omega+2E_F)^2}{(\hbar\omega-2E_F)^2+(2k_BT)^2}\right],$$

$$\sigma_{intra}(\omega) = \frac{e^2}{4\hbar}\frac{8ik_BT}{\pi\hbar(\omega+i\tau^{-1})}\ln\left[2\cosh\left(\frac{E_F}{2k_BT}\right)\right] \tag{2.4}$$

In eq. 2.4, k_B is the Boltzmann constant, T is the temperature, ω is the frequency of IR light, and τ is the free carrier scattering rate.

The real (lossy) part of graphene conductivity for the interband and intraband transitions have been demonstrated in units of universal optical conductivity $\sigma_0 = e^2/4\hbar$ in Fig. 2.4a,b respectively as functions of the wavelength $\lambda = 2\pi c/\omega$. The temperature has been assumed to be room temperature ($300^{\circ}k$). The scattering time of $\tau = 18fs$ (corresponding to the carrier scattering rate $\tau^{-1} = 293cm^{-1}$) was chosen.

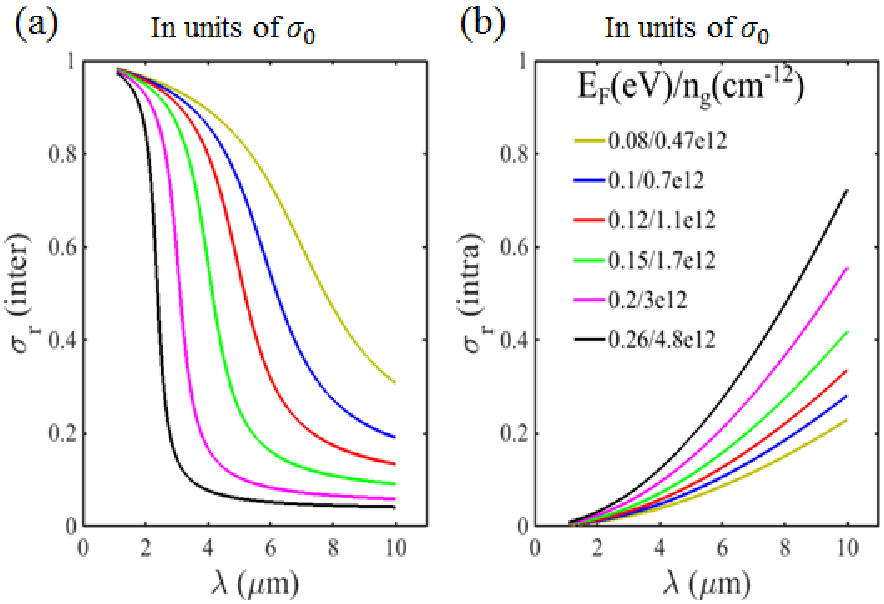

Figure 2.4: The real part of optical conductivity as a function of wavelength for different Fermi energies. (a) the interband (b) The intraband components of loss in units of $\sigma_0 = e^2/4\hbar$. The legend in (b) lists the values of Fermi energy/carrier concentration for each color.

From Fig 2.4 it is apparent that the optical loss strongly depends on the carrier concentration of graphene and wavelength. In the mid-IR range which is the wavelength range of our interest, as the Fermi energy increases the interband loss decreases due to transition to the Pauli blocking regime where $\hbar\omega < 2E_F$ and the optical excitation is avoided (the red arrow in Fig 2.3b). For example at $\lambda = 6\mu m$, the interband loss drops significantly for Fermi energies higher than $E_F = 0.1\ e$V. However the intraband losses increase for higher dopings which is due to higher rate of scattering occasions at larger carrier concentrations.

2.2.1 Graphene plasmonic properties

Graphene is a semi-metal and can be assumed as a conductor. Therefore it has both resistive and reactive properties which is reflected in the real and imaginary part of the conductivity in the random phase approximation formalism. In Fig. 2.5 the ratio between imaginary and real part (σ_i/σ_r) is shown as a function of wavelength and for different Fermi energies at zero temperature. This ratio is less than one for the visible range and far infared as shown by the striped regions, which implies that graphene is mainly lossy (resistive) in these regimes. The dominant loss in the visible and far-infared regions are the interband and intraband transitions respectively. However in the mid-IR regime, this ratio can be large which means graphene is primarily inductive and due to small losses can behave like a plasmonic material. Graphene becomes increasingly metallic as the Fermi energy acquiring qualities of metals such as inductive and plasmonic properties. Therefore, graphene has unique properties in mid-IR and the interaction of graphene with the electromagnetic field of a resonant element at frequency $\omega = 1/\sqrt{LC}$ will induce a frequency shift due to the graphene perturbation in the inductance. By tuning the graphene inductance it`s possible to manipulate the resonance frequency of the resonant element which is the strategy used in dissertation to manipulate the amplitude and phase of the mid-IR light.

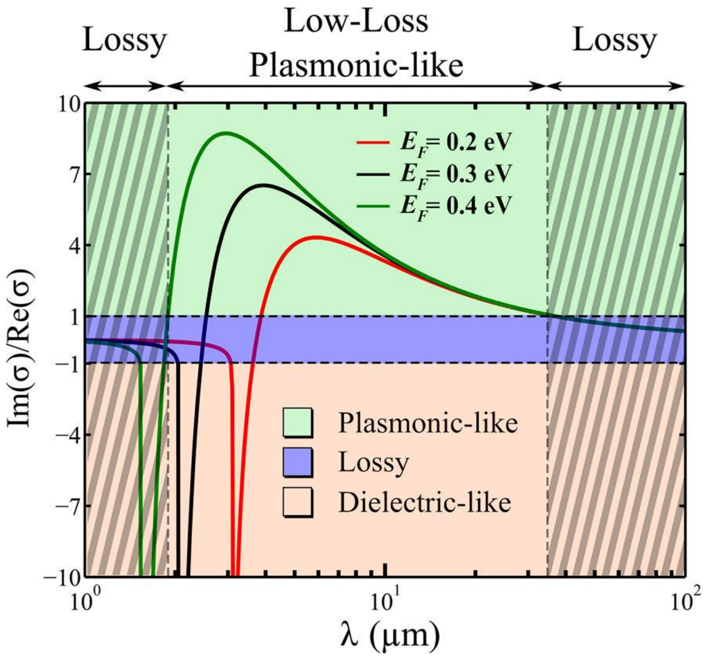

Figure. 2.5: Optical response of moderately doped graphene in different spectral ranges: A mid-IR window, with dominantly plasmonic response, inside the entire optical spectrum with dominantly lossy behavior. Plasmonic and lossy regimes are shown by arrows on the top for a graphene with EF = 0.4 eV. A narrow spectral range at which graphene behaves as a dielectric occurs at $\omega = 2E_F/\hbar$ inside the low wavelength lossy regime. The graphene intraband scattering rate was assumed to be γ = 269 cm−1. (The figure and caption take from Ref [91].

2.3 TUNING CARRIER CONCENTRATION

Being a conductor, graphene can screen the electrostatic fields. The two prominent scheme for gating graphene are back-gating and top-gating as depicted in Fig 2.6. The common approach is to transfer graphene onto a highly doped silicon substrate with an insulator between Si and graphene. Applying a gate voltage V_{BG} between silicon graphene will vary the electrostatic fields $E = V_{BG}/d$ in the insulator and the graphene electron (hole) concentration per area: $n_{e(h)} = CV_{BG}/e$ that screens the fields. Here C and d are the capacitance per area and the thickness of the insulator layer respectively. Similarly, a voltage between graphene and a top-gate V_{TG} can induce carrier concentration of $n_{e(h)} = CV_{TG}/e$ on the graphene below the top-gate. Using these two approaches, one can tune the carrier concentration of graphene at a speed limited by the time constant of the circuit. Here for simplicity, we assumed that the insulator does not have any impurity. For practical substrates, the impurity sites trap charge carriers which will induce a residual charge on graphene. This effect will be elaborated in section 4.8.

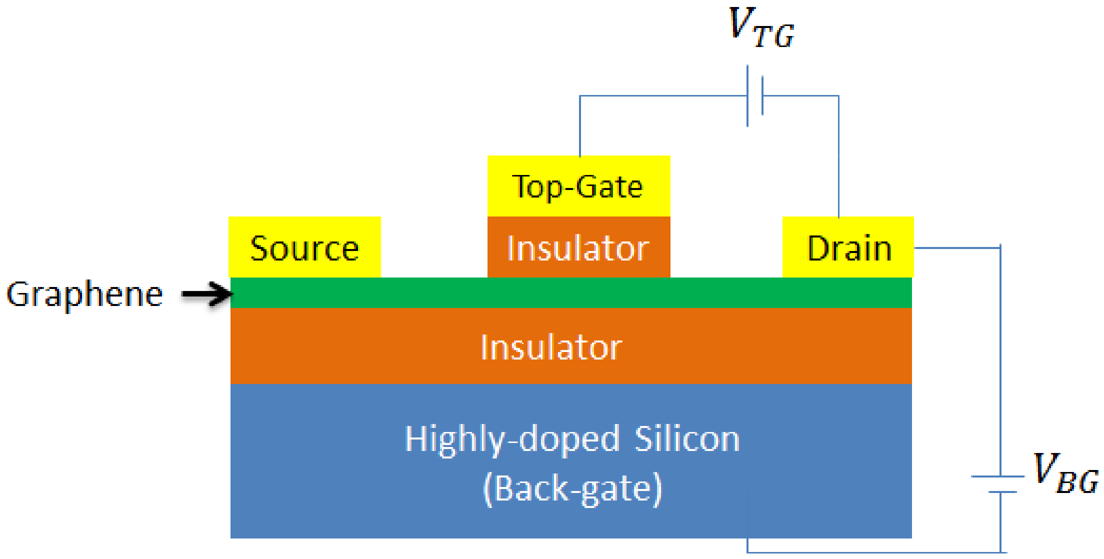

Figure 2.6: Schematic for back-gating and top-gating. A back-gate voltage between highly doped silicon and graphene induces electrostatic fields in the insulator that are screened by a carrier concentration that is proportional to the back-gate voltage V_{BG}. Similarly a voltage V_{TG} can induce charges on graphene below the top-gate.

2.4 GRAPHENE FABRICATION TECHNIQUES

Several methods have been proposed for graphene fabrication. Some of the more established methods include micromechanical exfoliation of graphite, graphite oxidation, synthesis of graphene by chemical vapor deposition (CVD) method, electric arc graphene production, thermal decomposition of silicon carbide and epitaxial growth of graphene on metal surface[92]. In this dissertation, we used CVD graphene which is widely used for the synthesis of carbon nanostructures. In particular, the method is employed to fabricate large-area graphene which is important in our research since the bi-periodic metasurfaces are tens of microns in each dimension. The technique is based on the possibility of thermal catalytic decomposition of gaseous hydrocarbons on the surface of some metals with the formation of various nanocarbon structures[93]. The detail of fabrication stages and transfer technique used in this dissertation is available in appendix B.

2.5 CONCLUSIONS

Graphene exhibits outstanding electronic properties such as large mobility which stems from its unique linear dispersion. In large graphene channels, the electrical transport is diffusive and limited by the elastic and inelastic scattering of the charge carriers. The electrical properties can be described by a semi-classical diffusive conductivity as a function of Fermi energy and scattering time. The later can be derived from electrical transport (I-V) measurements. The optical properties of graphene strongly depends on the Fermi energy of the carrier and can be described by interband and intraband transitions in a random phase approximation. In the mid-IR regime, graphene experiences small optical loss compared to the visible and far-IR/terahertz region and behaves primarily as an inductor. By varying the Fermi level, graphene can be treated as a tunable inductive perturbation to an optical cavity and facilitate the design and fabrication of ultrathin tunable optical devices.

Chapter 3: Fano resonance

3.1 INTRODUCTION:

One of the interesting concepts in study of light-matter interaction is the Fano interference. This phenomena was originally discovered by Fano in quantum physics to describe the asymmetrical shape of ionization spectral lines of atoms and molecules[94]. A higher energy photon ionizes an atom by two different mechanisms. i) Direct optical excitation of an electron from its bound state to the unbound state and ii) Indirect excitation of two electrons into an intermediate bound state, followed by an Auger-like electron ejection. The first process is non-resonant and exists as long as the photon energy exceeds the excitation threshold. However the second process requires the electrons to be excited into a well-defined auto-ionizing state and therefore is resonant. The ionization cross section exhibits an asymmetrical dependence on the photon energy due to quantum mechanical interference between these two processes. In analogy, wave interference can give rise to Fano resonance in photonic systems. In principle the interference between a bright mode with a short lifetime with a dark mode with a long lifetime leads to a Fano resonance. The bright (dark) mode has a strong (weak) radiative coupling to the incident light, however the dark mode is only allowed to couple to the bright mode via near-field. As a consequence, the incident photons can get trapped in the dark mode for a long time before they couple back to the bright mode and radiate to the continuum or decay into the non-radiative (ohmic) channels. This will enhance the light-matter interaction in the spectral vicinity of the dark mode. This concept is illustrated in Fig. 3.1 for two adjacent dipole antennas which supports two eigenmodes. A dipole (bright) mode that can couple to the far field and a quadrupole (dark) mode which cannot couple to the far-field and the dipole mode due to anti-symmetric change distribution. However, by adding an asymmetry to the structure as shown on the right, the dipole and the quadrupole mode start interacting in the near-field as their overlap integral is now non-zero. This energy transfer between the dipole and quadrupole mode enhanced the light-matter interaction as detailed in the proceeding sections.

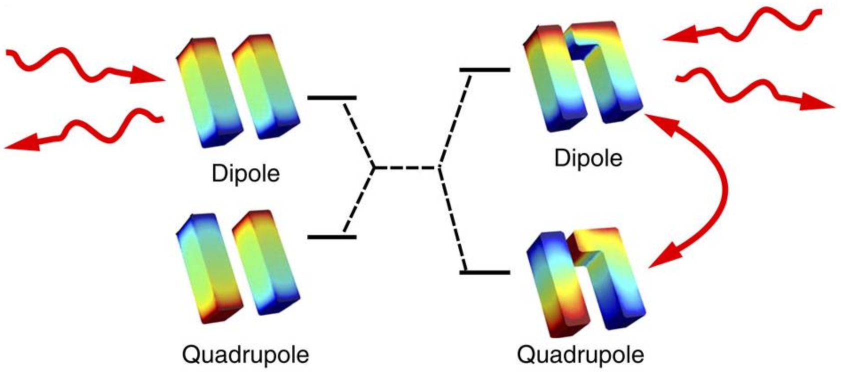

Figure 3.1: The eigenmodes of a double antenna structure (left). The coupling of the quadrupole mode to the far-field is forbidden due to anti-symmetric charge distribution. Adding an asymmetry to the structure (right) will allow near-field interaction between the dipole and the quadrupole mode. Figure taken from Ref [95].

3.2 ANALYTICAL MODELING

The interference of two coupled photonic resonators can be best modeled in the framework of temporal coupled mode theory[96]. It is assumed that the bright mode with the natural frequency of ω_b and the lifetime of τ_b can directly couple to the incident light while the dark mode with natural frequency of ω_d the lifetime of $\tau_d \gg \tau_b$ can only be excited though coupling to the bright mode. The equation of temporal coupled mode theory can describe the dynamics of such two-mode interaction[97]:

$$\dot{a_b} - j(\omega_b + j\tau_b^{-1})a_b + j\kappa a_d = \beta_b S^{in} e^{j\omega t}$$

$$\dot{a_d} - j(\omega_d + j\tau_d^{-1})a_d + j\kappa a_b = 0 \tag{3.1}$$

In eq. 3.1, a_b and a_d are the field amplitude for the bright and dark modes. S^{in} and ω are the amplitude and frequency of the incident field, β_b is the coupling strength of the bright mode to the incident wave, κ is the coupling strength between the two resonators. Eq. 3.1 is normalized in such a way that the incident power is $\left|S^{in}\right|^2$energy stored in the bright and dark modes are $|a_b|^2$and $|a_d|^2$ respectively. It is assumed that the bright mode can radiate into reflection and transmission in a symmetric way, therefore the scattered waves can be expressed as: $S^r = {\beta_b}^* a_b$ and $S^t = S^{in} + {\beta_b}^* a_b$. The reflection and transmission coefficients can be consequently described as[97]:

$$r = \frac{S^r}{S^{in}} = \frac{-j|\beta_b|^2(\omega - \omega_d - j\tau_d^{-1})}{(\omega - \omega_b - j\tau_b^{-1})(\omega - \omega_d - j\tau_d^{-1})}$$

$$t = \frac{S^t}{S^{in}} = 1 + r. \tag{3.2}$$

Also the lifetime of the modes can be derived in terms of radiative τ_R and ohmic lifetimes τ_o:

$$1/\tau = 1/\tau_R + 1/\tau_o \tag{3.3}$$

In Fig. 3.2 the reflectance and transmittance spectra described by eq. (3.2) is shown for different values of spectral detuning $\delta = \omega_b - \omega_d$ between the bright and the dark resonance. The frequency of the bright resonance ω_b is assumed to be fixed while ω_d is changing.

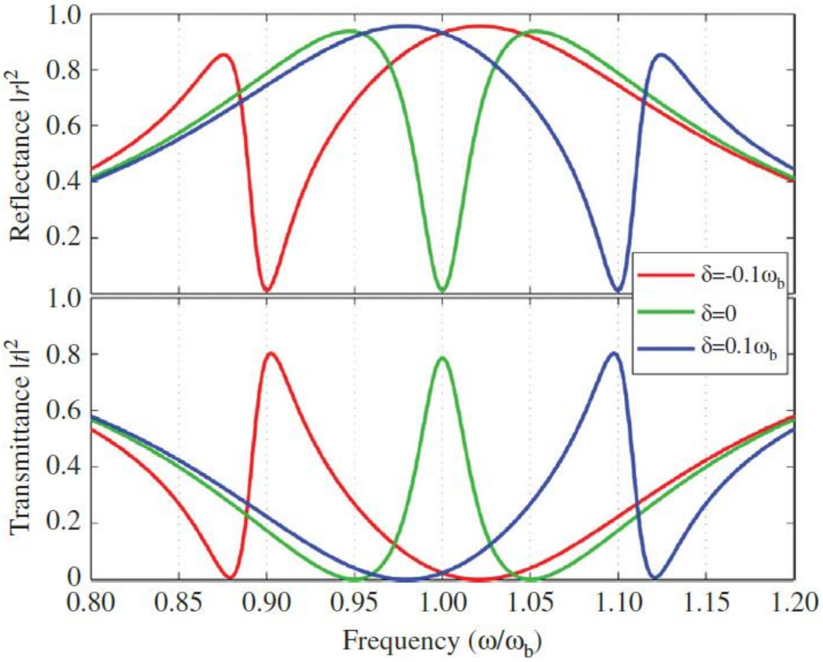

Figure 3.2: Reflectance and transmittance spectra of a Fano-resonant system from eq. 3.1 and 3.2 with finite ohmic losses. The three curves correspond to spectral detuning of $-0.1\omega_b, 0\ , 0.1\omega_b$ as shown by the red,green and blue curves respectively. The parameters used are the following: $\tau_b^R = 10/\omega_b, \tau_b^o = \tau_d^o = 500/\omega_b$ and $\kappa = 0.05\omega_b$. Figure taken from Ref[97].

The strongly asymmetrical scattering spectra for $\omega_b \neq \omega_d$ is the characteristic of the Fano interference between the modes. The particular case that the two resonances have identical spectral position $\omega_b = \omega_d$ is referred to as electromagnetically induced transparrency (EIT) which is distinguished by the symmetrical line-shape (green curve) and maximum transmittance at the resonance. Without the coupling between the resonances ($\kappa = 0$), only a transmission minimum would be observed due to excitation of the bright mode.

3.3 LIGHT-MATTER INTERACTION ENHANCEMENT

As mentioned earlier incident photons that can couple to the dark mode through Fano interference, will be stored in the mode for $\tau_d \gg \tau_b$. Therefore, the energy stored in the dark resonance is much larger than that of the bright mode. In Fig. 3.3, the total stored energy in the system: $|a_b|^2 + |a_d|^2$ is shown as a function of incident frequency normalized to the frequency of the bright mode. The red curve shows the total stored energy which has very high value at $\omega = \omega_d$ which results in large enhancement of the optical near field. This field enhancement can be used in sensing protein monolayers[14], gas-sensing[98] and single-layer graphene[57] just to name a few.

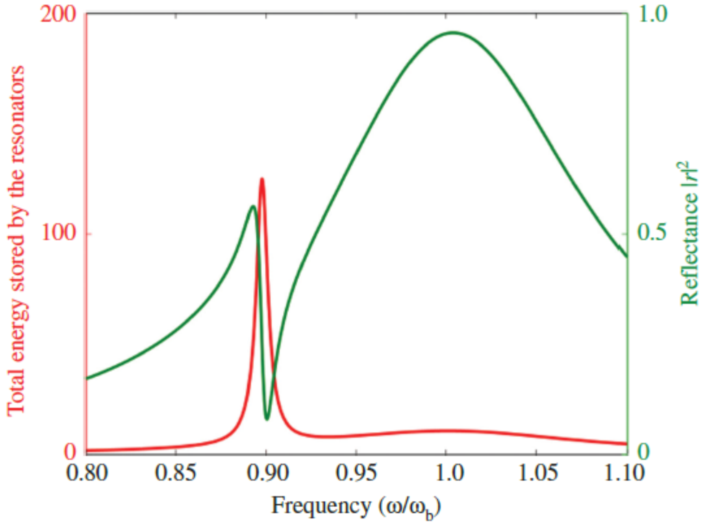

Figure 3.3: The total stored energy in the resonators as a function of normalized frequency ω/ω_b. The reflectance is shown by the free curve. The figure has been taken from Ref [97].

3.4 DOUBLE-LORENZIAN REPRESENTATION:

The Fano expression for the reflection coefficient can be simplified to a double-Lorenzian by assuming that the coupling coefficient κ is frequency-independent and the coupling is weak ($|\kappa| \ll |\delta|/2$), which corresponds to the case that the dark mode has a high quality factor. The double-Lorenzian expression reads[97]:

$$r(\omega) \approx \frac{A_1}{j(\omega-\widehat{\omega}_b)-\hat{\tau}_b^{-1}} + \frac{A_2}{j(\omega-\widehat{\omega}_d)-\hat{\tau}_d^{-1}} \tag{3.4}$$

The new parameters of complex amplitude $A_{1,2}$ and frequency $\widehat{\omega}_{1,2}$ are related to the parameters of the Fano model in the following manner:

$$\begin{aligned} \widehat{\omega}_{b,d} &= \omega_{b,d} + Re\left(\frac{\kappa^2}{\hat{\delta}}\right), \\ \hat{\tau}_{b,d}^{-1} &= \tau_{b,d}^{-1} - Im\left(\frac{\kappa^2}{\hat{\delta}}\right), \end{aligned} \tag{3.5}$$

While the effective radiative coupling parameters are:

$$\begin{aligned} A_1 &= |\beta_b|^2 \left(\frac{\hat{\delta}^2+\kappa^2}{\hat{\delta}^2+2\kappa^2}\right), \\ A_2 &= |\beta_b|^2 \left(\frac{\kappa^2}{\hat{\delta}^2+2\kappa^2}\right) \end{aligned} \tag{3.6}$$

In eq. 3.5 and 3.6, $\hat{\delta} = (\omega_b - \omega_d) + j(\tau_b^{-1} - \tau_d^{-1})$ is the complex spectral detuning. Also $A_{1,2}$ are complex values where $|A_1|$ and $|A_2|$ is the radiative coupling amplitude of the bright and the dark mode.

The bi-resonant expression of eq. 3.4 can fit to the experimentally measured scattering spectrum and derive the frequency and the lifetime of the resonances. This provides a platform for spectroscopic characterization of e.g. an analyte added to a plasmonic metasurface which exhibits Fano resonance. As an example, the complex conductivity of a single layer graphene was characterized by estimating the spectral shift and lifetime modification of a Fano resonance[57]. It must be noted that double-Lorenzian eq. 3.4 can be extended to the case of triple-Lorenzian to model a double-Fano resonance system.

3.5 CONCLUSION

We provided a general picture of Fano interference and used a couple mode theory to analytically model this important phenomena highly used in light-matter interaction. The coupled mode theory can be a useful tool in study of plasmonic metasurfaces with Fano-resonance or metasurfaces that are interacting with a material resonance. In the next chapter, we use a triple-Lorenzian to fit to the experimentally measured reflectivity spectra of a metasurface which supports two Fano resonances. The metasurface is functionalized by graphene which tunes the resonance frequency, lifetime and coupling amplitude, upon applying a gate voltage to the graphene. The coupled-mode model enables tracing these resonance parameters as a function of the gate voltage. By using a perturbation method, we are able to calculate an important property of graphene: the scattering (collisional) time of the carriers.

Chapter 4: Electrical Switching of In[1]frared Light Using Graphene Integration with Plasmonic Fano Resonant Metasurfaces

4.1 INTRODUCTION

As mentioned in chapter 1 and 2, graphene has been recently center of attention as a promising optoelectronic material because its optical properties can be rapidly and dramatically changed using electric gating. Graphene's weak optical response, especially in the infrared part of the spectrum, remains the key challenge to developing practical graphene-based optical devices such as modulators, infrared detectors, and tunable reflect-arrays. In this chapter, it is experimentally and theoretically demonstrated that a plasmonic metasurface with two Fano resonances can dramatically enhance the interaction of infrared light with single layer graphene. Graphene's plasmonic response in the Pauli blocking regime is shown to cause strong spectral shifts of the Fano resonances without inducing additional non-radiative losses. we experimentally demonstrate that, by integrating an SLG with a high-Q Fano-resonant metasurface, it is possible to modulate mid-IR reflectivity an order of magnitude ($\approx 10dB$), thus achieving the modulation depth as high as 90% using electrostatic gating. This is accomplished by designing a metasurface that exhibits a spectrally narrow reflectivity dip. The strong enhancement of the electric field parallel to the SLG's surface is shown to result in strong graphene/metasurface coupling that inductively (i.e. essentially losslessly) shifts the plasmonic resonances of the metasurface by approximately half of the spectral width. The

---

[1] Dabidian, N.; Kholmanov, I.; Khanikaev, A. B.; Tatar, K.; Trendafilov, S.; Mousavi, S. H.; Magnuson, C.; Ruoff, R. S.; Shvets, G. Electrical Switching of Infrared Light Using Graphene Integration with Plasmonic Fano Resonant Metasurfaces. *ACS Photonics* **2015**, *2* (2), 216–227

The role of co-authors in this works was as follows: Kholmanov and Magnuson fabricated and transferred CVD graphene, Khanikaev and Mousavi designed the C-shaped metasurface, Tatar did all the coupled-mode fittings in this chapter. Trendafilov confirmed the theoretical simulations.

resulting electrically controlled deep modulation of the reflected IR light is caused by the said spectral shift which is determined by graphene's optical conductivity $\sigma_i(n)$ and controlled by varying the charge carriers concentration $n(V_g)$ in the SLG by applying a variable back-gate voltage V_g.

We also use first-principles electromagnetic simulations to demonstrate that the phase and amplitude of the reflected light can be dynamically varied independently of each other. Phase modulation (PM) at the specific wavelength λ_R^{PM}can be accomplished by keeping the amplitude R of the reflected light constant while varying its phase ϕ_R as a function of V_g. Similarly, amplitude modulation (AM) can be accomplished at the specific wavelength λ_R^{AM}. Similar amplitude and phase modulation can be accomplished in transmission, thus paving the way for infrared rapidly tunable reflect- and transmit-arrays. The effects of graphene's strong coupling to the metasurface on the optical response (i.e. the wavelength-dependent reflectivity/phase and the linewidth of the reflectivity peak) are investigated by varying the charged carriers' concentration in the electrically gated SLG.

Finally, we experimentally demonstrate the possibility of all-optical measurement of the free carrier collisional time τ[86] which appears in the Drude expression of intraband conductivity of graphene. A simple procedure for extracting τ from the reflectivity spectra of the integrated graphene/plasmonic metasurface is described. This procedure is valid in the low optical frequency regime, where graphene's optical conductivity is dominated by graphene's Drude response. It is demonstrated that this extracted carrier scattering time is consistent with that obtained using dc conductivity measurements.

4.2 SWITCHING STRATEGY

Because the main motivation of this work is the development of an efficient electrically controlled IR modulator, we start be reviewing the desired properties of such device. A conceptual example of a reflection modulator is shown in Figure 4.1a, where the wavelength-dependent reflectivity $R(\lambda)$ from a frequency-selective metasurface can be spectrally shifted from the on- to the off-state by some non-optical (e.g., electrical) means. Ideally, at the targeted wavelength λ, such modulator would have a relatively high on-reflectivity $R_{on}(\lambda)$ and very low off-reflectivity $R_{off}(\lambda)$ in its off-state. The spectral shift could be caused, for example, by applying back-gate voltage V_g to the layer of graphene as shown in Figure 4.1b. The performance of such modulator would be characterized by the modulation depth (MD) defined as $MD \equiv \left(1 - R_{off}/R_{on}\right) \times 100\%$. A high-performing modulator must have $MD > 90\%$.

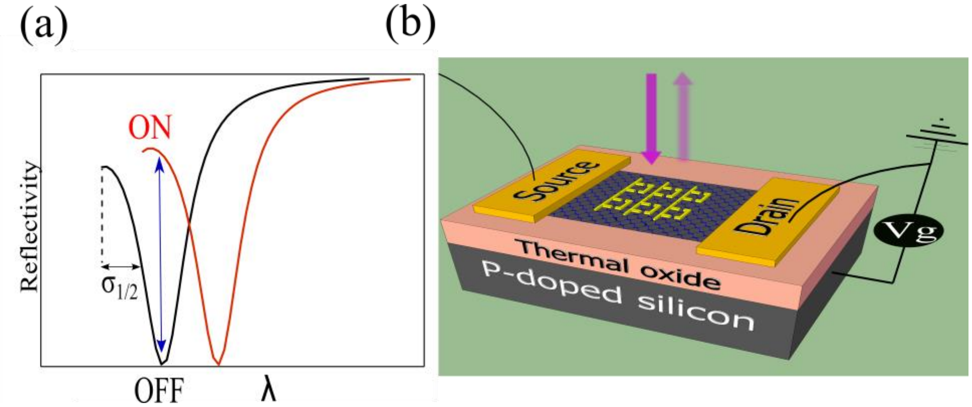

Figure 4.1 **(a)** Conceptual schematic of an efficient light modulator based on a frequency-selective tunable reflector. Key features: narrow linewidth, large spectral shift, and zero reflectivity at the targeted wavelength. The HWHM of the reflectivity peak ($\sigma_{1/2}$) is shown by the black arrow **(b)** The realization based on a Fano-resonant metasurface integrated with graphene. Spectral shifting is achieved by back-gating of the graphene underneath the metasurface.

It follows from Figure 4.1a that the metasurface and its reflectivity $R(\lambda)$ must satisfy the following requirements: (a) narrow linewidth $\sigma_{1/2}$ that can be bridged by graphene-induced spectral shift $\Delta\lambda$; (b) strong concentration of the optical energy by the metasurface capable of producing $\Delta\lambda \sim \sigma_{1/2}$, and (c) near-zero reflectivity in the vicinity of the target wavelength λ. To satisfy these conditions, we have designed a metasurface which exhibits broadband reflectivity that is greatly reduced at the two nearby wavelengths due to the phenomenon of plasmon-induced electromagnetically induced transparency(EIT)[9,100,101] which is directly related to[97] Fano interference.

4.3 METASURFACE DESIGN

The schematic unit cell and the SEM image of the fabricated metasurface are shown in Figures 4.2a,b. The unit cell consists of three key elements: (i) a metallic wire that electrically connects the neighboring cells in y-direction, and whose functionality is to provide broadband reflectivity of the y- polarized light; (ii) a pair of x-oriented monopole antenna pairs [101,102] attached to the wire, and (iii) a C-shaped antenna (CSA) placed in their proximity. The plasmonic metasurface is assumed to be placed on a thick SiO_2 substrate. In practice, the substrate used in the experiments is a finite-thickness ($t = 1\mu m$) SiO_2 grown on a Si wafer, but the oxide layer is thick enough to avoid any effect of the Si wafer on optical properties of the metasurface. This metasurface exhibits an optical response with two maxima in the transmission spectrum (or two deep reflectivity minima) due to Fano resonances, and therefore can be characterized as a plasmonic metasurfaces exhibiting double electromagnetically induced transparency (double-EIT). This effect is illustrated in Figure 4.2c, where we use a bottom-up approach of adding different constitutive parts of the unit cell to illustrate the nature of the two resonances as detailed below.

First, we note that a grid of plasmonic wires behaves as anisotropic "dilute plasma" [103] for the y-polarized incident light. Specifically, the structure strongly reflects the light with the wavelength λ which is longer than the characteristic effective plasmon wavelength $\lambda_{\mathrm{p}}^{\mathrm{eff}}$ which is a function of the inter-wire spacing P_{x}, wire width w, and the frequency-dependent dielectric permittivity $\epsilon_{\mathrm{s}}(\lambda)$ of the underlying substrate. As expected, the reflectivity $\mathrm{R}(\lambda)$ of the wire array shown as the black solid line in Figure 4.2c increases as the function of the wavelength and reaches 60% at $\lambda = 7.5\mu\mathrm{m}$. Next, a CSA supporting a dipolar antenna resonance at $\lambda_{\mathrm{d}}$is added to the metasurface. The destructive interference between anti-parallel currents in the wires and in the CSA for $\lambda > \lambda_{\mathrm{d}}$ produces a pronounced dip in reflectivity at $\lambda_2 \approx 7.2\mu\mathrm{m}$ as shown by the blue line in Figure 4.2c. We refer to this dip as the EIT2. Although the dip at $\lambda = \lambda_2$ is not particularly narrow because of the strong coupling between the dipole-active mode of the CSA and the plasmonic wire, we demonstrate below that the half width at half maximum (hwhm) $\sigma_{1/2}$ of the emerging reflectivity peak can be considerably narrowed by employing a second Fano resonance at the shorter wavelength.

Specifically, by adding the x-directed (horizontal) plasmonic monopole antennas to the wire grid, we introduce a second dark (monopole) mode whose resonant frequency corresponding to $\lambda_m \approx 6.2\mu m$ is primarily determined[101,102] by the monopoles' length l_m according to $\lambda_m \approx 4\sqrt{\epsilon_s}(l_m)$. This emergent mode is referred to as the monopole mode because of the strong current flow between neighboring monopole antennas. Note that if the monopole antennas are equally spaced, that is $P_y = 2\left(L_y + w\right)$, then by symmetry the monopole mode is strictly dark (i.e. completely decoupled from the normally incident light and the concomitant uniform wire current) in the absence of the near-field coupling between the C-shaped and monopole antennas. The symmetry breaking produced by the introduction of the CSA antennas and by the non-equal spacing of the antennas causes the narrow-band monopole mode to couple to the broad-band wire grid currents, thus producing Fano interference. The destructive Fano interference between the wire current and the current flowing between the monopole antennas results in the short-wavelength reflectivity dip at $\lambda_1 \approx 6.2\mu m$ which is referred to as the first EIT (EIT1) in the rest of the paper. The charge distribution and current profile for the EIT1 dip are shown in Figures 4.2e,g respectively.

The addition of the monopole antennas also has an effect on the dipole mode and, by extension, on the EIT2 reflectance dip. By comparing the spectral positions of the EIT2 with (red line) and without (blue line) the monopole antennas, we conclude that the capacitive coupling between the CSAs and monopole antennas causes the spectral position of EIT2 to red-shift. The near-field coupling between C-shaped and monopole antennas produce a characteristic quadrupole-like charge distribution shown in Figure 4.2f which is responsible for electric field enhancement between the antennas. This field enhancement plotted in Figure 4.2d can be exploited in graphene-functionalized metasurfaces as explained below. The near-field coupling between the two discrete (dipolar and monopolar) modes and the broad-band currents flowing in the plasmonic wire grid cause Fano interference. The result of this interference is a double-dip reflectivity spectrum shown in 4.2c (red line). Qualitatively, the EIT2 reflectivity dip at $\lambda_2 \approx 7.6\mu m$ is caused by the counter-flowing currents in the CSA and the wire grid plotted in Figure 4.2h. The resulting narrow reflectivity peak "sandwiched" between the EIT1,2 dips at λ_1 and λ_2 is the main consequence of the double-Fano resonance. It is exploited in this work in order to develop a graphene-based reflection modulator. The modulation is accomplished by electrically controlling the conductivity of graphene, which in turn detunes the reflectivity dips by a considerable fraction of the linewidth $\sigma_{1/2}$ of the reflectivity peak. In order to achieve the largest possible spectral shift of Fano resonances by the addition of an SLG placed underneath the metasurface, it is important that it experiences the largest possible tangential component E_t of the electric field. Therefore, one of the functions of the metasurface is to produce a strong near-field enhancement $\eta = (E_t/E_{inc})^2$ of the incident electric field E_{inc} on the surface of graphene. This tangential field intensity enhancement, which is proportional to the interaction energy between graphene and the metasurface, is plotted in Figure 4.2d as the function of the wavelength of the incident wave. The maxima of η correspond to the spectral positions of the Fano resonances[97]. Note that a much stronger tangential field enhancement is observed at $\lambda = \lambda_2$ compared to $\lambda = \lambda_1$, suggesting that the strongest coupling between the metasurface and SLG should be expected at the long-wavelength (second) Fano resonance. We also note that the possibility of employing two discrete states strongly interfering with a continuum state has been discussed in the original paper by U. Fano[94], and its application to multi-band sensing applications was later suggested[104]. Here, we employ the double-Fano resonance for several purposes. *First,* we use the two Fano resonances in order to produce a narrow-band reflectivity maximum that can be utilized for dynamic modulation of reflectivity using SLG. *Second,* we experimentally demonstrate a dual-band SLG modulator that produces the highest degree of optical modulation at the frequencies corresponding to the two EIT resonances, $\lambda_1$and λ_2. *Third,* we demonstrate that the degree of optical modulation (both in amplitude and phase), which is proportional to the frequency shifts $\Delta\omega_{1,2}$ due to the SLG's hybridization with the metasurface, depends on the tangential field distribution in graphene. For example, the charge distribution on the metasurface corresponding to the second (long-wavelength) Fano resonance supports a much higher tangential field, resulting in $\Delta\omega_2 > \Delta\omega_1$. The consequence of this hierarchy of Fano resonances is that the modulation depth around $\lambda = \lambda_2$ is larger than that around $\lambda = \lambda_1$.

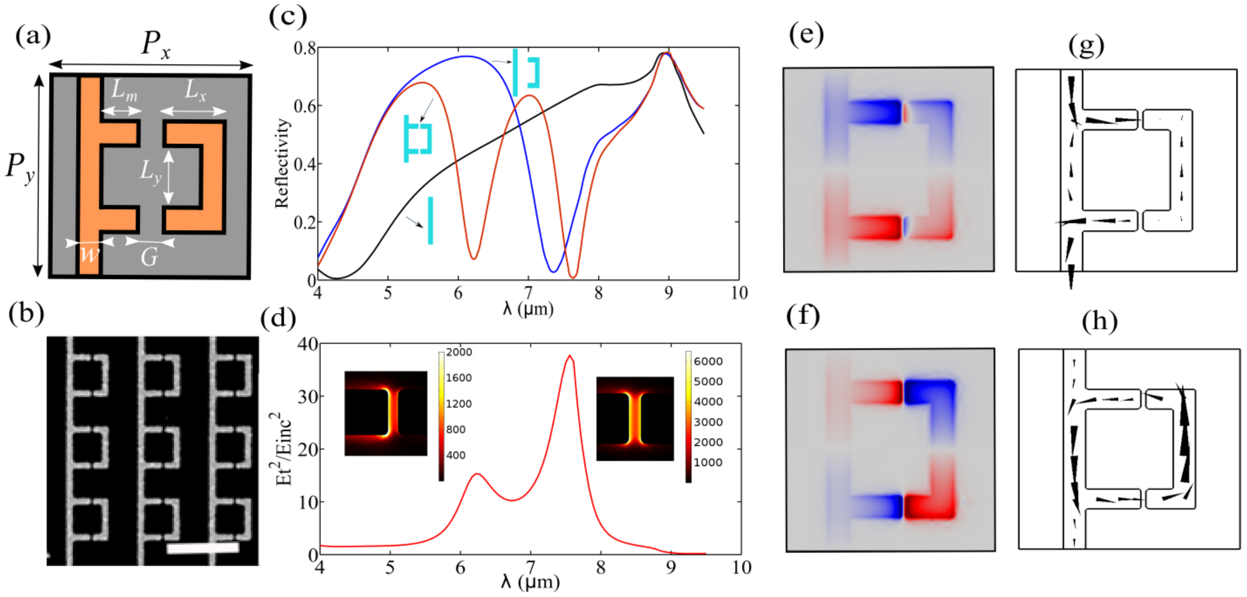

Figure 4.2: **Design of a metasurface exhibiting double-Fano resonance. (a)** Geometry of the unit-cell of the metasurface with parameters: $P_x = P_y = 3\mu m, L_x = .675\mu m, L_m = .75\mu m, L_y = 1.2\mu m$, and $w = .3\mu m$. For the two fabricated metasurfaces $G = 70nm$ and $100nm$. The thickness of metal is $t_m = 30nm$ (5nm Cr+25nm gold) **(b)** SEM image of the metasurface fabricated on top of graphene. Bar: 3μm. **(c)** Simulated Reflectivity at normal incidence for wire grid (black), wire and CSA (blue) and the full structure all on the Si/SiO$_2$ substrate. **(d)** Value of $(E_t/E_{inc})^2$ integrated over graphene surface where E_t is the tangential electric field. The insets show the value of $(E_t/E_{inc})^2$ for the two modes with the colorbar indicating the local values in the gap. In **(e)** and **(f)** colors represent E_z calculated 5 nm below the metasurfaces/SiO$_2$ interface for EIT1 (e) and EIT2 (f) excited by a y-polarized incident field. The electric current density for EIT1 **(g)** and EIT2 **(h)** is plotted inside the metal 5nm above the substrate's surface.

We also note that the possibility of employing two discrete states strongly interfering with a continuum state has been discussed in the original paper by U. Fano[94], and its application to multi-band sensing applications was later suggested[104]. Here, we employ the double-Fano resonance for several purposes. *First,* we use the two Fano resonances in order to produce a narrow-band reflectivity maximum that can be utilized for dynamic modulation of reflectivity using SLG. *Second,* we experimentally demonstrate a dual-band SLG modulator that produces the highest degree of optical modulation at the frequencies corresponding to the two EIT resonances, $\lambda_1$and λ_2. *Third,* we demonstrate that the degree of optical modulation (both in amplitude and phase), which is proportional to the frequency shifts $\Delta\omega_{1,2}$ due to the SLG's hybridization with the metasurface, depends on the tangential field distribution in graphene. For example, the charge distribution on the metasurface corresponding to the second (long-wavelength) Fano resonance supports a much higher tangential field, resulting in $\Delta\omega_2 > \Delta\omega_1$. The consequence of this hierarchy of Fano resonances is that the modulation depth around $\lambda = \lambda_2$ is larger than that around $\lambda = \lambda_1$.

4.4 COUPLED MODE THEORY DESCRIPTION OF DOUBLE-FANO RESONANCES

Extending the earlier developed theory[57,97] of Fano-resonant metasurfaces which demonstrated that the complex-valued reflectivity coefficient $r(\omega)$ from a metasurface supporting a single Fano resonance can be described by a two-pole (double-Lorentzian) function, we approximate the reflectivity from a double-Fano resonant metasurface using the following triple-Lorentzian function:

$$r(\omega) = \frac{A_0}{i\omega - 1/\tau_0} + \frac{A_m}{i(\omega - \omega_m) - 1/\tau_m} + \frac{A_d}{i(\omega - \omega_d) - 1/\tau_d}, \quad (4.1)$$

where $\omega_{m(d)}$ and $\tau_{m(d)}$ are the spectral positions and the lifetimes of the monopole (dipole) resonances of the "bare" (i.e. without graphene) metasurface. The first term in eq 4.1 describes the broadband reflectivity by the plasmonic wires, the second term describes the resonant reflectivity by the monopole resonance, and the third term describes the resonant reflectivity by the CSA resonance. The complex amplitudes A_0,A_m,A_d (where $A_0 \gg A_m, A_d$, see the details in the chapter 7) of the corresponding modes are proportional to their far-field coupling strength[57,97]. Note that, in general, the resonance frequencies do not coincide with the spectral positions of the reflectivity dips: $\omega_{1(2)} \neq \omega_{m(d)}$.The corresponding quality factors of the two resonances defined as $Q_{m(d)} = \omega_{m(d)}\tau_{m(d)}$ will be computed below from the experimental data by fitting the reflectivity spectrum $R(\lambda \equiv 2\pi c/\omega)$ to the $|r(\omega)|^2$ function given by eq 4.1.

4.5 INTEGRATION OF THE METASURFACE WITH GRAPHENE

The multi-pole expansion of the reflectivity coefficient remains valid after loading the metasurface with SLG. The addition of an SLG perturbs the resonant frequencies of the modes according to $\widetilde{\omega}_{m(d)} = \omega_{m(d)} - i/\tau_{m(d)} + \Delta\widetilde{\omega}_{m(d)}$, where the graphene-induced complex-valued frequency shift $\Delta\widetilde{\omega}_{m(d)}$is calculated [57] according to

$$\Delta\widetilde{\omega}_{m(d)} = -i\sigma_{SLG} \int_S |E_t|^2 dS / W_0^{m(d)} \,, \tag{4.2}$$

where $\sigma_{SLG}(\omega) \equiv \sigma_{re} + i\sigma_{im}$ is the complex-valued surface conductivity of the SLG represented as the sum of it resistive and reactive parts, $W_0^{m(d)}$ is the stored energy of the given (monopole or dipole) mode, and the integration is performed over graphene's surface S.

It follows from eq 4.2 that the addition of graphene has two effects: (a) spectral blue-shift of the resonant frequencies $\omega_{m(d)}$equal to $\Delta\omega_{m(d)} = \Re e\left[\Delta\widetilde{\omega}_{m(d)}\right] \propto \sigma_{im}$, and

(b) additional spectral broadening of the mode, i.e. the increase of the quantity $1/\tau_{m(d)}$, which is equal to $\Delta\left(1/\tau_{m(d)}\right) = -\Im m\left[\Delta\widetilde{\omega}_{m(d)}\right] \propto \sigma_{re}$. According to eq 4.2, these frequency/lifetime changes are proportional to the square of the tangential electric field of each mode on graphene, thus suggesting that the dipole resonance should experience larger perturbation that the monopole resonance according to Fig4.2b. Spectral tuning of the optical response of the graphene-functionalized metasurface is accomplished by injecting free charge carriers into graphene.

4.6 TUNING OPTICAL PROPERTIES OF GRAPHENE

As explained in chapter 2, Graphene's optical conductivity $\sigma_{SLG}(\omega)$ can be described by random phase approximation (eq. 2.3) which provides the frequency-dependent conductivity in terms of Fermi energy, scattering time and temperature. The real and imaginary parts of the graphene conductivity $\sigma_{SLG}(\omega)$, measured in the units of universal optical conductivity $\sigma_0 = e^2/4\hbar$, are plotted in Figures 4.3a,b respectively, as functions of the wavelength $\lambda = 2\pi c/\omega$. The scattering time $\tau = 18fs$ (corresponding to the carrier scattering rate $\tau^{-1} = 293cm^{-1}$) was assumed. A dip of σ_{re} is observed at intermediate wavelengths (e.g., $\lambda > 5\mu m$) due to the Pauli blocking of loss-inducing interband transitions. The plasmonic response of graphene can be quantified by the ratio $(\sigma_{im}/\sigma_{re})$ [57], which was recently measured by launching graphene plasmons using near-field scanning optical microscopy[105]. As Figure 4.3c shows, the higher the charge concentration, the larger this ratio becomes, making graphene increasingly plasmonic.

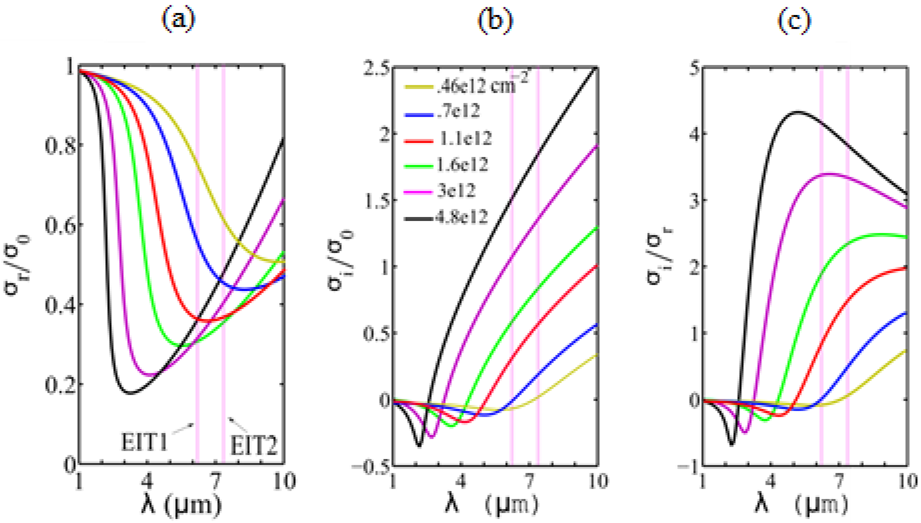

Figure 4.3 Optical properties of graphene. **(a)** Real and **(b)** imaginary parts of graphene's optical sheet conductivity $\sigma_{SLG}(\omega)$ calculated from eq 2.4 for different values of graphene doping. **(c)** Ratio of inductive to resistive conductivities for different free carrier densities in graphene color-coded according to the inset in (b). Carrier scattering time: $\tau = 18\text{fs}$.

4.7 SAMPLE FABRICATION

The process of sample fabrication followed the steps below. First, the SLG was grown on polycrystalline Cu foil using a CVD technique[106] and subsequently transferred from the Cu foil onto $1\mu m$ thick insulating (SiO_2) layer that was grown on a lightly doped silicon substrate[107] using wet thermal oxidation. Second, good quality graphene area were isolated with an oxygen plasma cleaning step. Thirdly, two $100\mu\text{m} \times 100\mu\text{m}$ metasurface samples with unit cell dimensions given in Figure 4.2 and two different gaps ($G = 70nm$ for Sample 1 and $G = 100nm$ for Sample 2) between the CSAs and monopole antennas were fabricated on top of the isolated SLG using electron beam lithography (EBL). The detailed recipe for nanofabrication and graphene synthesis and transfer is available in appendix A and B respectively. The thickness of the metasurface was 30nm (5nm of Cr and 25nm of Au). An SEM image of a segment of the Sample 1 is shown in Figure 4.2b, where the inset zooms in on a single unit cell of the metasurface on SLG. Finally, source and drain contacts (10nm Cr+100nm Au) were deposited on top of graphene on both sides of the metasurface using another EBL step. Back-gating voltage applied across the SiO2 insulating layer between the Si substrate and the drain electrode was used to modulate graphene's carrier density as shown in Figure 4.1b.

4.8 EXPERIMENTAL RESULTS

Two metasurfaces with physical dimensions given in the caption of Figure 4.2 were fabricated on top of an SLG grown using chemical vapor deposition (CVD) and transferred onto an oxidized Si wafer. The carrier density n in graphene was controlled by an applied electrostatic potential difference between the SLG and the Si backgate according to $n \cong \sqrt{{n_0}^2 + (C_g \Delta V/e)^2}$, where n_0 is the residual carrier density at $V = V_{CNP}$ which is the potential at the charge neutrality point (CNP) and $\Delta V = V_g - V_{CNP}$ is the potential deviation from the CNP voltage V_{CNP} that can be experimentally determined from electric measurements[108] as shown below in Figure 4.4a and $C_g = \varepsilon/d$ is the gate capacitance per unit area; d and ε are the thickness and electrostatic permittivity of the SiO_2 spacer. The reason for having residual charges n_0 at the CNP can be explained as follows: The SiO_2 substrate has impurities and defect sites close to the surface. As CVD graphene is transferred onto the oxide substrate, graphene carriers (electrons and holes) will get trapped in the defect sites. The trapped charges will produce electrostatic fields that are screened by graphene. This results in puddles of electrons and holes across graphene with concentrations that depends on the concentration of substrate

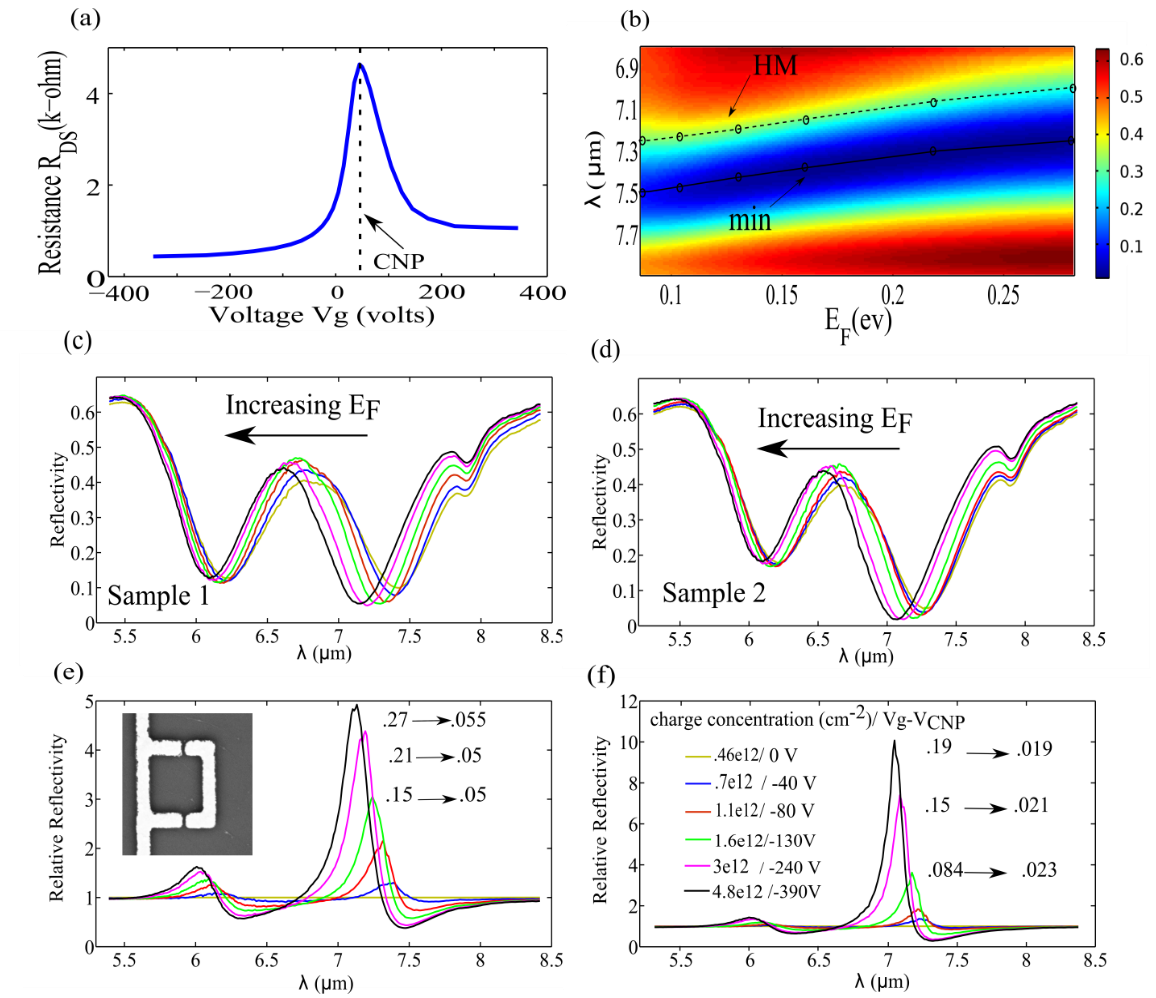

Figure 4.4: Experimentally measured reflectivity modulation from a plasmonic metasurface (see inset) integrated with back-gated graphene. **(a)** Measured drain-source dc electric resistance of the SLG vs gate voltage V_g (see Figure 4.1b). Charge neutrality point: $V_{CNP} \approx +45V$**.** **(b)** Color-coded reflectivity from the Sample 1 in the vicinity of the dipole resonance. The minimum (min) and the half maximum (HM) of the reflectivity spectrum are shown for different Fermi energies E_F. **(c,d)** Reflectivity spectra for the Sample 1 **(c)** and Sample 2 **(d)**. The spectra are color-coded according to the values of $n(\Delta V)$ tabulated in **(f)**. Inset in **(c):** SEM image of the unit cell of the metasurface fabricated on top of the CVD graphene. **(e,f)** Relative reflectivities (extinction ratios) $\mathrm{RR}(n,\lambda)$ corresponding to the spectra in **(c,d)**. Insets: baseline reflectivity $\mathrm{R_{on}}(\lambda)$ at $\Delta\mathrm{V} = 0$ and the extinguished reflectivity $\mathrm{R_{off}}(\mathrm{n_h},\lambda)$ for the 3 highest holes' concentrations n_h corresponding to the maximum of $\mathrm{RR}(n,\lambda)$.

impurities[86,109]. Therefore at the charge neutrality point, the conductivity and the carrier concentration is finite. We estimate that for our sample $C_g \approx 2nF\ cm^{-2}$. The residual charges at the CNP point can be estimated to be around $n_0 = 0.46e12\ cm^{-2}$ using a self-consistent method[86] as detailed in the next section. All experiments were carried out in the hole-injection regime of $\Delta V < 0$.

4.8.1 Electrical transport measurement

SLG's characterization was carried out using current-voltage (I-V) measurements. The charge neutrality point (CNP) $V_g = V_{CNP} = 45V$ is identified by measuring the drain-source electric resistance $R_{DS}(V_g)$ as shown in Figure 4.4a. In the absence of gating ($V_g = 0$), graphene is hole-doped which is due to doping by adsorbates such as resist residue added during fabrication and OH groups that borrow electons from graphene[109]. For voltages smaller than the charge neutrality point $V_g < 45$V, graphene is hole-doped and for $V_g > 45$V, it is electron-doped. We choose to inject hole into graphene, because at $V_g = 0$ graphene is hole-doped. This means for large gate voltages we can achieve higher ΔV and Fermi levels with negative voltages (hole injection) compared to positive voltages (electron injection).

Due to the breakdown voltage of silicon dioxide at 0.5 GV/m, we vary the back gate voltage in the $-345V < V_g < 45V$ range using "Heathkit 500V PS-3" power supply. The holes' areal concentration (given by $n_h = C_g \Delta V / e$) can reach the maximum values of $n_h^{max} \approx 4.8e12\ cm^{-2}$ for the peak gate voltage.

4.8.2 Optical modulation/switching measurement

Optical characterization of back-gated metasurfaces integrated with graphene was performed in the mid-infrared part of the spectrum using a Thermo Scientific Continuum microscope coupled to a Nicolet 6700 FTIR Spectrometer with NA=0.58. The sample spectra averaged over 32 scans were collected with spectral resolution of 4 cm^{-1}.

The reflectivity spectra $R(n, \lambda)$ from graphene-integrated Fano-resonant metasurfaces are plotted in Figures 4.4c and 4.4d for Samples 1 ($G = 70nm$) and 2 ($G = 100nm$), respectively. The spectra are color-coded according to the values of carrier (hole) concentrations $n \equiv n_h$ in the SLG described in the Figure 4.4f inset. The color-coded spectra for the Sample 1 in the vicinity of the dipole resonance (close to the EIT2 reflectivity dip) are re-plotted in Figure 4.4b to illustrate that the spectra are shifted by more than hwhm of the reflectivity peak by changing the free carrier areal density in graphene from $n = n_0$ to $n = 4.8 \times 10^{12} cm^{-2}$. This remarkably strong effect of graphene on the reflectivity is caused by two properties of the graphene-loaded metasurface: (i) narrow spectral width of the reflectivity peak, and (ii) strong concentration of the tangential electric field. While the most dramatic modulation of the reflected intensity is observed near the EIT2 dip (around $\lambda_2^{mod} \approx 7\mu m$), a weaker (but comparable with the present state-of-art results[105]) are also observed near the EIT1 dip (around $\lambda_1^{mod} \approx 6\mu m$).

To quantify the efficacy of the resulting graphene/metasurface modulator, we define the wavelength-dependent modulation depth (MD) as [110–112]

$$MD(n, \lambda) = \left|\frac{R_{on}(\lambda) - R_{off}(n, \lambda)}{R_{on}(\lambda)}\right| \times 100\% = \left|1 - \frac{1}{RR(n, \lambda)}\right| \times 100\%. \qquad (4.3)$$

Here $RR(n, \lambda) = R_{on}(\lambda)/R_{off}(n, \lambda)$ is the extinction efficiency that represents the ratio between the baseline reflectivity $R_{on}(\lambda) \equiv R(n = n_0, \lambda)$ measured in the absence of free carriers in the SLG and the extinguished reflectivity $R_{off}(n, \lambda) \equiv R(n, \lambda)$ measured for the gate voltage corresponding to the finite gate-induced carrier concentration $n = n_h$. Relative reflectivities $RR(n, \lambda)$ for the Samples 1 and 2 are plotted in Figures 4.4e,f, respectively. The higher is the relative reflectivity, the better is the modulator. Ideally, one would prefer that both the baseline reflectivity $R_{on}(\lambda)$ and the relative reflectivity $RR(n_h^{max}, \lambda)$corresponding to the largest applied voltage be large numbers. For example, a modulator with a low value of the baseline reflectivity would be inefficient regardless of its relative reflectivity. As our experimental results presented in Figures 4.4c,d indicate, these two requirements can indeed be satisfied by a Fano-resonant metasurface integrated with back-gated SLG.

Specifically, large values of the peak RR, defined as $RR_{peak} \equiv \max_\lambda RR(n_h^{max}, \lambda)$, are experimentally measured around λ_2^{mod} for both samples. For Sample 1, $RR_{peak}^{(1)} \approx 5$ leading to $MD_{peak}^{(1)} \approx 80\%$ (corresponding to extinguishing the baseline reflectivity from 27% down to 5.5%) is demonstrated, while an even higher $RR_{peak}^{(2)} \approx 10$ leading to $MD_{peak}^{(2)} \approx 90\%$ (corresponding to extinguishing the baseline reflectivity from 19% down to 1.9%) is achieved for Sample 2. We note that these modulators are relatively narrow band because of the resonant nature of the metasurface. For example, the 3dB bandwidth of the modulation depth was measured to be $\Delta\lambda^{(1)} = 245nm$ and $\Delta\lambda^{(2)} = 140nm$ (corresponding to 3.5% and 2% of the resonance wavelength) for Samples 1 and 2, respectively. We also observe that the RR is much smaller for the shorter-wavelength monopole mode at $\lambda_1^{mod} = 6\mu m$. This is a direct consequence of the weaker tangential field enhancement η at the monopole resonance as observed from the theoretical calculation shown in Figure 4.2d.

Note that the small feature at $\lambda \approx 7.9\mu m$ is due to the occurrence of epsilon near zero (ENZ) effect that stems from the longitudinal phonon polariton resonance of SiO_2 where $\varepsilon_r^{SiO_2} = 0$ [113,114]. This resonance is excited by the electric field component of the incident light (E_z) which is normal to the substrate. Therefore it is predicted to appear for finite incidence angle and P-polarized incident field. These are indeed the experimental conditions encountered in our experiment because of the inherent properties of the focusing optics of the infrared microscope. The existence of an optical phonon at $\lambda_{SiO_2} \approx 9\mu m$[115] and the strongly dispersive character of the substrate's dielectric permittivity $\epsilon_{SiO_2}(\omega) \equiv \epsilon_r + i\epsilon_{im}$ affect the quality factor of the dipole resonance. Specifically, the resonant behavior of $\epsilon_r(\omega)$ causes the quality factor and spectral shift of the dipole mode to increase in comparison with the case of an idealized (non-dispersive) substrate that is typical for visible/near-IR frequency range. Additional information about the substrate effect is provided in Chapter 7.

As mentioned earlier, an ideal modulator needs to be both efficient (high baseline reflectivity, i.e. moderate insertion loss) and possess a high modulation depth. Achieving high MD by itself is not particularly challenging: as long as the reflectivity drops to near-zero value (as it is indeed the case according to Figures 4.4c,d of the metasurface under this study), even the slightest spectral detuning of the Fano resonance will result in a high MD. Simultaneously satisfying the efficiency requirement is more challenging because it requires that the spectral detuning $\Delta\lambda_{m(d)}$due to graphene be comparable to $\sigma_{1/2}$.

4.9 DERIVATION OF RESONANCE PARAMETERS USING COUPLE MODE THEORY

In order to understand how the SLG shifts the frequencies and quality factors of the two Fano resonances, we have fitted the experimentally measured reflectivity spectra $|r(\omega)|^2$ for the Sample 1 to the triple Lorentzian formula given by eq 4.1. The fitting parameters are $A_0, A_m, A_d, \omega_m, \omega_d, \tau_0, \tau_m$ and τ_d which represent the complex amplitude of the background, monopole mode and dipole mode, the frequency of the monopole mode and the dipole mode and the lifetime of the background, monopole and the dipole mode respectively. Defining the difference between the two sides of eq 4.1 as:

$$Diff(\omega, A_0, A_m, A_d, \omega_m, \omega_d, \tau_0, \tau_m, \tau_d) = \left[r(\omega) - \frac{A_0}{i\omega - \frac{1}{\tau_0}} - \frac{A_m}{i(\omega - \omega_m) - \frac{1}{\tau_m}} - \frac{A_d}{i(\omega - \omega_d) - 1/\tau_d} \right]^2 \tag{4.4}$$

The fitting becomes possible by minimizing $\sum_\omega Diff$. The least-square method was applied in Matlab where initial values and a range for all fitting parameters were provided as the input. The results of the fitting procedure for the three selected concentrations of charge carriers are shown in Figure 4.5a. The ENZ feature has been excluded from the fitting window.

The resonant wavelengths $\lambda_{m(d)}$ and quality factors $Q_{m(d)}$ for the two resonances are plotted in Figure 4.5 for increasing doping levels n_h. According to Figures 4.5b,d, the resonant wavelengths first slightly increase for small values of n_h because $\sigma_i(\lambda_{m(d)}) < 0$ due to the interband term [41,57] as shown in Figure 4.3c. This spectral detuning is very small for carrier concentrations corresponding to interband transitions-dominated regime which is defined by $2E_F(n) < \hbar\omega_{d(m)}$ and bounded by the vertical dashed lines in Figure 4.5. At the same time, as the Pauli blocking starts taking place for $2E_F(n) > \hbar\omega_{d(m)}$, the quality factor of both resonances experiences a rapid increase shown in Figures 4.5c,e by the red circles. The rise in the Q-factors (QFs) correlates with the decrease of the real (dissipative) part of graphene's surface conductivity σ_r shown by the blue circles in Figures 4.5c,e. Overall, the transition to Pauli blocking regime for high values of carrier density causes considerable change of the QFs for both modes: the $Q's$ of the monopole and dipole mode change in the $14.3 < Q_m < 16.4$ range (15%) and in the $15.0 < Q_d < 18.2$ range (21%), respectively. Note that the maximum of QF approximately coincides with the minimum of σ_r for both modes. Spectral blue-shifting of both resonances can be clearly observed in Figures 4.5b,d as the carrier density increases. This experimentally observed behavior is consistent with eq 4.2. For example, for the dipole mode the spectral shift is $|\Delta\lambda_d| \approx 0.33\mu m$ $(\Delta\omega_d \approx 62\ cm^{-1})$ or about $|\Delta\lambda_d|/\lambda_d \approx 4.6\%$ of the total bandwidth. Assuming that $Q_d \approx 18$, we conclude that the $|\Delta\lambda_d|/\lambda_d > 1/2Q_d$ condition, which is necessary for an efficient and deep modulator, is satisfied for the dipole resonance of the integrated graphene/metasurface structure.On the other hand, the corresponding spectral shift numbers for the monopole resonance (EIT1) are more modest: $|\Delta\lambda_m| \approx 0.09\mu m$ $(\Delta\omega_m \approx 23\ cm^{-1})$, or about $|\Delta\lambda_m|/\lambda_m \approx 1.4\%$. The spectral shift of the monopole mode is considerably smaller than that of the dipole mode, which is mainly due to its weaker interaction with graphene (smaller tangential field enhancement η) as shown in Figure 4.2d.

Eq. 4.1 is the expression of a triple Lorentzian with A, ω and τ, representing the complex amplitude, frequency and the life time of the resonances. As graphene doping changes these values also vary as table 4.1 shows. It would be interesting to compare the amplitude and the life time of the three different Lorentzian. As stated before, the amplitude is proportional to the far field radiation and the life time represents the loss of the modes. This is an interesting example of coupling between the bright background (continuum) mode with dark (discrete) modes. It`s expected for the bright background to have large amplitude and short life time whereas the dark modes is supposed to have

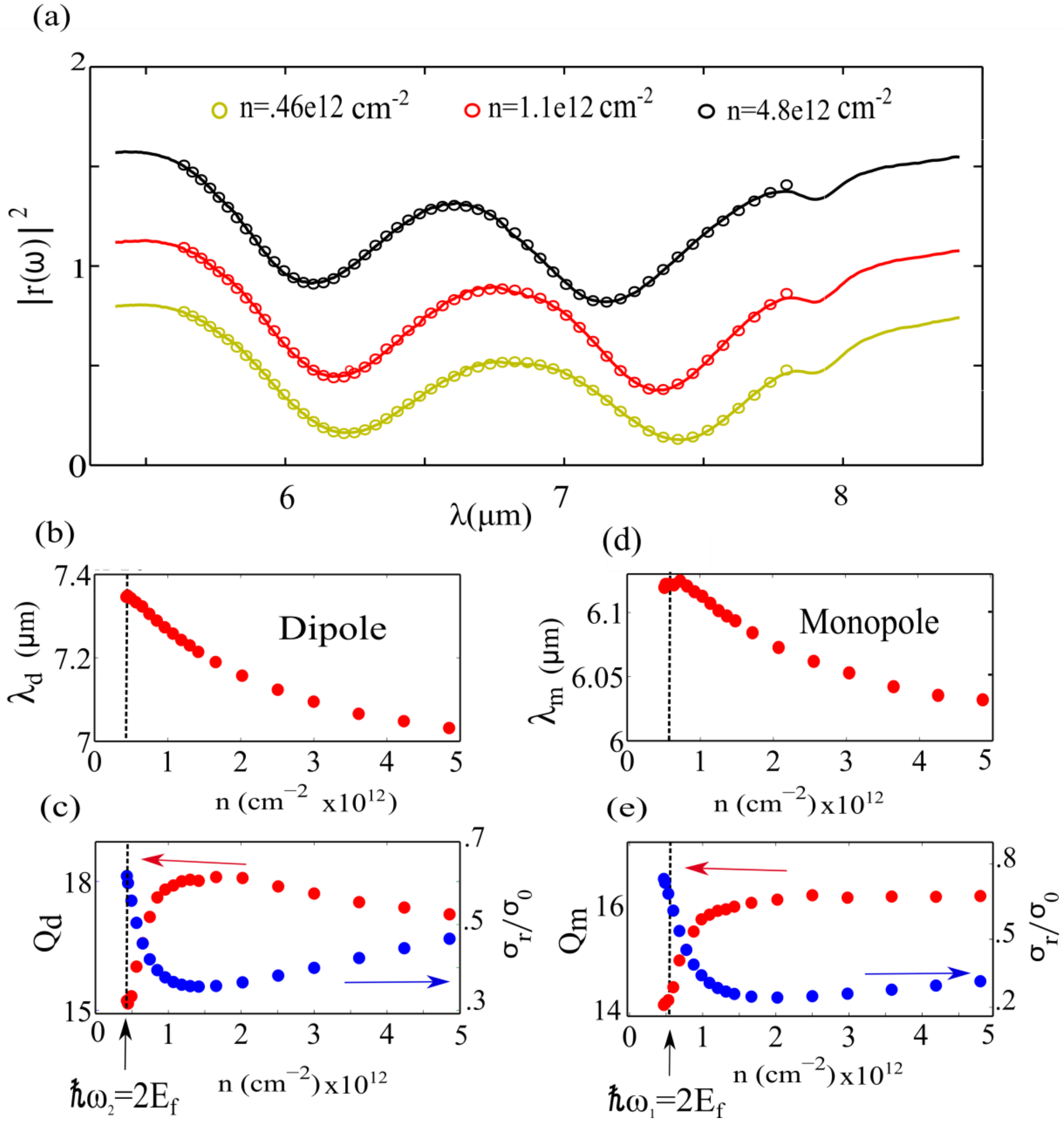

Figure 4.5: **(a)** The measured reflectivity spectrum (solid lines) for Sample 1, fitted to the tri-Lorentzian spectrum given by eq 4.1 (circles) for three selected holes' concentrations. **(b-c)** Extracted resonant wavelengths λ_d and the quality factor $Q_d(n)$ of the dipole mode**. (d,e)**: same as **(b,c)**, but for the monopole mode. Vertical dashed lines: carrier concentration n corresponding to $2E_F(n) = \hbar\omega_{d,m}(n)$. Blue circles in **(c)** and **(e)**: σ_{re} in units of the universal conductance $\sigma_0 = e^2/4\hbar$ calculated at corresponding resonant frequencies $\omega_{d,m}(n_h)$.

smaller amplitude and longer life time. This is obvious from table 4.1 because $|A_0| \gg |A_m|, |A_d|$ and $\tau_0 \ll \tau_m, \tau_d$.

$n(cm^{-2})$	$\lvert A_0\rvert$	$\lvert A_m\rvert$	$\lvert A_d\rvert$	$f_m(1/cm)$	$f_d(1/cm)$	$\tau_0\ (fs)$	$\tau_m(fs)$	$\tau_d(fs)$
$0e12$	3.17	0.31	0.12	1634	1359	7.0	46.6	59.0
.5e12	3.34	0.29	0.12	1632	1363	5.5	49.4	64.4
1e12	3.52	0.27	0.11	1637	1375	4.5	52.2	69.7
1.6e12	3.59	0.27	0.11	1642	1394	4.3	53.0	70.2
3e12	3.59	0.28	0.12	1651	1407	4.2	53.0	67.5
4.8e12	3.49	0.28	0.13	1657	1421	4.5	52.6	64.6

Table 4.1: The doping dependent values for amplitude, frequency and the life time of the triple Lorentzian in eq. 5.1 The frequency values are in (cm^{-1}) and the life times have a femtosecond unit.

All the fittings in this section was performed by Kaya Tatar.

4.10 CONCLUSIONS

We have experimentally demonstrated electrical control of the reflectivity of mid-infrared light using back-gated single layer graphene. An order of magnitude modulation of the reflected light was accomplished by designing a novel type of a metasurface supporting double Fano resonances and integrating it with an under-layer of graphene. The unique aspect of such modulator is its high baseline reflectivity and large reflectivity extinction coefficient (modulation depth). A new metasurface-based approach to extracting the free carrier scattering rate in graphene was also demonstrated. Numerical simulations indicate that independent amplitude and phase modulation are possible in reflection and transmission. This work paves the way to future development of ultrafast opto-electronic devices such as dynamically reconfigurable holograms, single-detector imagers, dynamical beam-steering devices, and reconfigurable biosensors.

Chapter 5: Experimental Demonstration of Phase Modulation and Motion Sensing Using Graphene-Integrated Metasurfaces

5.1 INTRODUCTION

Plasmonic metasurfaces can modify the wavefront of light by altering its intensity, phase and polarization state. Integration of plasmonic metasurfaces with active components, giving rise to active plasmonic metasurfaces, allow dynamic modulation of the wavefront leading to interesting applications such as beam-steering, holograms and tunable waveplates. Fig. 5.1 shows the schematic of a device which can electrically control the wavefront of the incident beam with an antenna array and an active medium. Such device is known as reflect antenna array and requires careful design of antennas and an active mechanism which can control and change the phase by 2π. In particular each of the antennas needs to induce a different phase shift that linearly depends on its position along the array. Using such mechanism, active steering of the beam of light in different directions at high-speeds is a possibility as long as the active material and the electrical circuit operate at high-speed. Graphene is an interesting material whose property can be actively controlled by electrical gating at a Gigahertz rate. In this chapter, we use a graphene-integrated metasurface to induce a tunable phase change to the wavefront of the reflected light. The metasurface supports a high quality Fano resonance around 7.7 micron. The phase change due to electrical gating is measured using a Michelson interferometer. It is shown that the reflection phase can be tuned up to 55° on gating the graphene. In particular the phase can be changed by 28° while keeping the reflected amplitude nearly constant. Using the experimentally measured phase, it is also demonstrated that the polarization state of the reflected light can be modulated via application of a gate voltage. Finally, we show a proof of concept application of our system as a potentially high-speed non-moving laser interferometry system with sub-micron accuracy.

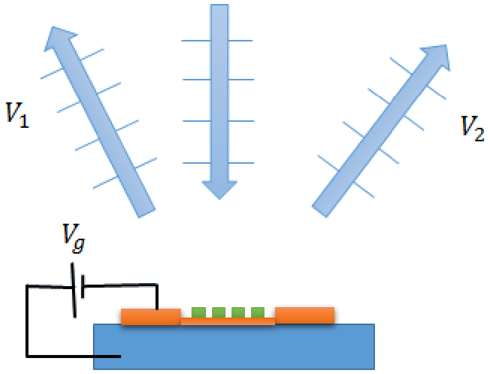

Figure 5.1: Schematic of a device which can actively steer the beam into different direction with an electrical control signal. The blue lines represent the phase front of reflected waves.

5.2 METASURFACE DESIGN/OPTICAL CHARACTERIZATION

In chapter 4, we showed 10 dB amplitude modulation, effectively switching the Mid-IR light by electrically controlling the charge concentration of single layer graphene (SLG) that is integrated to a plasmonic Fano metasurface[99]. In this chapter, we use a similar active metasurface, using SLG as the active electro-optical material, but focus on the phase modulation of the reflected waves as shown in Fig. 5.2a where a backgate scheme is used to change graphene doping by an electrostatic gate voltage V_g. This in turn induces a gate-voltage dependent phase change $\Delta\Phi(V_g)$ to the wavefront of the waves reflected from the plasmonic metasurface. Using a Michelson interferometric setup as depicted in Fig. 5.1b, we measure the voltage dependent modulation of reflection phase. We employ the plasmonic metasurface to enhance the interaction of electromagnetic fields with the single layer graphene (SLG). The unit cell of the metasurface is shown in Fig. 5.3a which consist of a continuous wire and a dipole. The metasurface exhibits electromagnetically induced transparency (EIT). This EIT is directly related to the Fano resonances which is defined by the interaction of a bright mode with broadband response

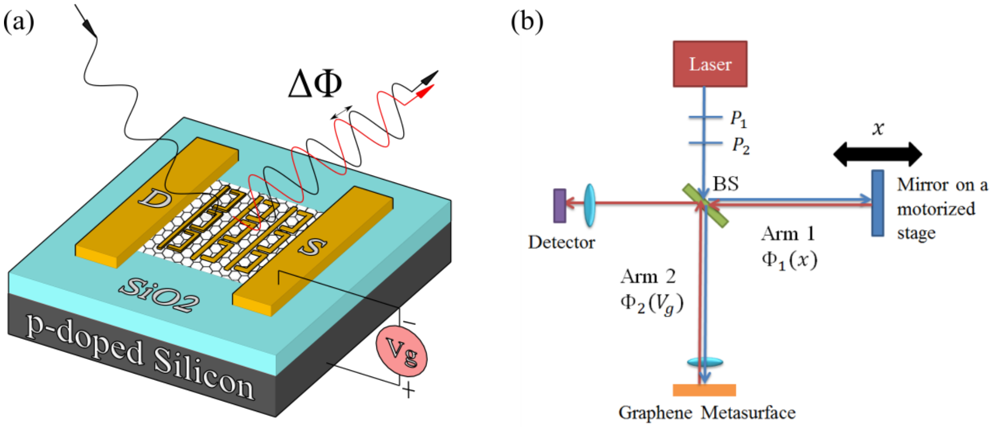

Figure 5.2: Schematic for graphene-induced phase modulation of the reflected light waves. The plasmonic metasurface is fabricated on top of a single layer graphene (SLG). Source (S) and drain (D) contacts are attached to SLG for its electrical characterization. The phase modulation $\Delta\Phi$ is a function of the gate voltage V_g applied across the insulating SiO2 spacer. (b) Experimental setup for the phase measurement: a Michelson interferometer with a beam-splitter (BS) and two polarizers P_1 and P_2 used to adjust the power and set the polarization of the infrared beam. The active graphene-integrated metasurface placed in the test arm (Arm 2) induces a voltage-tunable phase shift $\Phi_2(V_g)$, and the moveable mirror on a motorized stage placed in the reference arm (Arm 1) induces a displacement-tunable phase shift $\Phi_1(x)$.

with a narrowband dark mode[97]. The continuous wire of this structure mimics a dilute plasma and provides a broadband background. The structure supports a dark mode with quadrupolar charge distribution, which manifests as a minimum in reflection spectrum.

At the resonance, the current density of the dipole and the wire are anti-symmetric as shown in Fig. 5.3a. The interaction of light and graphene is proportional to $|E_t^2|$ [57,99]

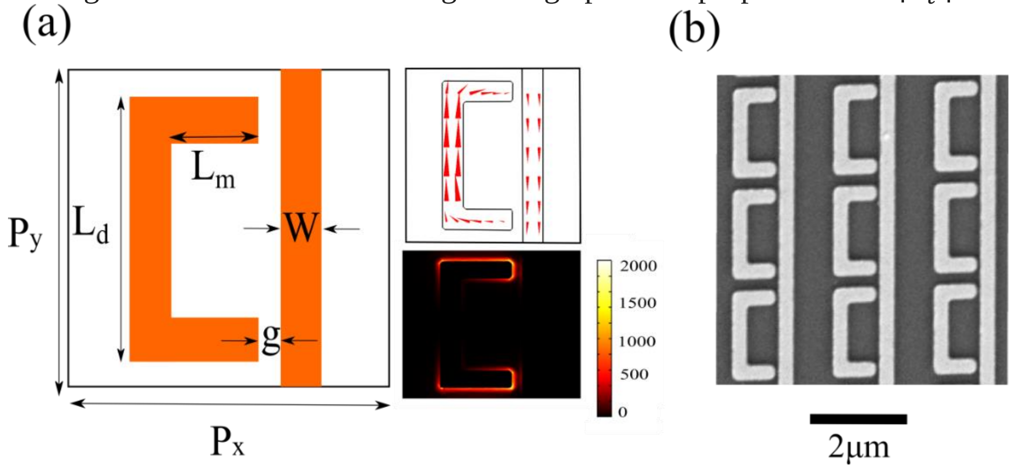

Figure 5.3: **(a)** The unit cell of the metasurface with the following dimensions: $g = 120\,nm, L_d = 1.8\,\mu m, L_m = 600\,nm$, the width of all the wires $W = 250\,nm$ and the periodicity in both directions $P_x = P_y = 2.1\,\mu m$. The current profile at the reflectivity minimum for the structure without graphene is shown on the top right. The current is plotted 5 nm above the SiO2 surface. Near-field enhancement $\left|E_t^2/E_{inc}^2\right|$ at the Fano resonance frequency is plotted at the graphene plane (bottom right). **(b)** An SEM picture of the metasurface. The black scale bar represents 2 micron.

where E_t is tangential electric field at the graphene surface. The field enhancement defined by $\left|E_t^2/E_{inc}^2\right|$ at the resonance is shown in Fig. 5.3a where E_{inc} is the incident field. An SEM picture of the metasurface is shown in Fig. 5.3b.

The metasurface is fabricated on top of SLG and an electrostatic gate voltage V_g is applied between the silicon backgate and the graphene to change the carrier concentration n of SLG which controls the optical conductivity of graphene. A list of the experimentally applied gate voltages and the corresponding graphene's Fermi energies is listed in Table 1. The electric fields $E = V_g/d$ inside the silicon oxide spacer of thickness

$d = 1\mu m$ separating the SLG from the back gate are tabulated as a function of the applied gate voltage V_g.

V_g (V)	E(MV/cm)	E_F(eV)
-40	-0.4	0.08
-20	-0.2	0.09
0	0	0.10
30	0.3	0.12
80	0.8	0.15
150	1.5	0.18
280	2.8	0.23

Table 5.1: Fermi energies E_F in the SLG and the corresponding electric fields $E = V_g/d$ inside the silicon oxide spacer of thickness $d = 1\mu m$ separating the SLG from the back gate are tabulated as a function of the applied gate voltage V_g.

The simulated reflectivity and reflection phase for Y-polarized light at normal incidence for different Fermi energies is shown in Fig. 5.4a,b. The reflectivity of our sample is measured using laser spectroscopy. The source is a quantum cascade laser (Daylight solution, MIRcat-1400). The laser light is split into two arms by a beam splitter (CaF_2 2-8 um). The results for different gate voltages are shown in Fig. 5.4c. The experiment is performed at normal incidence and for the light polarized along the dipole (Y-direction). The setup shown in Fig 5.2b was used to measure the optical spectroscopy of the sample where the arm 1 is blocked by IR absorbing material and the only detected signal is from the graphene metasurface. The laser was operated on pulsed mode with pulse repetitions rate of $250\ KHz$ with the pulse duration of $100\ ns$. A MCT detector was utilized for the measurement of intensity. The signal was amplified by a lock-in amplifier model (Stanford research systems SR844) with an integration time of 3 ms. A high numerical aperture NA=0.5 ZnSe lens was used as the objective.

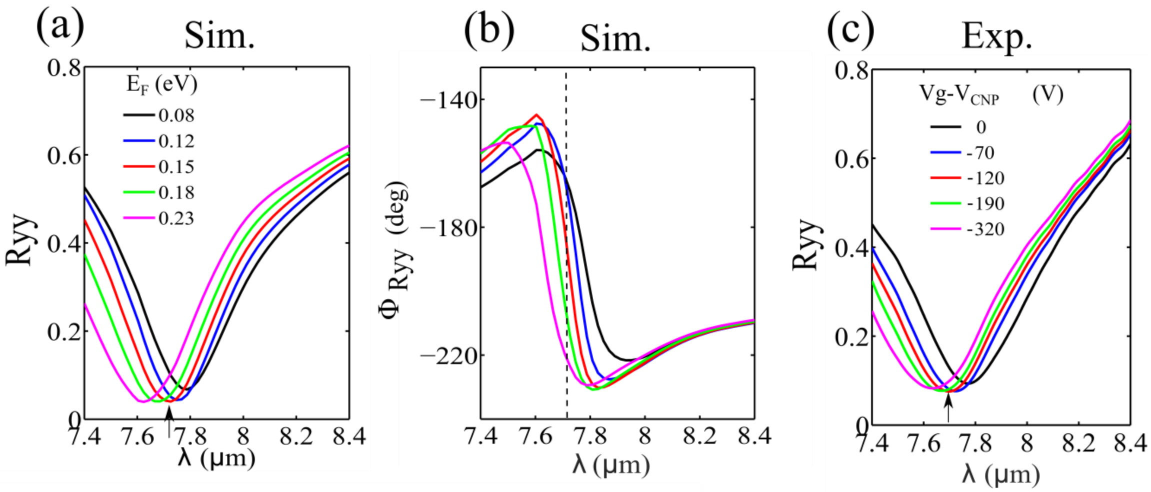

Figure 5.4: (a) The simulated metasurface reflectivity spectrum for normal incidence with Y-polarized light. The colors represent different Fermi energies of the graphene. (b) The simulation results for reflection phase. Excitation parameters is similar to (b) (c) The measured reflectivity for y-polarized incident light at normal incidence. Different voltages have been color-coded according to their correspondent Fermi energy in (a)

The gate voltages in Fig 5.4c correspond to the Fermi energies in Fig. 5.4a and there is a good agreement between the measured and simulated reflectivity.

5.3 SAMPLE FABRICATION

The processes used for fabrication of the sample were similar to the process explained in section 4.7 with the details and recipes given in Appendix A and B. The only difference is that a Ni (15 nm) and Au (80 nm) contact was deposited on the back-gate to lower the contact resistance between the gold pads of the chip carrier and the silicon.

5.4 ELECTRICAL TRANSPORT MEASUREMENT

We used a parametric analyzer (Keithley 2450) for the current-voltage (I-V) measurement to characterize the SLG. In Fig. 5.5 the resistance between drain and source contacts R_{DS} is shown as a function of gate voltage. The maximum resistance corresponds to charge neutrality point of graphene. For our sample $\mathrm{V_{CNP}} \cong 40$ V.

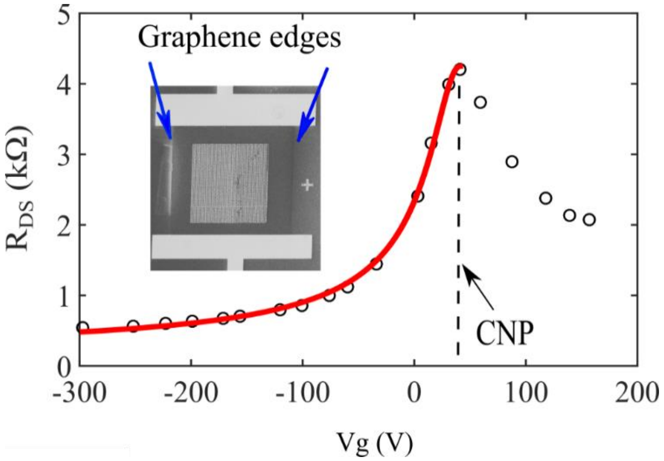

Figure 5.5: Electrical transport measurement for graphene: the resistance between the drain and the source contact (R_{DS}) as a function of gate voltage V_g. The inset shows the graphene metasurface integrated with graphene with the drain and source contacts.

A fitting procedure was used to determine the electrical properties of the sample and graphene as detailed in appendix D section b.

5.5 INTERFEROMETRIC MEASUREMENT

We used a Michelson interferometer as shown in Fig. 5.2b to measure the phase modulation of the reflected plane wave due to graphene gating. A quantum cascade laser is used as the light source. The laser light is split into two arms by a beam splitter (CaF2 2-8 µm). On arm 1, the beam is reflected from a mirror mounted on a motorized stage whose motion is controlled by a closed-loop actuator with optical encoding capability. On arm 2, the graphene-integrated metasurface is mounted. The reflected wave (marked by red arrows in Fig. 5.3b) combine on the beam-splitter (BS) and an MCT detector measures the resulting interference signal. The interfered wave can be described as:

$$\mathrm{C}\left(\mathrm{x},\mathrm{V_g},\mathrm{t}\right) = \mathrm{A}\sin\left(\omega\mathrm{t}+\Phi_1(\mathrm{x})\right)+\mathrm{B}\left(\mathrm{V_g}\right)\sin\left(\omega\mathrm{t}+\Phi_2\left(\mathrm{V_g}\right)\right), \tag{5.1}$$

where A and $\Phi_1(\mathrm{x})$ are the amplitude and the position-dependent phase of the waves from arm 1, respectively. $\mathrm{B}(\mathrm{V_g})$ and $\Phi_2\left(\mathrm{V_g}\right)$ are the amplitude and the voltage-dependent phase of the reflected wave from the graphene-integrated metasurface, respectively. From eq 5.1, the time-averaged intensity is:

$$\left|\mathrm{C}(\mathrm{x},\mathrm{V_g})\right|^2 = \frac{|\mathrm{A}|^2}{2}+\frac{\left|\mathrm{B}(\mathrm{V_g})\right|^2}{2}+\mathrm{A}\mathrm{B}(\mathrm{V_g})\cos(\Phi_1(\mathrm{x})\text{-}\Phi_2\left(\mathrm{V_g}\right)), \tag{5.2}$$

where $\left|\mathrm{C}(\mathrm{x},\mathrm{V_g})\right|^2$ is the measured intensity for position x of the mirror and graphene gate voltage $\mathrm{V_g}$. Equation 5.2 consists of a DC offset (first two terms on the right hand side) and an interferometric part (last term in the right hand side). To characterize $\Phi_2\left(\mathrm{V_g}\right)$, we set the voltage to $\mathrm{V_g} = 0$ V and move the mirror with constant step sizes, measuring the intensity after each step to record a few full-wave interferometric oscillations of the intensity. We then return to the original position, change the voltage to $\mathrm{V_g} = \mathrm{V_1}$ and go forward for the same number of steps. Finally we return to the original position at $\mathrm{V_g} = 0$ V. The schematic in Fig. 5.8b summarizes the above-mentioned movement of the actuator that is used to measure the phase change between $\mathrm{V_g} = 0$ V and $\mathrm{V_g} = \mathrm{V_1}$. By using a least-square fitting of the measured interferometric data to a cosine function with an offset: $\mathrm{a}(\mathrm{V_g})\cos\left(\mathrm{bx}+\mathrm{c}(\mathrm{V_g})\right)+\mathrm{d}(\mathrm{V_g})$ we can find the fitting parameters of

$\mathrm{a(V_g), b, c(V_g)}$ and $\mathrm{d(V_g)}$ where $\Phi_1(\mathrm{x}) = \mathrm{bx} + \Phi_1(0)$ and $\mathrm{c}(\mathrm{V_g}) = -\Phi_2(\mathrm{V_g})$. Here $\Phi_1(0)$ originates from the difference between the path lengths of two arms. By comparing the fitted parameters for the two forward directions at to $\mathrm{V_g} = 0\,\mathrm{V}$ and to $\mathrm{V_g} = \mathrm{V_1}$, the phase change can be calculated from:

$$\Delta\Phi(\mathrm{V_g}) = [\Phi_2(\mathrm{V_g}) - \Phi_2(\mathrm{V_{CNP}})] = c(V_{CNP}) - c(V_g). \tag{5.3}$$

The normalized interferometric signal can be defined from the fitted parameters:

$$\mathrm{I_N}(\mathrm{x}, \mathrm{V_g}) = \frac{|\mathrm{C}(\mathrm{x}, \mathrm{V_g})|^2 - \mathrm{d}(\mathrm{V_g})}{\mathrm{a}(\mathrm{V_g})}. \tag{5.4}$$

In Fig. 5.4a, $I_N(x, V_g = 0\text{ V})$ and $I_N(x, V_g = -150\text{ V})$ are shown with green and blue circles respectively where $x = sN_x$ is the mirror position and N_x are the number of minimum step size and s is the minimum step size of the actuator. The fitted curves are demonstrated by the red and black solid lines in Fig. 5.4a. The x-axis is the number of minimum step sizes. In principle the fitting parameter b is equal to $b = 4\pi/\lambda$ where λ is the wavelength of light. However to characterize the actuator step size with a finite error, we keep it as a fitting parameter. After fitting the interferometric signal in the two forward direction, we notice that b_{f1} and b_{f2} (parameter b for the first and second forward direction) in all the experiments are roughly equal with 0.5 % maximum error for all of our experiments. To minimize this error, we define $b = (b_{f1} + b_{f2})/2$ and use it in the fitting procedure mentioned earlier. In addition, from the fitting we find the minimum step size of the actuator to be $s \approx 68\,nm$. Each actuator jump consisted of 8 minimum step sizes. The integration time for intensity measurement was set to be 100 ms and there is a 200ms delay time after an actuator jump till the intensity is measured.

The procedure for phase modulation calculation between $V_g = 0$ and $V_g = V_1$ can be summarized as the following:

- Apply $V_g = 0$, move the mirror in the forward direction for certain number of actuator jump.
- Move backward at $V_g = 0$ return to the original position.
- Change the voltage to $V_g = V_1$ move forward for the same number of actuator jumps
- Return to the original position at $V_g = 0$
- Fit the forward curves for intensity to $a(V_g)cos(bx + c(V_g)) + d(V_g)$, which gives fitted values of $b_{f1}$and b_{f2}.
- Assign $b = (b_{f1} + b_{f2})/2$
- Fit the two curves again to $a(V_g)cos\left(bx + c(V_g)\right) + d(V_g)$
- $\Delta\Phi(\mathrm{V_g}) = c(V_{CNP}) - c(V_g)$

The gate voltage was reset to $V_g = 0$ before each measurement, in order to avoid the potential hysteretic interfacial effects[117] (e.g. charge trapping and redox reaction) that takes place at high gate voltages. To confirm that the hysteretic effects does not affect our measurement, we calculate the variation of $c(V_g = 0)$ (when moving in the forward direction at $V_g = 0$) for different voltages. The results are shown in in Fig. 5.6 where the y-axis is $c(V_g = 0)$ in degrees. The small error of around 1 degree ensures that E_F returns to the same value each time we reset to $V_g = 0$.

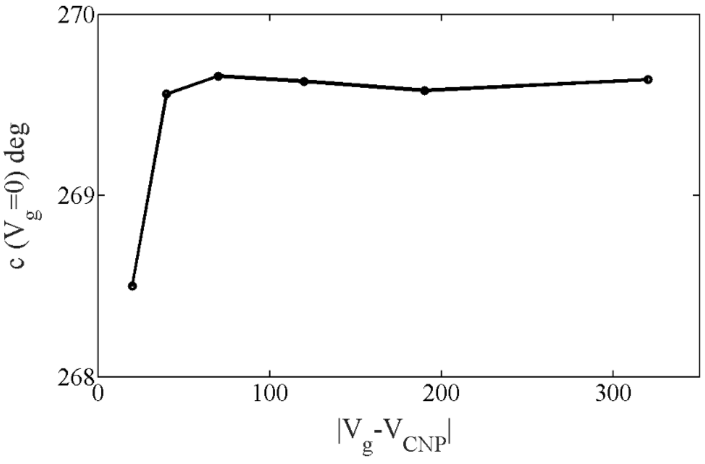

Figure 5.6: Variations of $c(V_g = 0)$ in degree as a function of gate voltage.

The results of our interferometric experiments are shown in Fig. 5.7. In Fig. 5.7b, the fitted curves to $I_N(x, V_g)$ are demonstrated for three different Fermi energies at $\lambda_0 = 7.69\ \mu m$. The x-axis is the mirror movement normalized to the wavelength. The total phase shift for the Y-polarized light is about $\Delta\Phi(V_g = 280V) \approx -55°$(corresponding to $E_F = 0.23eV$). To make sure our measurement results are reproducible we perform the phase measurement experiment 3 times. The robustness and repeatability of the phase shift is confirmed by repeating the experiments three times and plotting the measured phase shifts for the three trials in Figure 5.7c. We speculate that the repeatability can be further improved by graphene's passivation that can be achieved by, for example, depositing an insulating layer of Al2O3[116,117] or boron nitride (BN)[118] over the SLG and fabricating the metasurface on top of it.

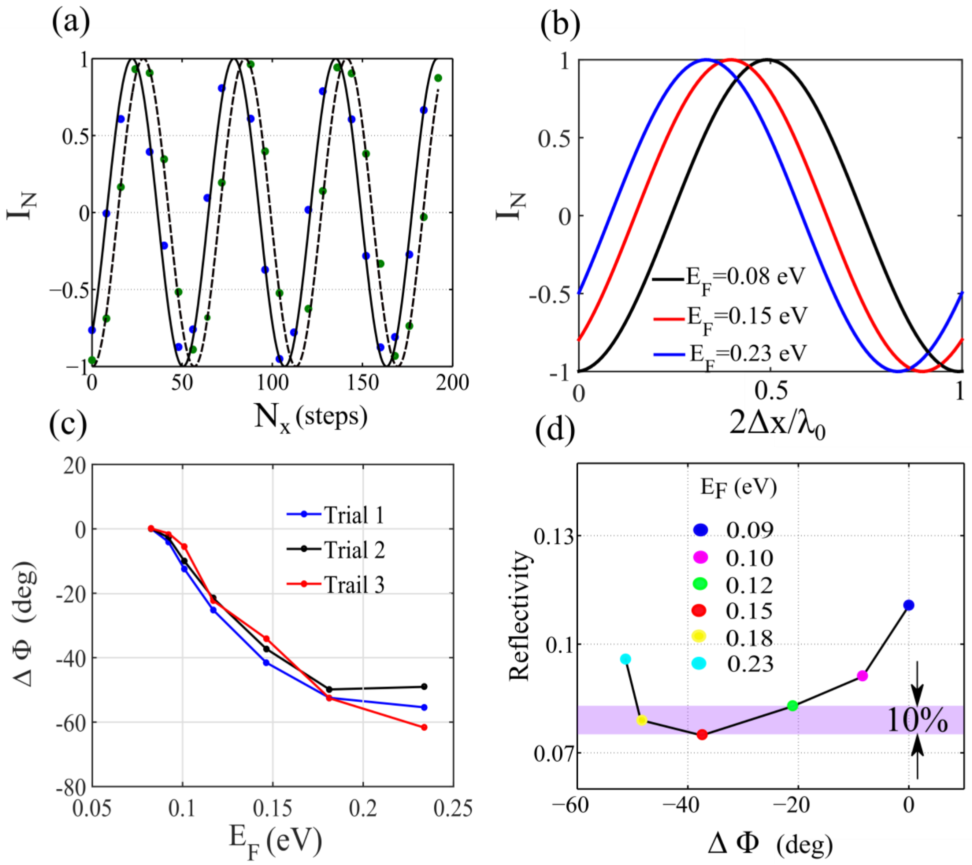

Figure 5.7: **(a)** The Interference for two different voltages: the x-axis shows mirror position in units number of minimum step sizes of roughly 68 nm. The dots represent normalized interference data I_N as defined by eq 5.4 for $V_g = 0$ V (green) $V_g = -150$ V (blue). These data are fitted to $cos(bx + c(V_g))$ where b and $c(V_g)$ are the fitting parameters and $x = N_x s$. All the experiments are run at $k_0 = 1300\, cm^{-1}$ ($\lambda_0 = 7.69\, \mu m$). For each gate voltage the actuator moves for 25 jump in one direction. **(b)** Fitted interference patterns as (a), but plotted for three values of E_F (black: $E_F =$ 0.08 eV, red: $E_F = 0.15$ eV, blue: $E_F = 0.23$ eV) over one oscillation period $0 < x < \lambda_0/2$. **(c)** The results of three independent interferometric measurement trials: Phase change $\Delta\Phi$ as a function of Fermi energy. The phase change is measured with respect to $V_g = V_{CNP}$ ($E_F = 0.08$ eV). The incident field was polarized along Y-direction. These three curves show the reproducibility of the experimental results **(d)** The results of trial1 is shown in the reflectivity-phase plane. The reflectivity changes about 10 % in the colored region while the phase is changing by about 28 degrees.

In Fig. 5.7d the phase shift results of trial1 is shown in reflectivity-phase plane. Different Fermi energies are shown by different colors. The reflectivity in the colored region changes only about 10 % whereas the phase is changing by about $\Delta\Phi \approx -28$ degrees. The property of the pure phase shift at a constant reflectivity is promising for realizing fast phase modulators, as well as in other optical applications.

5.6 APPLICATIONS OF PHASE MODULATION

5.6.1 Motion detection

The concept of interferometric motion detection using an active graphene integrated metasurface illustrated in Fig. 5.8a is explained by observing that the test and reference arms of the Michelson interferometer can, in principle, be exchanged. That means that, instead of using the known $\Phi_1(x)$ to measure the unknown $\Phi_2(V_g)$, we can now use the tabulated $\Phi_2(V_g)$ to measure the unknown Φ_1. If an arbitrary reflecting object moving along the $x = x_{obj}(t)$ trajectory is used instead of the mirror, then extracting $\Phi_1(x_{obj})$ would enable tracking its motion. Such tracking requires that the phase shift $\Phi_2(V_g)$ in Arm 2 (which becomes the new reference arm) be changed on the

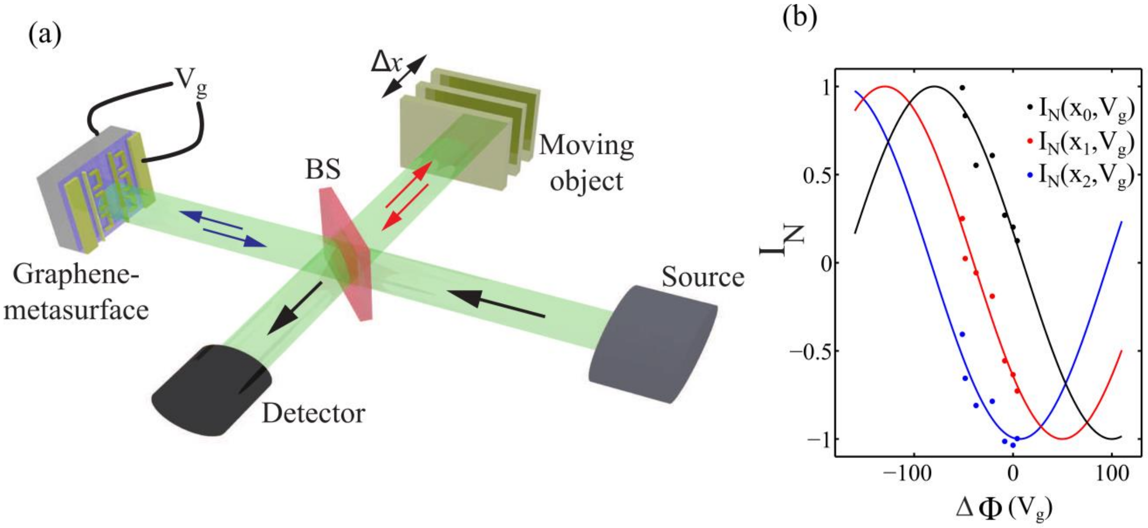

Figure 5.8: **(a)** Schematic of the interferometric motion detection using a graphene integrated metasurface. The motion of the reflecting object (mirror on a moving stage) is detected by varying the phase of the reflected light from the graphene integrated metasruface via field-effect gating. **(b)** Normalized interferograms $I_N(x_j, V_g)$ plotted for three mirror positions $x_j = x_0 + j\Delta x$ ($\Delta x = 540nm$ corresponds to 8 steps of the moving stage, $j = 0,1,2$ for black, red, and blue symbols, respectively) and seven voltages from Table 1. Horizontal axis: $\Delta\Phi(V_g)$ from Fig. 5.7c (Trial 1).

time scale which is much shorter that the object's movement. The experimentally obtained plot of $\Delta\ \Phi\,(V_g)$ presented in Fig. 5.7c serves as a look-up table for measuring the movement of the reflecting object (e.g. a moving mirror). The key advantage of the non-mechanical change of $\Phi_2$is the speed (tens of GHz) at which such change can be accomplished.However, there is a significant difference between measuring $\Phi_2(V_g)$ using a sequence of $\Phi_1(x_j)$ spanning several periods (where $0 < x_j < sN_{max}$) as it was done Fig. 5.7a, and extracting $\Phi_1(x_{obj})$ using a sequence of $\Phi_2(V_g = V_k)$ spanning a fraction of a radian. The accuracy of the latter simulation may be potentially limited because of the smaller phase change in the reference arm. To investigate the spatial resolution of a graphene-based distance measurement interferometer, we have selected six mirror position triplets $x_j = x_0 + j\,\Delta\,x$ (where $j = 0{,}1{,}2$, $\Delta x = 0.54\mu m$, and x_0 is different for different triplets) and plotted the normalized interferograms $I_N\left(x_j, V_k\right)$ as a function of $\Delta\,\Phi\,(V_k)$ for the seven voltages listed in Table 5.1.The experimental results for one such triplet is shown in Fig. 5.8b, where the black, red, and blue symbols correspond to x_0, x_1, and x_2 members of the triplet, respectively. The data was fitted to $I_N\left(x_j, V_k\right) = \cos\left[\Psi_j - \Delta\;\Phi_2(V_k)\right]$ (solid lines), where $\Psi_j = 4\pi x_j/\lambda + \mathit{\Phi}_1(0) - \Phi_2(V_{CNP})$ follows from the definition of $I_N(x, V_g)$. Using $\Psi_j - \Psi_0 = 4\pi\left(x_j - x_0\right)/\lambda$, the relative distances $(x_1 - x_0)$ and $(x_2 - x_0)$ were measured and plotted in Fig. 5.8c for all six (x_0, x_1, x_2) position triplets. Note that this technique does not attempt to extract the absolute distances.

Next, we demonstrated that the accuracy of the displacement measurement is high despite the fact that the phase change in the reference arm of the interferometer is less than one radian according to Fig. 5.8b. Figures 5.9a,b illustrates the accuracy of the measurement by plotting the extracted positions of x_1 and x_2 (referenced to x_0) for all the 23 triplets. For simplicity we assume $x_0 = 0$. The black solid dots, represent the calculated position for a certain triad number. The red lines correspond to mean value of position: $\overline{x_1} = 0.542\mu m$ and $\overline{x_2} = 1.083\mu m$ and the black lines show the standard deviation for positions. The standard deviation for positions x_1 and x_2 were calculated to be $\sigma_1 = 33\ nm$ and $\sigma_2 = 47\ nm$ which also determine the error bar of our measurement for the two measurements. Figure 5.9c summarizes these calculations. The dashed blue line is drawn at 45 degrees to illustrate the agreement between the actual displacements of the mirror (horizontal axis) and the displacement measured using the graphene-based interferometer. The red solid dots shows the mean value of our measurements and the error bars are shown similar to Figures 5.9a,b by the black lines. These data indicate that displacement as small as $\Delta x = 540nm$ can be measured with $\pm 33nm$ accuracy which is roughly $\pm$ 6% error. For displacement of $\Delta x = 1080nm$ the error is $\pm 47nm$ which is roughly $\pm$ 4.5% error. In addition, no assumption of constant (distance-independent) reflectivity from the moving object is needed for the application of this technique.

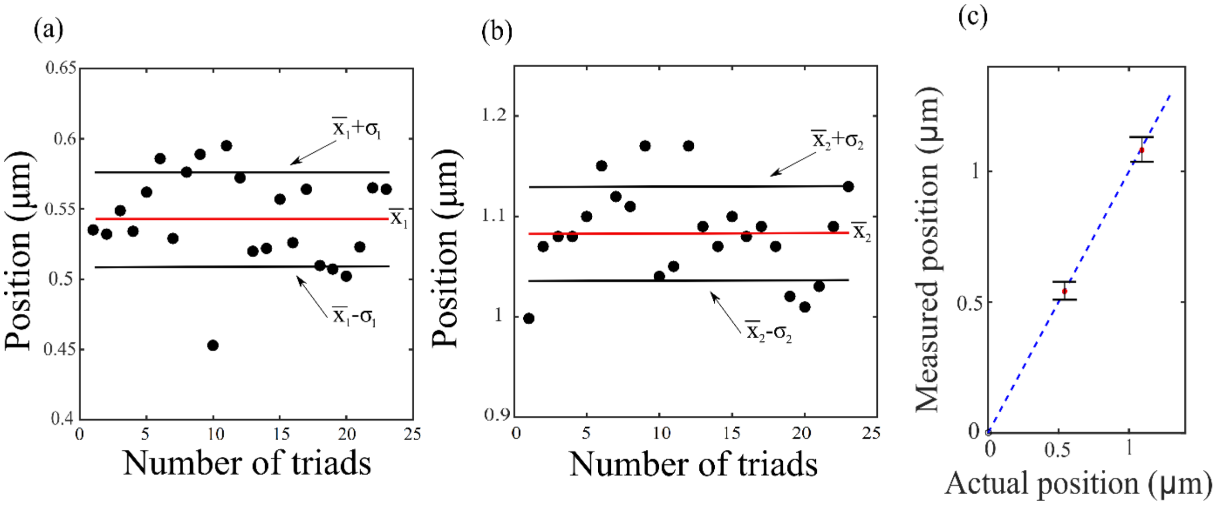

Figure 5.9: The extracted relative displacements $(x_1 - x_0)$ **(a)** and $(x_2 - x_0)$ **(b)** for 23 triplets from the 25 data points (corresponding to 25 actuator jumps) are shown by black solid dots. The solid red lines correspond to the mean value of $\overline{x_1}$ and $\overline{x_2}$ whereas the black lines show the error bar determined by the standard deviation $\sigma_1$and σ_2. For simplicity, x_0 is assumed to be zero **(c)** The mean value and error bar of the displacement measurement are shown with solid red dot and black lines. A blue dashed line is drawn at 45° to compare the extracted and actual mirror positions. All measurements are performed at $\lambda = \lambda_0$.

The distance measurement technique based on active graphene integrated metasurfaces demonstrated above is a potential alternative to the more conventional chirp-based techniques[119] because it is carried out in mid-IR, where atmospheric light scattering is considerably reduced[120] and passive chirping outside of the laser is challenging, and at potentially high (multi-GHz) speeds.

5.6.1.1 Maximum traceable object velocity:

It would be interesting to know how fast of an object can be traced using with the motion sensing technique described in 5.6.1 for a given tolerable error. We start by estimating the speed of our device. To simplify, we neglect the parasitic capacitance of the circuit and also assuming $R_{DS} = 1k\Omega$. From capacitance per area of our device $C_g \approx 2nF\ cm^{-2}$, the response time of our sample is roughly $\tau \approx 0.2ns$. Therefore, it take at least $\Delta T = 1.4ns$ to take 7 data points of Fig. 5.6b. This corresponds to 55 degree phase modulation. Assuming we can tolerate 20% error and reminding that $\Phi_1(\mathrm{x}) = \frac{4\pi}{\lambda}\mathrm{x} + \Phi_1(0)$, the distance that the mirror can move while the gate voltages are changing can be estimated by $\Delta x = \frac{\Delta\Phi_1\lambda}{4\pi} \approx 117\ nm$ where $\Delta\Phi_1 = 11° = \frac{11\pi}{180}$ rad. The maximum velocity of the mirror that can be traced will then be $V_{M-max} = \frac{\nabla x}{\nabla \mathrm{T}} \approx 84\ \mathrm{m/s}$. It should be noted that the maximum velocity in linearly related to error. For example for 10% of tolerable error the maximum velocity will decrease by a factor of 2.

5.6.2 Application in polarization conversion

The second application enabled by voltage-controllable Graphene-integrated metasurfaces is the development of electrically tunable wave plates that can control the polarization state of the reflected mid-IR light in real time. Because the utilized metasurface (see Fig. 5.3a) is strongly anisotropic, its response to x −polarized light is very different from the resonant response to y −polarized light considered so far. Specifically, while strong Fano resonance at $\lambda = \lambda_0$ occurs for the latter, no such resonance exists for the former. In the absence of resonance, no significant phase variation is expected for reflected x −polarized light as the gate voltage is varied. This is confirmed by our interferometric measurement, the results of which are described in Fig. 5.7a, where the experimentally obtained phase changes at $\lambda = \lambda_0$ for both x and y polarized light at normal incidence are plotted as functions of graphene's Fermi energies $E_F(V_g)$ taken from Table 5.1. Both experimentally measured $\Delta\Phi_x(V_g)$ and $\Delta\Phi_y(V_g)$ are in good agreement with numerical simulations (Fig. 5.7c). Note that the theoretically and experimentally obtained reflection phases are referenced to those at the CNP point of graphene. The absence of the metasurface's resonant response to x −polarized light is also experimentally confirmed by featureless reflectivity $R_{xx}(\lambda)$ that does not appreciably change with E_F as shown in Fig. 5.7b. Note that the x − and y −axes are the principal axes of the metasurface (i.e. $R_{xy} = 0$) due to the mirror reflection symmetry of the structure with respect to the x −axis.

The action of an active phase plate is easily captured by examining the polarization state of the reflected light that is polarized at 45°with respect to the principal (x and y) axes of the graphene-integrated metasurface at incidence. The resulting (un-normalized) polarization ellipse is given by the following parametric formula:

$$\begin{aligned} E_x(V_g) &= \sqrt{R_{xx}}\cos[\alpha_{xy}(V_g) - \omega t], \\ E_y(V_g) &= \sqrt{R_{yy}}\cos[\omega t] \end{aligned} \tag{5.5}$$

where $0 < \omega t < 2\pi$ is a parameter, the two polarized reflectivities ($R_{xx}$and R_{yy}) may be voltage-dependent, and the reflected phase shift $\alpha_{xy} = \Delta\Phi_x(V_g) - \Delta\Phi_y(V_g) + \alpha_{CNP}$ between the two polarizations is also controlled by the gate voltage.

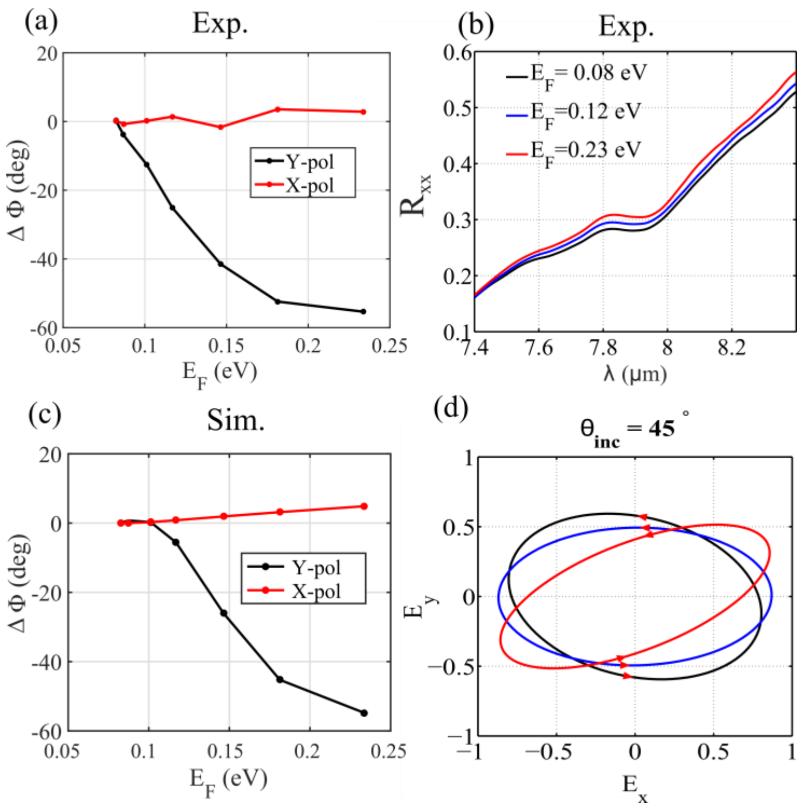

Figure 5.10: (a) Measured phase shifts $\Delta\Phi_x$ and $\Delta\Phi_y$ of the linearly polarized light reflected at normal incidence from the voltage-controlled graphene-integrated metasurface. Red line: x −polarised, black line: y −polarized light, horizontal axis: graphene's Fermi energy. **(b)** Measured reflectivity for x −polarised incident light corresponding to three Fermi energies. **(c)** Simulated phase shifts $\Delta\Phi_x$ and $\Delta\Phi_y$ plotted as a function of the Fermi energy. **(d)** Normalized polarization ellipses of the reflected light calculated using eq 5.5 and the experimentally obtained $\Delta\Phi_x$ and $\Delta\Phi_y$ from panel (a). The constant $\alpha_{CNP} = 107°$ was extracted from COMSOL simulations. Incident light's polarization at 45° with respect to the principal axes of the metasurface was assumed. The colors correspond to the Fermi energies from panel (b). All measurements and simulations correspond to the wavelength of light ($\lambda = \lambda_0$) that corresponds to the minimum of $R_{yy}(\lambda)$ at $E_F =$ 0.15 eV. In simulations $\lambda_0^{(\mathrm{th})} = 7.72\mu m$ was used.

. Here, $\alpha_{CNP} \equiv \Delta\Phi_x(V_{CNP}) - \Delta\Phi_y(V_{CNP})$ is the phase shift at the V_{CNP}. Here we focus on the case whereR_{xx} and R_{yy} are nearly voltage-independent as can be observed from the experimental data presented in Fig. 5.7b. However, the significant (by almost a full radian) voltage-induced $\Delta\Phi_y$ translates into an equal magnitude shift of α_{xy}, and, therefore, a significant rotation of the polarization ellipse. Three such normalized polarization ellipses are presented in Fig. 5.7d for the corresponding gate voltages and graphene's Fermi energies extracted from Table 1. These results indicate that both the ellipticity and the orientation of the polarization ellipse can be significantly altered by applying a gate voltage. For example, we observe from Fig 5.7d that the direction of the major axis can be moved from the second quadrant (at $E_F = 0.08\ eV$) to the first quadrant (at $E_F = 0.23\ eV$). Note that such orientation of the polarization ellipse is enabled by the voltage-induced phase shift, and cannot be accomplished by pure amplitude modulation of either $R_{xx}(V_g)$ or $R_{yy}(V_g)$. This implies that only a limited subspace of Stokes parameters of the reflected light can be accessed by pure amplitude modulation. For example, if the major axis of the polarization ellipse is restricted to stay in the first quadrant, then only the positive values of the second Stokes parameter $S_2 \equiv I(+45°) - I(-45°)$, defined as the intensity difference of light passing through the analyzers oriented at $+45°$ and $-45°$ degrees with respect to the principal polarization axes, can be accessed. In contrast, phase modulation demonstrated here does not suffer from such restrictions. Therefore, one may envision using phase-shifting graphene-integrated metasurfaces for real-time ellipsometric applications[121] that require high time resolution. The mathematic analysis and data processing in this section was performed by Dr. Shourya Dutta Gupta.

5.7 PRELIMINARY PHASE MODULATION MEASUREMENTS USING AN OPEN-LOOP ACTUATOR

In this section, additional examples of phase modulation measurement are provided for two other devices. The main difference of these experiments compared to the one described in section 5.5 is that an open-loop actuator was utilized in arm1. An open-loop actuator is not equipped with an optical encoding system and therefore the movement is not as accurate as a closed-loop actuator. To reduce the error, we used slightly different procedure for phase measurement where the mirror is not returned to the original position when the voltage changes. The procedure can be summarized as such:

- Assign $V_g = V_1$ move forward for a few periods
- Change the voltage to $V_g = V_2$ move forward.
- Keep moving forward for all N gate voltages
- Fit all the interference signals measured to $a(V_g)cos\big(bx + c(V_g)\big) + d(V_g)$
- Assign $\mathrm{b_{average}} = \Sigma \mathrm{b_i}/\mathrm{N}$
- Fit the two curves again to $a(V_g)\ cos\big(\mathrm{b_{average}}x + c(V_g)\big) + d(V_g)$
- $\Delta\Phi\big(V_g\big) = c(V_{CNP}) - c\big(V_g\big)$

Fig 5.8a,b compares the mirror stage movement procedure for the open-loop and close-loop actuator (section 5.5). With an open-loop actuator the mirror is not returned to the original position which was mainly to avoid the backlash effect which originates from in-accurate step size of the actuator when the motion is reversed. It should be noted that resetting to $V_g = 0$ after each gate voltage as was done in section 5.5 and as shown in Fig. 5.8b helps to reduce the measurement error. Without this resetting, graphene is exposed to high gate voltages for longer time during the phase modulation experiment leading to larger error from the redox effect. Interferometry measurement were performed using the setup of Fig. 5.2b and for two different samples using an open-loop actuator. 1) The metasurface design introduced in Fig 4.2 and 2) the design in Fig 5.3a. Figure 5.9 shows the experimental results for the double-Fano resonance structure of Fig. 4.2a. The dimensions are given in the caption of Fig. 5.9 and are different from those in Fig 4.2a.The reflectivity spectrum for three different voltages given in the legend is shown. The CNP point for this device is at $V_g = 300V$.

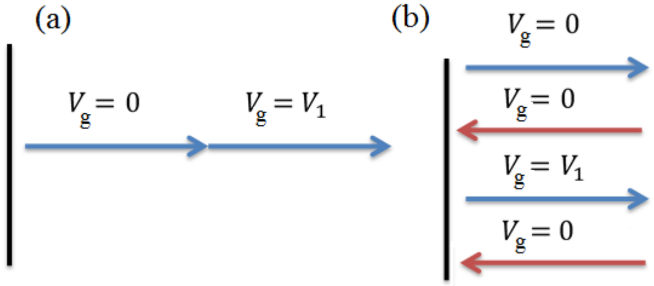

Figure 5.11: (a) With an open loop actuator, the mirror moves in the forward direction for all voltages (b) By using a closed-loop motor we return to the original position after each voltage change

Considerable blue-shift is obtained as the gate voltage changes from CNP point to $V_g = 250V$ with a total $\nabla V_g = 550V$ which corresponds to the Fermi energy of $E_F = 0.3\ eV$. The phase modulation was measured at two different wavelength shown by the red and black arrows. At both of these wavelengths the reflectivity is almost constant as the Fermi energy changes. The red arrow points at $\lambda = 5.69\ \mu m$ which is the reflectivity peak between the dipole and monopole mode. The black arrows is at $\lambda = 6.42\ \mu m$: the reflectivity minimum for $V_g = 100\ V$. In Fig. 5.9b, the reflectivity and phase modulation are shown as a function of Fermi energy for both wavelengths. Different colors of the solid circles represent various Fermi energies. The phase modulation at $\lambda = 5.69\ \mu m$ is around 17 degree while the reflectivity is almost constant and slightly above $R \approx 0.3$ as the Fermi energy changes from $E_F = 0.1\,eV$ and $E_F = 0.3\,eV$. At $\lambda = 6.42\,\mu m$, the phase modulation is around 40 degrees while the reflectivity is roughly constant around $R \approx 0.07$. In Fig. 5.10 the result of phase modulation measurement of the metasurface design in Fig 5.3a is shown where an open-loop actuator was used in the measurement. It should be noted that the measurement was performed on a different sample than the sample used in section 5.5.

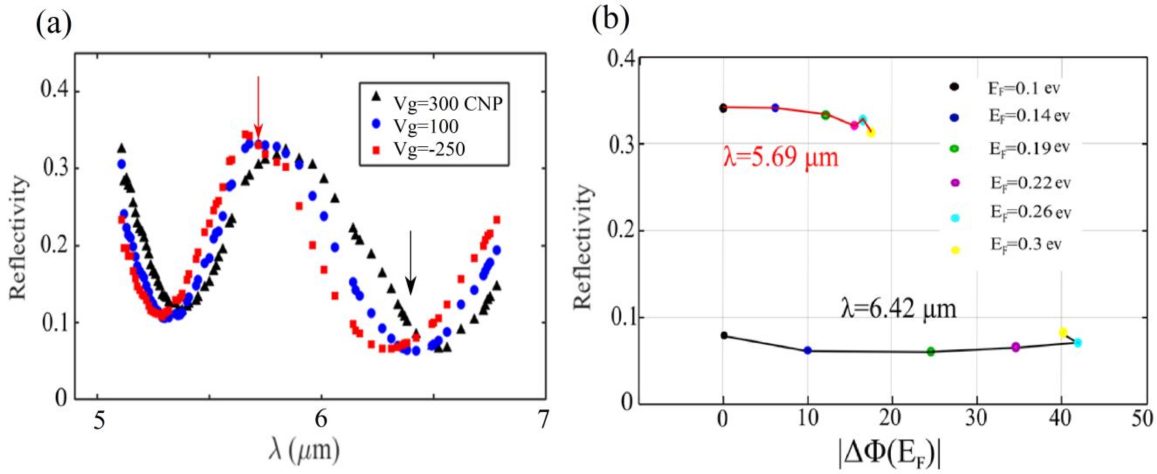

Figure 5.12: (a) The reflectivity of the sample in Fig 4.2a measured by a QCL at normal incidence. The dimensions of the structure are $P_x = P_y = 2.4\mu m, L_x = 0.54\mu m, L_m = 0.6\mu m, L_y = 0.96\mu m$, and $w = 0.24\mu m$ and $G = 70nm$. (b) The phase modulation and reflectivity as a function of Fermi energy for two wavelength shown by the red and black arrows in (a).

The reason for additional experiments of section 5.5 and fabrication of a new sample was to use a closed-loop actuator with smaller movement error as mentioned earlier. The FTIR measurement results are shown in Fig 5.10a where Fermi energy changed from $E_F = 0.08\,eV$ and $E_F = 0.24\,eV$. The phase modulation at $\lambda = 7.57\,\mu m$

was measured using a QCL and the interferometric setup of Fig 5.2b. A phase modulation of around 85 degrees is achieved as the Fermi level changes from $E_F = 0.08\,eV$ and $E_F = 0.29\,eV$ which is larger than the phase modulation achieved in section 5.5. In addition the reflectivity stays constant around $R \approx 0.05$ while the phase changes by about 40 degrees. It should be noted that a lower reflectivity minimum and higher Fermi energy might explain the higher phase modulation. However it is difficult to compare these two measurements as the metasurface quality, graphene quality, the actuator accuracy and the measurement procedure used in the experiment are different from section 5.5.

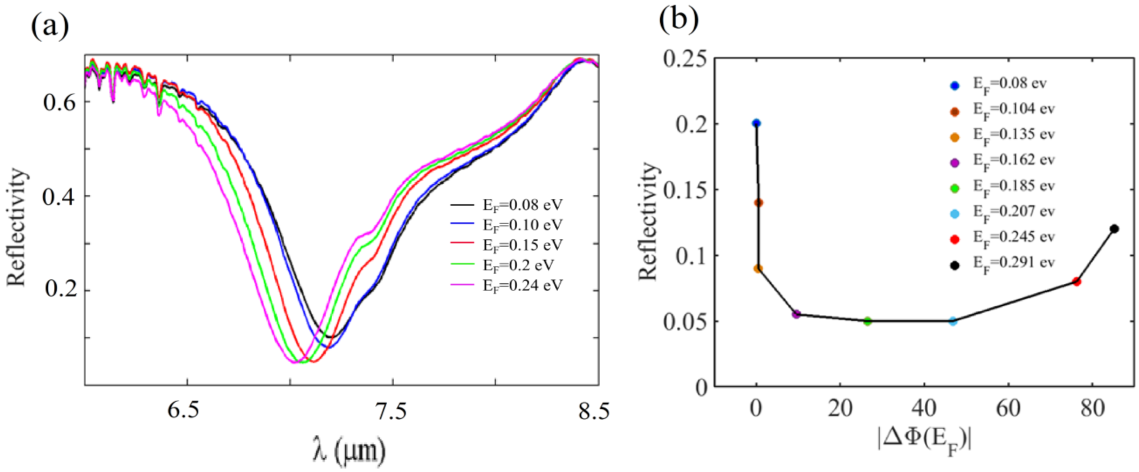

Figure 5.13: (a) The reflectivity of the metasurface design of Fig 5.3a measured by a FTIR. (b) The phase modulation and reflectivity as a function of Fermi energy at $\lambda = 7.57\,\mu m$

5.8 CONCLUSION

In summary, we have experimentally measured the gate voltage induced phase change of the reflected light from a graphene integrated metasurface. A phase change of almost 55° was recorded with a Fano-resonant metasurface design, of which about 28° occurred at nearly constant reflection amplitude. Numerical simulations performed matched closely with the measured phase response of the sample, further substantiating the experimental results. As a proof-of-concept application of this device, we employed it as a non-mechanical motion-sensing device and were able to measure submicron distances within 10% accuracy. Finally, we demonstrated that the anisotropic response of the metasurface coupled to the voltage dependent phase change allowed this device to be used as an ultra-thin active polarization converter. The results presented in this letter have significant implications for applications like active beam steering, phase conversion and motion sensing. However, the high insertion loss of R_{yy} (close to $\approx 10dB$ in our sample) and large applied bias voltages limit the efficiency of the studied design. These limitations can potentially be overcome by using alternative designs of the samples, thus enabling realization of practical high-efficiency devices in future.

Chapter 6: Enhancement of graphene photodetection using high-collection efficiency plasmonic metasurfaces

6.1 INTRODUCTION

As mentioned in the introduction chapter, graphene photodetectors can be wideband and potentially ultra-fast. The speed of photodetectors is generally limited by two factors. 1) Transit time of the generated electron-hole, which is the time it takes for the carrier to move from source to drain electrode 2) The RC time constant of the photo detection circuit. The holy grail of communication system is being able to modulate and detect the signal at a fast speed and therefore reduce both the transit time and the time constant of the photodetectors. A typical photodetector based on photoconductivity is shown in Fig. 6.1a where the blue and the yellow regions represent the photoconductor

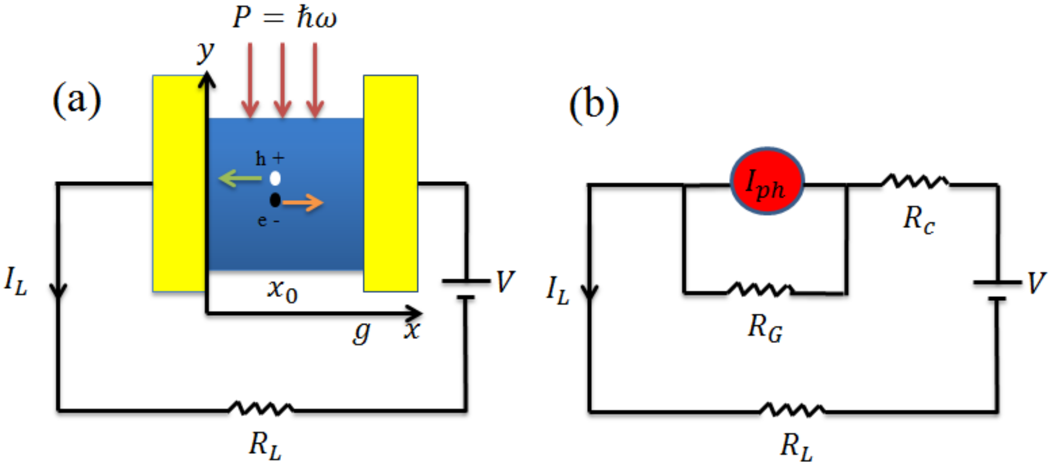

Figure 6.1: (a) A typical photodetector based on photoconductivity[71]. The blue and yellow region represent the photoconductor and contact. The electron-hole pair are generated in response to photons illuminated at the device. The load resistance, the bias voltage and the photocurrent are shown in the circuit. (b) The equivalent circuit model for the photodetector in (a). R_c and R_G are the metal-graphene contact resistance and graphene resistance.

And the metallic electrodes respectively. Fig 6.1b shows the circuit model for the photodetector circuit of Fig 6.1a where the graphene photoconductor is modeled with a current source I_{ph} and a parallel resistance R_G and a series resistance R_c is modeling the graphene-metal contact resistance. The transit time can be described as $\tau_{tr} = g/\upsilon_{tr}$ where g is the width of the photo-conducting region and υ_{tr} is the carrier drift velocity which is proportional to the carrier (electron or hole) mobility:

$$\upsilon_{tr_{e,h}} = \mu_{e,h} E. \qquad (6.1)$$

In eq. 6.1, $E = V_{bias}/g$ where V_{bias} is the bias voltage between the drain and source electrodes. Graphene introduces two interesting features as a photoconductor: i) large mobility which reduces the transit time. ii) Equal mobility for electron and hole $\mu_e = \mu_h$ unlike other semiconducting materials where hole mobility is much lower than that of electron. Thereby both electron and hole contribute equally to the current. From eq. 6.1, the transit time can be described as:

$$\tau_{tr} = g^2/(\mu V_{bias}) \qquad (6.2)$$

As a result of the quadratic relation between the size and the transit time, it is highly desirable to reduce the size of the photo-conducting region g to reduce the transit time. Ideally the transit time needs to be smaller than graphene recombination time which is 1∼3 picoseconds[122,123]. In order to further decrease τ_{tr} it is also possible to increase V_{bias}, however that is limited by breakdown field of the photoconductor material or substrate/superstrate between drain and source contacts. In what follows we use the procedure outlined in Ref (71) to estimate the photocurrent for the photodetector in Fig. 6.1 based on transit time and recombination time of photocarriers, assuming that the photoconductor is graphene.

Fig 6.1 shows an absorption event at $x = x_0$ which generates an electron-hole pair. The probability of the hole and electron reaching the electrodes is $e^{-(x_0/v_{tr}\tau_R)}$ and $e^{((g-x_0)/v_{tr}\tau_R)}$ respectively where τ_R is the photocarrier recombination lifetime. By integrating the contribution of all photons over the graphene surface photocurrent is obtained:

$$I_{ph} = \int_0^g e\Psi(x_0)(e^{-(\frac{x_0}{v_{tr}\tau_R})} + e^{-(\frac{g-x_0}{v_{tr}\tau_R})})dx_0 \qquad (6.3)$$

Assuming uniform illumination of monochromatic light on the graphene channel. In eq. (6.3), $\Psi(x_0)$ is the electron-hole generation rate per unit distance and is given by:

$$\Psi(x_0) = \frac{\beta P_{inc} M}{\hbar\omega g} \qquad (6.4)$$

where P_{inc} is the incident power, M is the hot carrier multiplication factor and β is the fraction of incident light absorbed in the graphene layer. The hot carrier multiplication factor M linearly scales with frequency and approaches unity in the mid-IR range[124]. Equation 6.3 reduces to:

$$I_{ph} = \frac{eP_{inc}}{\hbar\omega}\beta\frac{2M\tau_R}{\tau_{tr}}(1 - e^{-\frac{\tau_{tr}}{\tau_R}}) \qquad (6.5)$$

Photodetectors based on photo-conductivity are benchmarked by their photoconductive gain which is the number of detected photocarriers per absorbed photon: $G = (\frac{I_{ph}}{e})/(\frac{\beta P_{inc}}{\hbar\omega})$. From (6.5):

$$G = \frac{2M\tau_R}{\tau_{tr}}(1 - e^{-\frac{\tau_{tr}}{\tau_R}}) \qquad (6.6)$$

From Norton theorem, the parallel circuit model of graphene shown in 6.1b can be converted to a series circuit of $V_{ph} = R_G I_{Ph}$ as the source and R_G as resistance. Then I_L

can be calculated from the circuit element as: $I_L = I_{ph}R_G/(R_G + R_c + R_L)$ where R_G, R_c and R_L are the equivalent resistance for graphene, metal-graphene contact and the load for the photodetector of Fig 6.1a. The responsivity of the photodetector defined by $\mathfrak{R}_{ph} = I_L/P_{inc}$ and is given by:

$$\mathfrak{R}_{ph} = \frac{R_G}{R_G + R_c + R_L}\frac{e}{\hbar\omega}\beta G \tag{6.7}$$

If $\tau_{tr} \ll \tau_R$ the photo-carriers are collected very efficiently and the photoconductive gain G becomes close to its maximum value of 2. This can be directly calculated form eq 6.6. A photoconductive gain $G = 2$ means that for every photon that is absorbed in graphene, 2 photocarriers are detected (one electron and one hole). In addition to photocarriers that arrive at the electrodes by drift velocity, some photocarriers go through ballistic motion at the Fermi velocity of $V_F = 10^6\ \frac{m}{s}$ independent of the electric field across the electrodes. These are the carriers which are not affected by substrate impurities and graphene phonons and experience no backscattering. For a gap length of $g = 100\,nm$ and graphene mobility of $1000\ \mathrm{cm^2/Vs}$ and a bias-voltage $V_{bias} = 0.3\mathrm{V}$ (maximum voltage allowed before break-down in the air-gap), the transit time $\tau_{tr} = 0.33\,ps$ whereas the ballistic transport time $\tau_b = g/V_F = 0.01\,ps$ which are both smaller than the recombination time for single-layer graphene $\tau_R = 1\sim3$ picoseconds[122,123]. The hierarchy for the lifetime of these processes for the above-mentioned parameters can be summarized: $\tau_b << \tau_{tr} < \tau_R$ although τ_{tr} depends on gap size, graphene mobility and bias voltage and can be smaller or larger than τ_R accordingly. However the ballistic photocarriers travel in random directions and move toward the drain and source contact with the same probability and therefore do not contribute to the photocurrent. The

Equation 6.7 indicates that there are two major ways to improve the responsivity of a photodetector. 1) Increasing the graphene absorption (β) and 2) improving collection efficiency by reducing the transit time which increases the photoconductive gain (G). In this chapter, we design a metasurface that serves two purposes simultaneously, i) increase the absorption of light in graphene by enhancing the electromagnetic fields ii) reduce the size of photo-conducting region to improve collection efficiency. We first investigate the optical response of the metasurface and calculate graphene absorption from full-wave COMSOL simulation. The dark current is calculated using electrostatic COMSOL simulations. Finally the photocurrent and responsivity of the photodetector is estimated.

6.2 METASURFACE DESIGN AND ABSORPTION ANALYSIS

We used a metasurface similar to the double-fano resonance metasurface that was explained in depth in section 4.3 of chapter 4 with a slight difference that the center of dipole is connected to the wire of adjacent unit cell which provides drain and source electrodes for the purpose of collecting the photocarriers. The unit cell of the structure is shown in Fig. 6.2a. The simulation results for the reflectivity of this metasurface integrated with graphene ($\mathrm{E_F} = 0.08\ \mathrm{eV}$) is shown in Fig 6.2b which is similar to the response of the structure analyzed in section 4.3. The inset of Fig. 6.2b shows the charge distribution of the monopole and dipole mode. The line that connects the dipole to the wire is passing through the center of the dipole which has zero charge for both the monopole and dipole mode which explains why it does not change the optical response of the structure. The SEM picture for the fabricated metasurface on graphene in shown in Fig. 6.2c. The source lines extend beyond the metasurface on one side and connect to a large source contact (not shown in Fig. 6.2c) and similarly the drain lines connect on the other side to a large drain contact. The design provides a drain and source for each unit cell which is the main idea of this work: collect the electron-hole pair on each unit cell, reducing the size of the photo-conducting region to the gap (between monopole and dipole) of the metasurface which coincides with maximum concentration of photo-carriers. Figure 6.2d depicts the graphene ohmic loss across the spectrum, comparing the loss for inside and outside the gap. The ohmic loss surface density was calculated from:

$$\frac{dP_{loss}}{dS} = J.E = \sigma_r |E_t|^2 \qquad (6.8)$$

where E_t is the tangential electric field at the graphene plane. The blue curve is the ohmic loss in the gap and has a maximum close to the dipole mode at $\lambda \approx 7.4\mu m$ however it is vanishing close to the monopole mode at $\lambda \approx 6.3\mu m$. The red curve is the graphene loss outside the gap and has a maximum at the wavelength of monopole resonance. The insets of Fig 6.2d show the field enhancement $|E_t/E_{inc}|^2$of these two modes which confirm that the field enhancement (loss) outside the gap is mainly due to the monopole mode whereas the loss in the gap is primarily induced by the dipole mode. The total graphene loss is shown by the magenta curve and is around 40 % at $\lambda \approx 7.4\mu m$, however it should be noted that only the electron-hole pairs generated (due to absorption) inside the gap find the opportunity to be collected before recombination. In other word we can approximate the fraction of absorbed light $\beta = 0.2$.

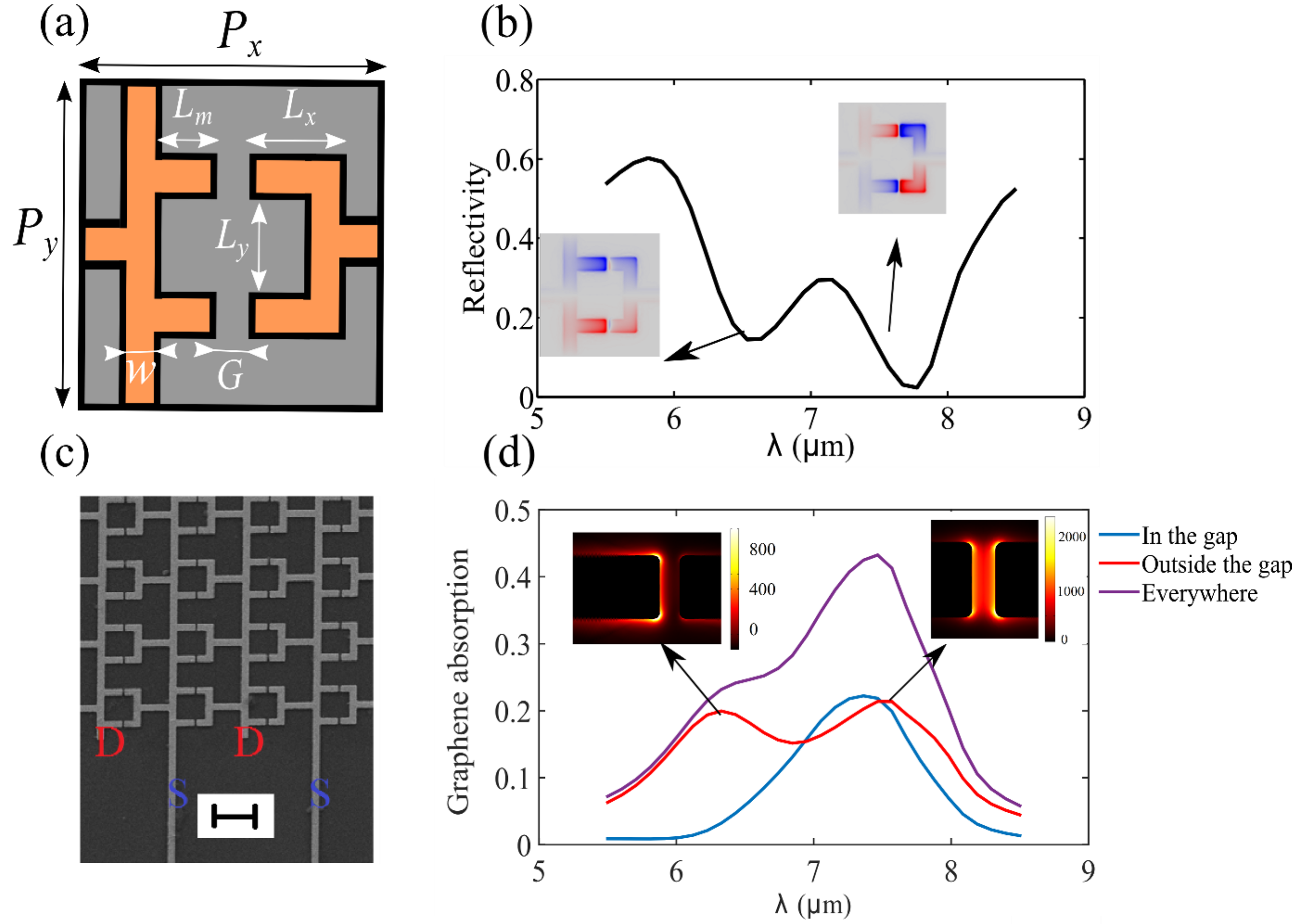

Figure 6.2: (a) Geometry of the unit-cell of the metasurface with parameters: $P_x = P_y = 3.3\mu m, L_x = .743\mu m, L_m = .825\mu m, L_y = 1.32\mu m,$ and $w = .33\mu m$ and $G = 100nm$. The length of the horizontal wire that connect the dipole to the vertical wire is 1.302 μm. (b) The simulation results for reflectivity of the metasurface at normal incidence of Y-light. The insets show the charge distribution of the monopole mode (left) and the dipole mode (right). (c) the SEM picture of the fabricated metasurface on graphene. The size of the scale bar is $2\mu m$. (d) Graphene absorption inside (blue) and outside (red) the gap. The magenta color shows graphene absorption on all areas. The insets represent the field enhancement $|E_t/E_{inc}|^2$ by the metasurface for the monopole (left) and dipole mode (right).

6.3 DARK CURRENT ESTIMATION

An electrostatic COMSOL model is employed to estimate the dark current. Figure 6.3a shows the potential on the graphene plane (right below the metasurface). A potential difference of $V_{bias} = 0.1\,\mathrm{V}$ is applied between the electrodes and the right electrode is grounded. We assume that addition of graphene under the metasurface does not change the electrostatic fields which is a good approximation since graphene is ultrathin and has a small conductivity compared to metal. The electrostatic fields are depicted in Fig 6.3b which is around 0.8 MV/m in the gap between the electrodes. The field lines in Fig 6.3c show the paths with equal electrostatic fields which correspond to the paths with equal current, since graphene has identical conductivity everywhere due to the back-gating scheme. The colors represent the potential and the density of the lines imply current density which is larger in the gap between the electrodes. The graphene surface current density is calculated from the electric field though: $K(x, y) = \sigma E(x, y)$ where σ is the conductivity of graphene. Graphene photodetectors are usually operated at the charge neutrality point. The absorption is maximum at this point since the interband transition is allowed for all electron energies smaller than photon`s energy $2E_F < \hbar\omega$. For all calculation in this chapter, we use the conductivity of graphene at the charge neutrality point. The DC conductivity of graphene at the charge neutrality point depends on the concentration of impurity, however it has been reported to be in the range: $4e^2/h < \sigma < 8e^2/h$ where h is the Planck constant and e is the electron charge. The conductivity is $8e^2/h$ for high quality samples and converges to $4e^2/h$ for bad quality samples[86]. We choose $\sigma = 8e^2/h \approx 2.2 \times 10^{-4}\ S$. In Fig. 6d the colors show the surface current density in units of Ampere per meter. Next a line is defined across the unit cell that passes through the gap to calculate the current flowing in different cross section of the unit cell and to estimate the total dark current. For clarity the line is shown in both Fig 6.3a and 6.3d. The total current across the line can be calculated as

$$I = \int \vec{K}.dl\hat{n} = \sigma \int \vec{E}.dl\hat{n} \qquad (6.9)$$

Where the surface current density $\vec{K}$ is integrated along the line and $\hat{n}$ is the unit vector normal to the line. The total dark current calculated from eq. 6.9 is equal to $I_{dark-cell} \approx 187\ \mu A$. Also in Fig 6.3d the percentage of the current that passes through each area is given with the gap current being the highest at 54 %. Also the total graphene resistance of the unit cell circuit can be calculated as $R_{G-cell} = V_{bias}/I_{dark-cell} \approx 534\ \Omega$. The unit cells are connected in parallel, thereby the total dark current of the photo-detector circuit is going to be $I_{dark-circuit} = I_{dark-cell} \times NM$ where N and M are the number of unit cells in the horizontal and vertical direction.

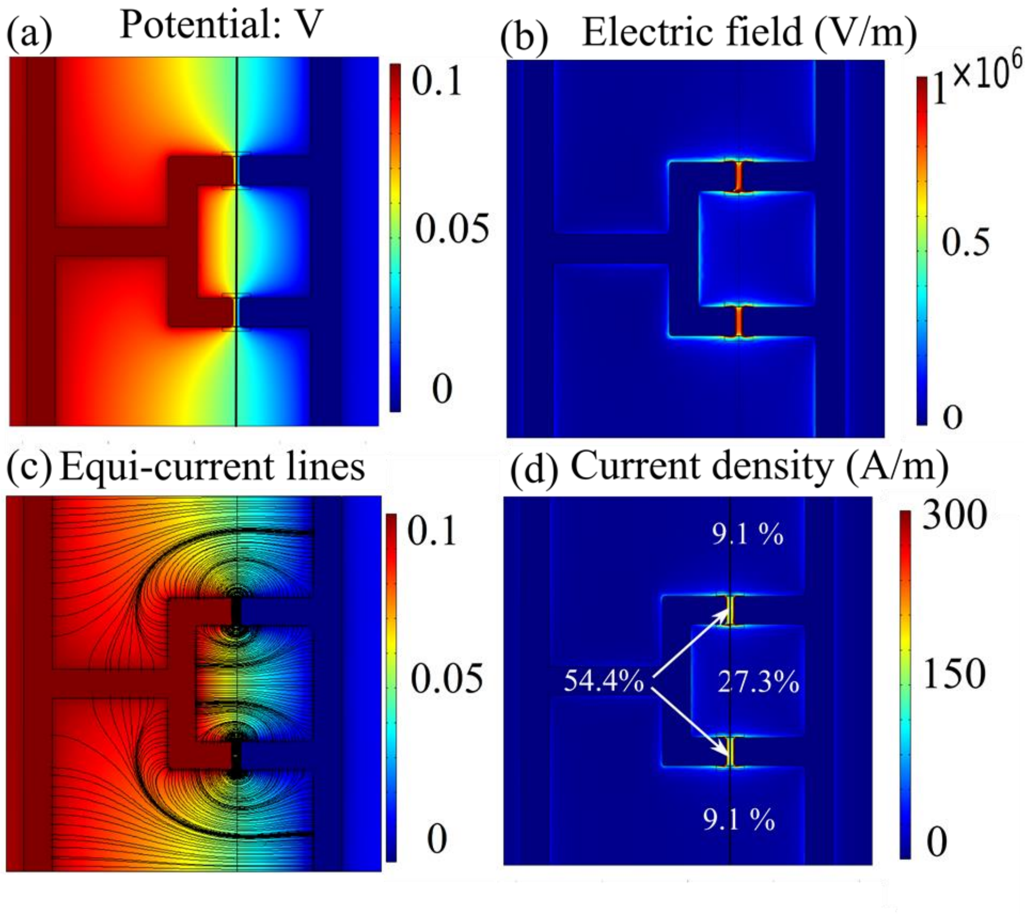

Figure 6.3: (a) The electrostatic potential across the structure. A bias voltage of 0.1 V is connected between the left and red right (ground) electrode. (b) Electric field in units of volts per meter. (c) The streamlines of equal electric field which corresponds to equal currents. (d) The surface current density in units of Ampere per meter. The numbers indicate what percentage of the total current flows through different areas of the metasurface.

6.4 RESPONSIVITY ENHANCEMENT USING PLASMONIC METASURFACE

To provide a reference for the photocurrent enhancement, we would like to compare the responsivity for two cases: 1) a bare graphene sheet between a drain and source with identical width (W) and length (L) and a load resistance of R_L. 2) a metasurface-based photodetector (MBPD) on top of a graphene sheet (Fig. 6.2c) with the same width and length of the previous case. Comparing the two numbers will quantify the photocurrent enhancement using the plasmonic metasurface.

6.4.1 Photocurrent generation for a reference graphene sheet

For both case 1 and 2, we choose $W = L = 33\mu m$, $R_L = 50\Omega$, recombination time of $\tau_R = 2\,ps$, mobility of $\mu = 1000\,\text{cm}^2/\text{Vs}$, $\sigma = 8e^2/h \approx 2.2 \times 10^{-4}$, for simplicity $R_c = 0$ and $V_{bias} = 0.1\text{V}$, at the incident wavelength of $\lambda = 7.5\mu m$. For case 1 of bare graphene from eq. 6.2 we find, $\tau_{tr} = 90ns$ which results in the photoconductive gain of $G \approx 5 \times 10^{-5}$. Graphene resistance is also calculated from $R_G = \frac{1}{\sigma}\frac{L}{W} \approx 4500\ \Omega$. The fraction of energy absorbed in bare graphene is known to 2.3% thereby $\beta = 0.023$. The responsivity can then be estimated from eq. 6.7 to be $\Re_{ph} = 5.5\mu\text{A/W}$.

6.4.2 Photocurrent generation for a MBPD

The goal in this section is to estimate the responsivity of the MBPD (shown in 6.2c) based on the equivalent circuit model in Fig. 6.1a,b and a circuit analysis. In Fig. 6.4 the circuit model of the photodetector is shown with each unit cell modeled with a circuit similar to 6.1b. It should be noted that R_G is Fig. 6.4 is the graphene resistance of a unit cell (R_{G-cell}) calculated in section 6.3 using electrostatic simulations. The circuit has N unit cell in X direction and M unit cell in Y direction and

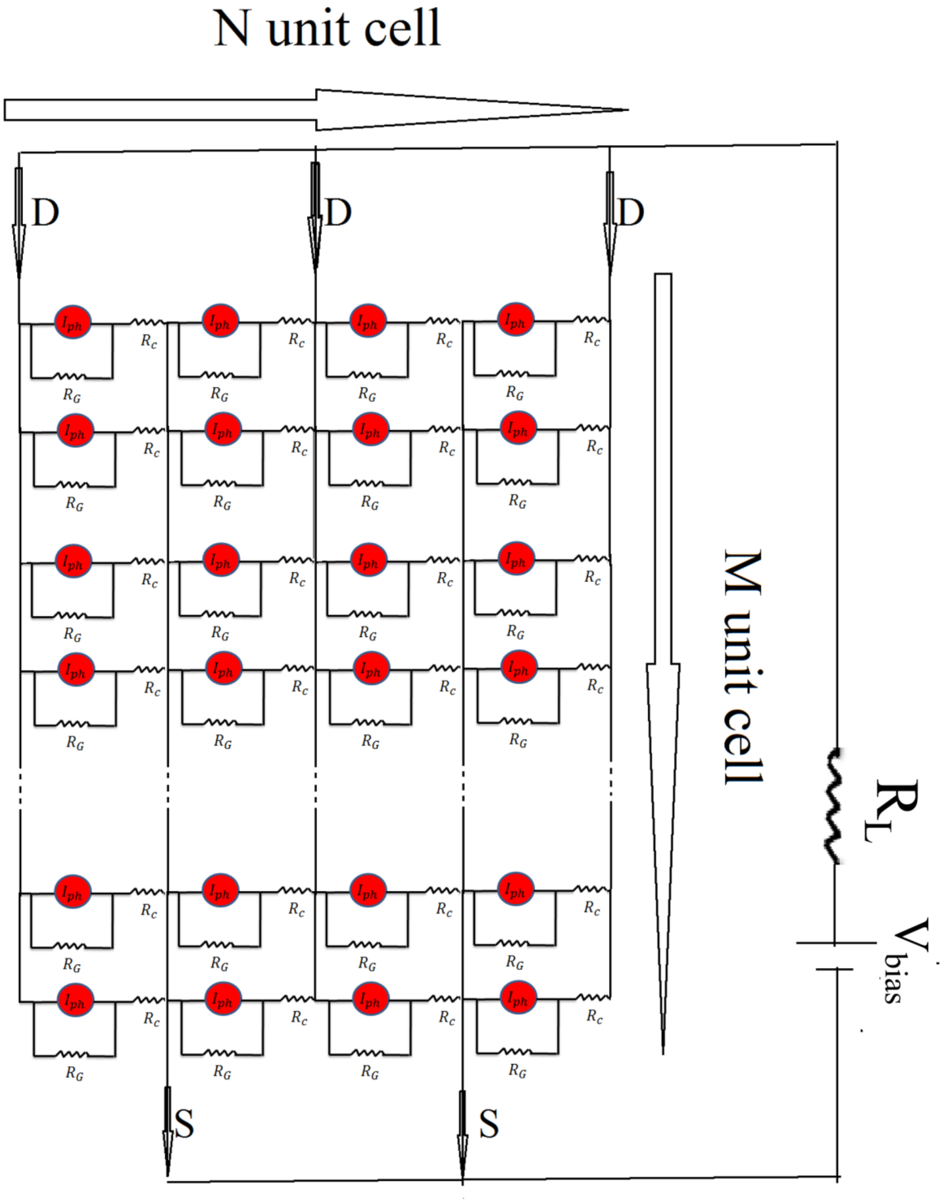

Figure 6.4: The electrical circuit model, corresponding to the MBPD each unit cell is modeled with a circuit shown in Fig. 6.1b. The drain and source lines and the direction of current flow is shown by the arrows. The load resistance and the DC bias complete the circuit.

is connected to a bias voltage and a load resistance where the direction of current flow is shown by arrows. From circuit theory, each unit cell (circuit of 6.1a) can be simplified to 6.5a. Therefore the photodetector circuit is comprised of $N \times M$ circuit of Fig 6.5a with parallel current source and resistance and can be reduced to the equivalent circuit of Fig 6.5b. The load current I_L is then given by:

$$I_L = \frac{I_{ph} R_G}{(R_G + R_c)/NM + R_L} \tag{6.10}$$

Equation 6.10 and the circuits of Fig. 6.5 indicate that the measureable photocurrent I_L depends on the ratio between R_G and R_L and the number of unit cells of the MBPD. Reducing the size of the metasurface as long as the collective response of the metasurface is preserved, can increase the load current for a given generated photocurrent of I_{ph}.

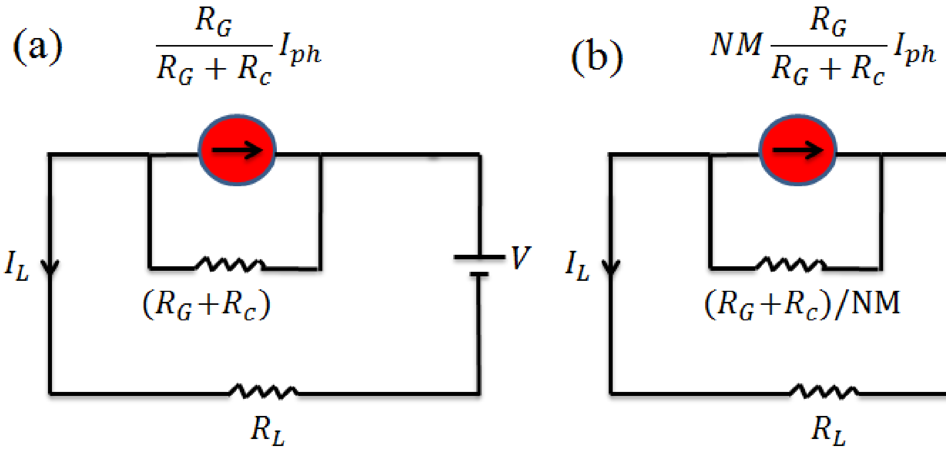

Figure 6.5: (a) The equivalent circuit for a metasurface unit cell with the equivalent graphene resistance of R_G and contact resistance of R_C. (b) The equivalent circuit for the MBPD (circuit of Fig 6.4) where N and M are the number of unit cells in X and Y direction.

Now we calculate photocurrent generated by each unit cell: I_{ph} of the circuit shown in Fig. 6.4. Having in mind that the incidence power in each unit cell $P_{inc-cell} = P_{inc}/NM$ where P_{inc} is the total incident power on the whole device area.

$$I_{ph} = \frac{P_{inc}}{NM}\frac{e}{\hbar\omega}G\beta \tag{6.11}$$

which leads to:

$$\begin{aligned} I_L &= \frac{R_G}{(R_G + R_c)/NM + R_L}\frac{P_{inc}}{NM}\frac{e}{\hbar\omega}G\beta \\ &= \frac{R_G}{(R_G + R_c) + NMR_L}P_{inc}\frac{e}{\hbar\omega}G\beta \end{aligned} \tag{6.12}$$

$$\Re_{ph-MBPD} = \frac{R_G}{(R_G + R_c) + NMR_L}\frac{e}{\hbar\omega}G\beta \tag{6.13}$$

which is the responsivity of the MBPD. From section 6.2, we know that $\beta = 0.2$. Since the periodicity of the metasurface is $P_x = P_y = 3.3\mu m$, we choose $N = M = 10$ so that the metasurface covers the whole area of the device ($W = L = 33\mu m$). N and M are large enough for our device to demonstrate collective (periodic) response. The graphene resistance for each unit cell $R_G = 534\ \Omega$ from our electrostatic calculations in section 6.3 and the gap size of the metasurface is 100nm, which gives $\tau_{tr} = 1\ ps$ and the photoconductive gain estimates as $G \approx 1.57$. This is a considerable improvement (almost 5 orders of magnitude) compared to case 1 with bare graphene ($G \approx 5 \times 10^{-5}$). The improvement is due to high collection efficiency of the metasurface design. From eq. 6.13 the responsivity can be estimated:

$$\Re_{ph-mbpd} \approx 0.17\text{A/W} \tag{6.14}$$

Therefore performance improvement is the ratio of the responsivity of the MBPD and bare-graphene which is about 31000. The drastic improvement is primarily due to high collection-efficiency of the metasurface. The secondary reason is that the graphene absorption of light is enhanced by the plasmonic metasurface. From section 6.3 , the dark current of the MBPD with $N = M = 10$ can be estimated as $I_{dark-circuit} = I_{dark-cell} \times NM \approx$ 19mA. For the laser power of $P_{inc} = 10mW$, the photocurrent of the MBPD is going to be $I_L \approx$ 1.7mA (assuming that the absorption is not saturated yet), which is roughly 10 times smaller than the dark current.

6.5 DETECTIVITY AND NOISE-EQUIVALENT POWER

The main design parameter for a photodetector is the sensitivity in detecting the optical signal of interest. The figure of merit of a detector that quantifies this sensitivity is defined as:

$$D^* = \frac{\sqrt{A*\Delta f}}{NEP} \tag{6.15}$$

Where A is the device area in $cm^2$and Δf is the signal bandwidth in Hertz and NEP is the noise-power equivalent which is the optical input power to the detector that produces a signal-to-noise ratio of unity (S/N=1). For the MBPD photodetector of this chapter, the signal bandwidth can be calculated from the time constant of the circuit τ_c as $\Delta f = 1/2\pi\tau_c$ where $\tau_c = R_c \times C_c$. Here R_c and C_c are the resistance and capacitance of the photodector circuit which easily relate to the unit cell values: $R_c = R_G/NM$ and $C_c = C_G NM$. From standard formula of capacitance, C_G of a unit cell can be approximated by: $C_G \approx 10^{-17}F$ by neglecting the effect of the oxide substrate. The circuit time-constant can be simplified to $\tau_c = R_G C_G \approx 5 \times 10^{-14}s$ from which the signal bandwidth $\Delta f = 3.2 \times 10^{12}\ Hz$.

To calculate the noise-equivalent power, we need to determine how much input signal power would result in a photocurrent equal to the dark current (for a given bias voltage). From pervious calculations, the dark current is around 19 mA for $V_{bias} = 0.1$V and the responsivity is around $0.17\ A/W$. This requires 110 mW of input power to achieve 19 mA of photocurrent, in other words $NEP = 110\ mW$.

The total area of MBPD is $A = 10^{-7} cm^2$, the figure of merit or detectivity of the MBPD is then calculated from eq. 6.15 to be $D^* \approx 5 \times 10^4 \frac{cm.Hz^{1/2}}{watt}$. It should be noted that this value is much lower than conventional mid-IR photodetectors. As an example detectivity of GeHg (a bandgap material) is around $10^{10} \frac{cm.Hz^{1/2}}{watt}$ at the temperature of 28 kelvin although the time constant is only tens of nanoseconds which is much slower than the MBPD of about 50 fs. Another point is that graphene mobility is high even at room-temperature which is an advantage compared to bandgap materials which require cooling to low temperatures.

From this comparison, one can conclude that graphene photodetectors are mostly useful for high-speed (large bandwidth) detection of signal however the sensitivity is much lower than the traditional bandgap materials.

6.6 PERFORMANCE EVALUATION

In this section, we compare the performance of the MBPD introduced in this chapter to other similar works. To our knowledge, the only MBPD published is Ref [71] where a plasmonic metasurface with a simple dipole antenna array was fabricated on CVD graphene between large drain and source contacts. The MBPD of this chapter employs a Fano resonance which has larger quality factor and therefore larger field enhancement than a dipole resonance used in Ref [71]. In fact, our MBPD can absorb 20 % ($\beta = 0.2$) of the incident light energy which is twice the absorption reported in [71].

The dark current in the mentioned work can be estimated from the transport measurement to be $I_{dark-circuit} = \frac{V_{bias}}{R_{DS-CNP}} = 5mA$ where R_{DS-CNP} is the resistance between the drain and source contact at the CNP point. This dark current is almost 4 times smaller than the dark current of our photodetector $(19mA)$. The reason can be explained by larger resistance of the antenna array where the antennas are oriented in series between the contacts whereas in our MBPD, all the unit cells are connected in parallel and therefore the circuit resistance is lower. For equal gap size and graphene mobility, the photoconductive gain should be equal. Also if R_G and C_G are the resistance and the capacitance of each unit cell (nano-detector) the RC time response for both MBPDs will be identical to $R_G C_G$ (neglecting the parasite capacitances). On another note, the bias voltage required for collection in our MBPD $(V_{bias} = 0.1V)$ is much smaller than Ref [71] $(V_{bias} = 5V)$ leading to much lower power consumption which is an advantage e.g. in wearable technologies.

In an interesting work, it was shown that two graphene transistor, spaced by 5 nanometers can produce relatively large responsivity of 1 A/W[74]. The top graphene transistor absorbs light and the photocarriers can tunnel through the short barrier. The tunneled carriers change the doping of the graphene in the lower transistor and shift the I-V curve of the lower transistor inducing a large change in current. The top transistor and the incident photons therefore are acting as gate contact for the lower transistor and the entire arrangement functions as a phototransistor. The detector is wide-band as graphene has no band-gap. Wide-band detection is an interesting feature of graphene photo-detectors. On the other side however the measured photocurrent does not give any information about the energy of the incident photon. In that regard, one can envision an array of MBPD with large quality factor (narrow-band) that can potentially reproduce the spectral information of the incident light similar to a spectrometer. This distinguishes our work from the photo-transistor of Ref[74].

6.7 CONCLUSION

We designed a Fano-metasurface with high-collection efficiency and large field enhancement. The electrical connectivity of metasurface provides a drain and source electrode for every single unit cell of the metasurface which reduces the transit time and improves the collection efficiency dramatically. Using full-wave simulations, the graphene absorption in the gap was calculated. The equivalent graphene resistance and the dark current was determined from an electrostatic simulations. A circuit analysis provided the mathematical relation for the responsivity of the MBPD. The devices demonstrates 31000 times responsivity improvement compared to a similar graphene photodetector without a metasurface. The sensivity of the MBPD was calculated and compared to band-gap materials.

Chapter 7: Material Characterization and Substrate Effect

7.1 INTRODUCTION

Plasmonic metasurfaces interact with the substrates, superstrates and 2D materials that they are integrated with. In chapter 4, 5 and 6 the interaction of plasmonic metasurfaces with graphene was utilized for realization of amplitude and phase modulators and high-speed sensors such as motion sensors and photodetectors. Therefore, it is important to characterize graphene and also study the interaction of metasurface resonances with the phonon resonance of SiO_2 which is the conventional isolating spacer in silicon samples. In this chapter, we employ coupled mode theory to analyze the optical response of the metasurface for two different purposes 1) derive the scattering time of charge carriers in graphene which is an important graphene parameter and 2) study the interaction of metasurface resonance modes with SiO_2 phonon resonance. The derived scattering time is in agreement with the scattering time derived from electrical transport measurement.

7.2 All optical measurement of carrier scattering rate

In this section we use a perturbative approach[57] to derive scattering rate of graphene charges. If a metamolecule made of PEC is perturbed by a mantle of surface area S and thickness $t \ll \lambda_R$ where λ_R is the resonant frequency of the metamolecule, the resonant frequency shift can be described by[57]:

$$\frac{\Delta\omega}{\omega} = \frac{t \int_S (1-\varepsilon_{||})\left|E_{||}\right|^2 dS}{W_0} - \frac{t \int_S (1-\frac{1}{\varepsilon_{\perp}})|D_{\perp}|^2 dS}{W_0} \tag{7.1}$$

Where $\varepsilon_{||}$ and $\varepsilon_{\perp}$ are the components of permittivity parallel and normal with respect to mantle surface and $W_0 = 2\int_V |E|^2 dV$ is the stored electromagnetic energy of the bare metamolecule. By observing that for graphene $t\left(\varepsilon_{||} - 1\right) = (i\sigma/\omega)$, eq 7.1 will be simplified to eq 4.2. Below we demonstrate that spectral shifts and linewidth changes produced from loading plasmonic metasurfaces with gated graphene can be used for precise determination of graphene's optical properties. Specifically, the free carrier scattering rate τ can be determined using a simple procedure that utilizes complex-valued resonant frequencies

$$\tilde{\omega}_{m(d)}^{n} = \omega_{m(d)} - i/\tau_{m(d)} + \Delta\tilde{\omega}_{m(d)}^{n} \tag{7.2}$$

that are experimentally measured for a broad range of carrier' densities $n_0 < n < 4.8e12cm^{-2}$. The corresponding resonant wavelengths and quality factors are plotted in Fig. 4.5. According to eq 4.2, $\Delta\tilde{\omega}_{m(d)}^{n}$ satisfies[57] the following equation:

$$\frac{\Re e[\Delta\tilde{\omega}_{m(d)}^{n}]}{\Im m[\Delta\tilde{\omega}_{m(d)}^{n}]} = -\frac{\sigma_{im}(\omega_{m(d)}^{n}, n)}{\sigma_{re}(\omega_{m(d)}^{n}, n)}, \tag{7.3}$$

where graphene's conductivity is calculated at the resonant frequency $\omega_{m(d)}^{n} \equiv \Re e[\tilde{\omega}_{m(d)}^{n}]$.

Equation 7.3 expresses a novel opportunity for characterizing optical properties of graphene (rhs of the equation) using experimentally measured frequency shifts of metasurface resonances (lhs of the equation). This approach is particularly valuable in the mid-IR portion of the spectrum where traditional transmission/absorption spectroscopy of graphene[41,57] is challenging because $\sigma_{re}$of the SLG is much smaller than the universal conductance $\sigma_0 = e^2/4\hbar$ as shown in Figures 4.3b,c. Under such circumstances, very small ($< 1\%$) changes in transmission through graphene must be accurately measured in order to extract graphene's optical parameters such as, for example, its carrier scattering rate τ.

Since the metasurface is fabricated on top of the graphene, we do not have access to the parameters of the fabricated bare-metasurface. Therefore, we use COMSOL simulations followed by the least-square fitting procedure detailed in 4.9.1 to derive ω_d. It should be noted that simulation underestimates the metallic losses, therefore the lifetime τ_d of the bare metasurface is defined as a fitting parameters. we now can calculate $\Delta\widetilde{\omega}_d^n$ for a wide range of hole densities $1.5e12cm^{-2} < n < 4.8e12cm^{-2}$ for the dipole resonance using eq 7.2. The calculation of the scattering time τ was done using a two-parameter best-fit procedure. The fitting parameters are τ and the lifetime of the bare metasurface τ_d. The lhs of eq 7.3 was expressed as a τ_d-dependent quantity $E(n;\tau_d)$. Next, the rhs of eq 7.3 was expressed as a τ-dependent quantity $T(n;\tau)$. Graphene conductivities that need to be inserted into the rhs of eq 7.3 were calculated from eq 2.4. The best-fit pair (τ, τ_d) was determined by minimizing $\sum_n Diff$ in MATLAB where the difference function $Diff$ is defined as:

$$Diff(n;\tau,\tau_d) = [E(n;\tau_d) - T(n;\tau)]^2. \qquad (7.3)$$

The density range was chosen to ensure that Drude conductivity contribution $\sigma_{intra}(\omega)$ dominates over the interband conductivity contribution $\sigma_{intra}(\omega)$. The dipole resonance was chosen over the monopole resonance because according to Figures 4.2 c,d the effect of graphene on the former is much larger than on the latter. The experimentally obtained quantity $-\Re e[\Delta\widetilde{\omega}_d^n]/\Im m[\Delta\widetilde{\omega}_d^n]$ was plotted in Figure 7.1 alongside with the material quantity $\sigma_{im}(\omega_d, n)/\sigma_{re}(\omega_d, n)$ calculated for three values of hole scattering

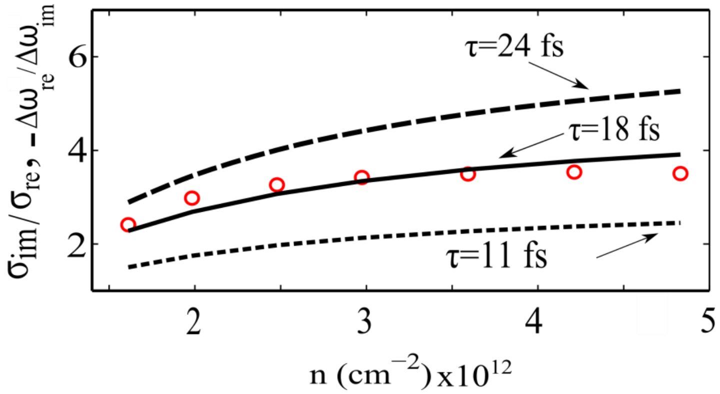

Figure 7.1: Extraction of the holes' scattering time τ in the Drude-dominated regime. Lines: $\sigma_{im}^{n}/\sigma_{re}^{n}$ calculated for three values of free carrier scattering time τ, circles: ratio of graphene-induced frequency shifts -$\Re e\left[\Delta\widetilde{\omega}_{m(d)}^{n}\right]/\Im m\left[\Delta\widetilde{\omega}_{m(d)}^{n}\right]$ of the resonances for a range of carrier concentrations.

time: $\tau_1 = 11$fs, $\tau_2 = 18$fs, and $\tau_3 = 24$fs. According to eq 7.1, these two quantities must be equal under the assumption that τ does not depend on the density of free carriers. It follows from Fig. 7.1 that this equality is rather accurately satisfied only for τ_2. Therefore, our experimental results impose very restrictive limits on the value of τ. We note that $\tau^{(DC)} \approx 14$fs, obtained using dc conductivity measurements, is indeed an under-estimate of the actual scattering time. As argued above, this may be related to the presence of grain boundaries outside of the optical field concentration areas of the metasurface.

7.3 EFFECT OF THE SiO$_2$ SPACER ON THE QUALITY FACTOR OF THE PLASMONIC MODE

Plasmonic metasurfaces mentioned in this dissertation, were fabricated on a silicon dioxide spacer of a Si/SiO$_2$ substrate. Silicon dioxide has a strong polaritonic resonance[113] at $\lambda_{SiO_2} \approx 9\mu m$. Fig. 7.2a displays the numerically simulated reflectivity of different components of the structure without the material resonance for the non-dispersive spacer with the refractive index $n_{sp} = 1.3$. The quality factors of the monopolar and dipolar resonances are obtained by fitting the numerically calculated reflectivity to eq 4.1. The comparison of the quality factors of the two resonances is presented in Table 7.2 for non-dispersive and dispersive SiO_2 spacers. While the quality factor of the monopolar resonance is only slightly affected by the polaritonic resonance in SiO_2, that of the dipolar resonance is two times higher for the metasurface on the dispersive SiO_2 substrate with complex-valued dielectric permittivity $\epsilon_{SiO_2}(\omega) \equiv \epsilon_{re}(\omega) + i\epsilon_{im}(\omega)$ plotted in Fig. 7.2d.

Spacer property	monopole	dipole
Dispersive spacer (SiO_2)	19	20
Non-dispersive spacer ($n_{sp} = 1.3$)	18	10

Table 7.1: The quality factor of the two resonances of a metasurface (defined in Figure 4.2a) fabricated over (second row) a dispersive SiO_2 spacer with the complex-valued dielectric permittivity $\epsilon \equiv \epsilon_{re} + i\epsilon_{im}$ plotted in Fig. 7.2d, and (third row) idealized non-dispersive spacer with refractive index $n_{sp} = 1.3$.

To investigate the effect of proximity between the dipole/monopole modes and the phonon-polariton resonance on the quality factor of the said modes, we have intentionally brought the frequency of the dipole mode closer to the polariton resonance. This was accomplished by up-scaling all the dimensions of the metasurface in the xy plane in order to red-shift the frequency of the dipole resonance. The colors in Fig. 7.2b depict the reflectivity for different periodicities. As the periodicity increases from $2.4\mu m\ to\ 3.9\mu m$ ($\approx 60\%$), the wavelengths of the monopole/dipole resonances, as well as the related wavelengths of the EIT1 and EIT2 dips, change by 36% and 18 %, respectively. The quality factors of the two resonances were extracted by fitting the reflectivities for each period to tri-Lorentzian profiles given by eq 4.1. The results of this extraction shown in Fig. 4.7c indicate that the quality factor of the monopole resonance increases from $Q = 15.5$ to $Q = 23.7$ (152% increase), whereas the quality factor of the dipole resonance changes from $Q = 12.5$ to $Q = 47.0$ (376% increase). The reason for this dramatic increase can be explained as being due to the increase of the electromagnetic energy stored in the dispersive medium, i.e. in the SiO_2 substrate underneath the plasmonic antenna. Recall that the electric energy stored in any dispersive medium with frequency-dependent complex-valued dielectric permittivity of $\epsilon(\omega) \equiv \epsilon_{re}(\omega) + i\epsilon_{im}(\omega)$ depends on the time-averaged electric field[2] $\boldsymbol{E}$ according to the following expression:

$$U_{E=}\frac{1}{2}\frac{\partial[\omega\varepsilon_{re}(\omega)]}{\partial\omega}\boldsymbol{E}^2 = \frac{1}{2}\left(\frac{\partial\varepsilon_{re}}{\partial\omega}\omega + \varepsilon_{re}\right)\boldsymbol{E}^2 \tag{7.4}$$

The multiplier factor $\epsilon_{eff} \equiv \partial[\omega\varepsilon_{re}(\omega)\,]/\partial\omega$ that enters eq 7.4 is equal to ε_{re} for a non-dispersive material. However it could be a rather large number for a dispersive material in the proximity of a phonon-polariton resonance. As the stored electric energy of a resonator increases, it`s quality factor Q increases. This comes from the definition of quality factor which is the ratio between the store energy and the dissipated energy. In Fig. 7.2d, the black and the blue curves show $\varepsilon_{re}(\omega)$ and $\epsilon_{im}(\omega)$ of SiO_2 [125]. The red circles depict $\partial[\omega\varepsilon_{re}(\omega)]/\partial\omega$ which grows from ≈ 2 at shorter wavelengths to ≈ 14 at $\lambda = 7.8\mu m$ close to the phonon resonance. Even more importantly for this work, the value of ϵ_{eff} can significantly exceed that of ϵ_{re} even for those frequencies for which $\epsilon_{im} \ll \epsilon_{re}$ is satisfied. That means that the dispersion can become significant before the

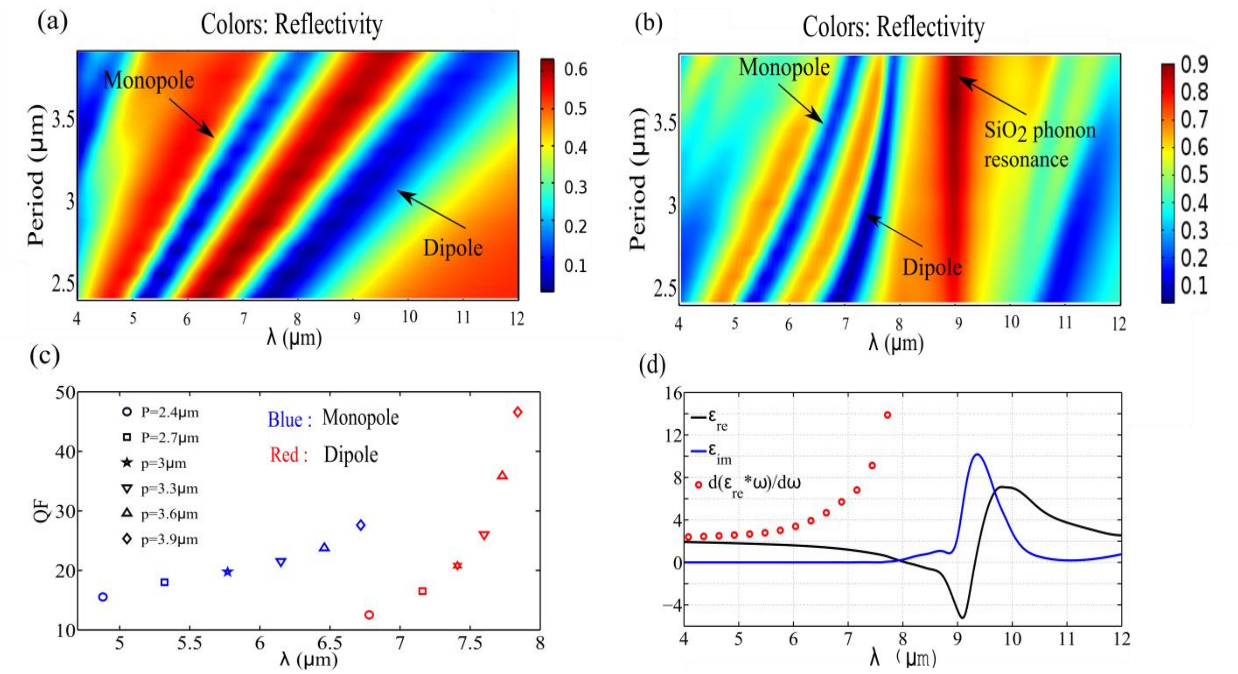

Figure 7.2: The normal incidence reflectivity from bare (no graphene) plasmonic metasurface shown in Fig 4.2 fabricated on top of (a) idealized non-dispersive spacer with refractive index $n_{sp} = 1.3$ and (b) dispersive SiO2 spacer with complex dielectric permittivity $\epsilon \equiv \epsilon_{re} + i\epsilon_{im}$plotted in (d) as a function of the wavelength λ. Vertical axis: periodicity P with which all in-plane dimensions are scaled with respect to the baseline dimensions given in caption to table 7.1. The thickness of the spacer ($t = 1\mu m$) and of the metasurface ($t_m = 30nm$) are kept fixed for all values of P. (c) The quality factors of both modes versus resonance wavelength for different periodicities. (d) The real and imaginary parts of the SiO2 permittivity. The red dots represent $\partial[\varepsilon_{re}(\omega)\ \omega]/\partial\omega$.

advent of high losses that would reduce the quality factor of the dipole resonance. For example, at $\lambda = 7\mu m$ we find that $\epsilon_{eff} \approx 6$ while $\epsilon_{re} \approx 1.14$ and $\epsilon_{re}/\epsilon_{im} \approx 50$. The increase in ϵ_{eff} increases the radiative quality factor of the dipole resonance because the quality factor is proportional to the stored energy which, in turn, is proportional to $\epsilon_{\ eff}$. This increase in the stored energy as the frequency of the dipole resonance approaches the polaritonic resonance of SiO_2 explains the dramatic increase of the quality factor of the dipole mode plotted in Figure 7.2.

7.4 CONCLUSIONS

In summary, it was shown that the graphene-induced optical detuning of plasmonic metasurface analyzed by the coupled mode theory provides a method for deriving the carrier scattering rate of graphene. The result is in agreement with that obtained from electrical transport measurement. Also it was shown that the proximity of the metasurface resonance with the phonon resonance of SiO_2 increases the energy restored in the substrate which increases the quality factor of the mode.

Chapter 8: Numerical Simulation of Graphene-Integrated Plasmonic Metasurfaces

8.1 INTRODUCTION

This chapter is an overview of the numerical simulation technique used in this dissertation. The simulation domain and boundary condition setting are introduced and the equations that derive the reflection coefficient from full-wave simulations are described. The numerical simulation results are compared to their experimental counterparts.

8.2 NUMERICAL ANALYSIS TECHNIQUE

For all the simulations in this dissertation, COMSOL MULTIPHYSICS a commercial software based on finite-element method was used. In Figure 8.1 the simulation domain and the material properties are shown. The two domain at either ends (left and right ends) represent perfectly matched layers (PML) which by definition does not reflect light at its boundary. The boundaries at the most right and left end are Perfect electric conductor (PEC). All other outside boundaries have periodic boundary condition.

The incidence wave is a plane wave which is modeled by a surface current as shown in Figure 8.1a. The surface current is defined by $\vec{J}(x,y) = \hat{m}\,.\exp\Big(j\big(k_x x + k_y x\big)\Big)$ where k_x and k_y are x and y components of the propagation vector and m is equal to x or y for the incident polarization of x and y.

Material properties are set for all domains, for gold and silicon dioxide the Palik handbook of optical properties was used[125]. The reflectivity can be derived from reflection coefficient r as: $R = |r^2|$. To calculate reflection coefficient r, we define two planes in the far-field at two z-coordinates distanced by Δ as shown in Fig 8.1b. The

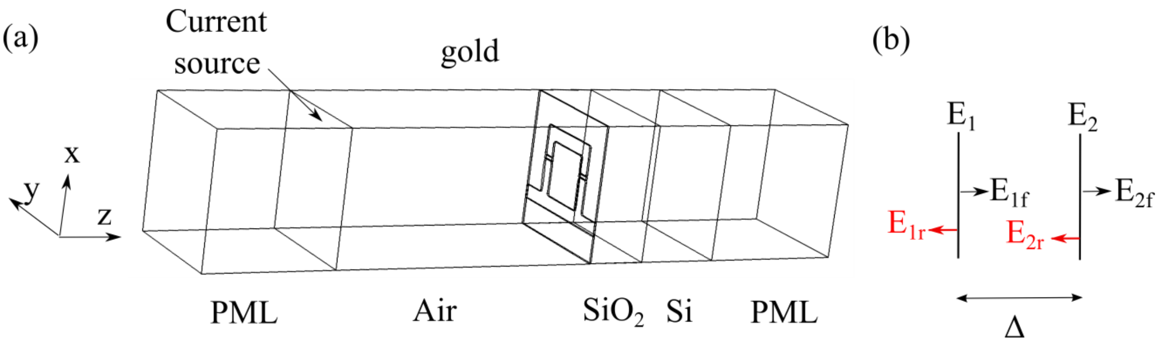

Figure 8.1: (a) The simulation domain. Different regions are tagged with their material name (b) The two reference planes in the air region used to define the reflection coefficient.

plane should be far enough from the sample to avoid near fields. The simulation results can provide the total electric field $E_1$and E_2 at these two z-coordinates which can be described in terms of forward and backward waves as:

$$\begin{aligned}\mathbf{E_1} &= \mathbf{E_{1r}} + \mathbf{E_{1f}} \\ &= (r+1)\mathbf{E_{1f}}\end{aligned} \tag{8.1}$$

$$\begin{aligned}\mathbf{E_2} &= \mathbf{E_{2r}} + \mathbf{E_{2f}} \\ &= \mathbf{E_{1r}} e^{-ik_0\Delta} + \mathbf{E_{1f}} e^{ik_0\Delta} \\ &= (re^{-ik_0\Delta} + e^{ik_0\Delta})\mathbf{E_{1f}}\end{aligned} \tag{8.2}$$

From equations 8.1 and 8.2, one can solve for the reflection coefficient r for known values of E_1, E_2, k_0 and Δ. In the simulations, Δ was chosen to be Δ= $0.05z_1$ where z_1 is the z-coordinate of the first plane. The above-mentioned procedure and the associated Matlab script that was used in this dissertation was developed by Dr. Hossein Mousavi.

8.3 NUMERICAL SIMULATIONS AND PROSPECTS FOR INDEPENDENT AMPLITUDE/PHASE MODULATION

Numerical simulations were carried out in order to verify the experimental results presented in Figure 4.4. In addition, these numerical simulations enable us to make predictions about some of the physical quantities that were not experimentally measured in this work, such as the amplitude and phase of the transmitted waves. The SLG was modeled using a surface current [57] $J_{SLG} = \sigma_{SLG} E_t$ where E_t is the tangential electric field on the graphene plane and σ_{SLG} is the optical conductivity of single-layer graphene described by eq. 2.4.

Figures 8.2a,b show the simulated reflectivity amplitudes $R(\lambda) \equiv |r(\lambda)|^2$ and phases $\varphi_R(\lambda) = \angle r(\lambda)$ of the reflected light for different carrier concentrations, and figure 8.2a is in excellent quantitative agreement with the experimentally measured spectra shown in Figure 8.2c. For completeness, we also present in Figures 8.3a,b the numerically simulated transmittances $T(\lambda)$ and phases $\varphi_T(\lambda)$ of the transmitted light although no experimental measurements of the transmission were performed. All simulations are performed for sample 1 with the gap size of 70nm. The incidence light is chosen to be P-polarized with the angle of incidence $\theta_i = 25°$ for consistency with our experimental setup that utilizes a high-NA microscope.

Below we use the results of the numerical simulations to demonstrate the promise of graphene-functionalized Fano-resonant metasurfaces for developing rapidly tunable amplitude and phase modulators (AM and PM) that can potentially operate with nanosecond-scale modulation speeds. We demonstrate that nearly pure phase modulation can be achieved at certain wavelengths (shown by red arrows in Figures 8.2a,b for reflected light and Figures 8.3a,b for transmitted light). For some other wavelengths (shown by black arrows in Figures 8.2a,b for reflected light and Figures 8.3a,b for

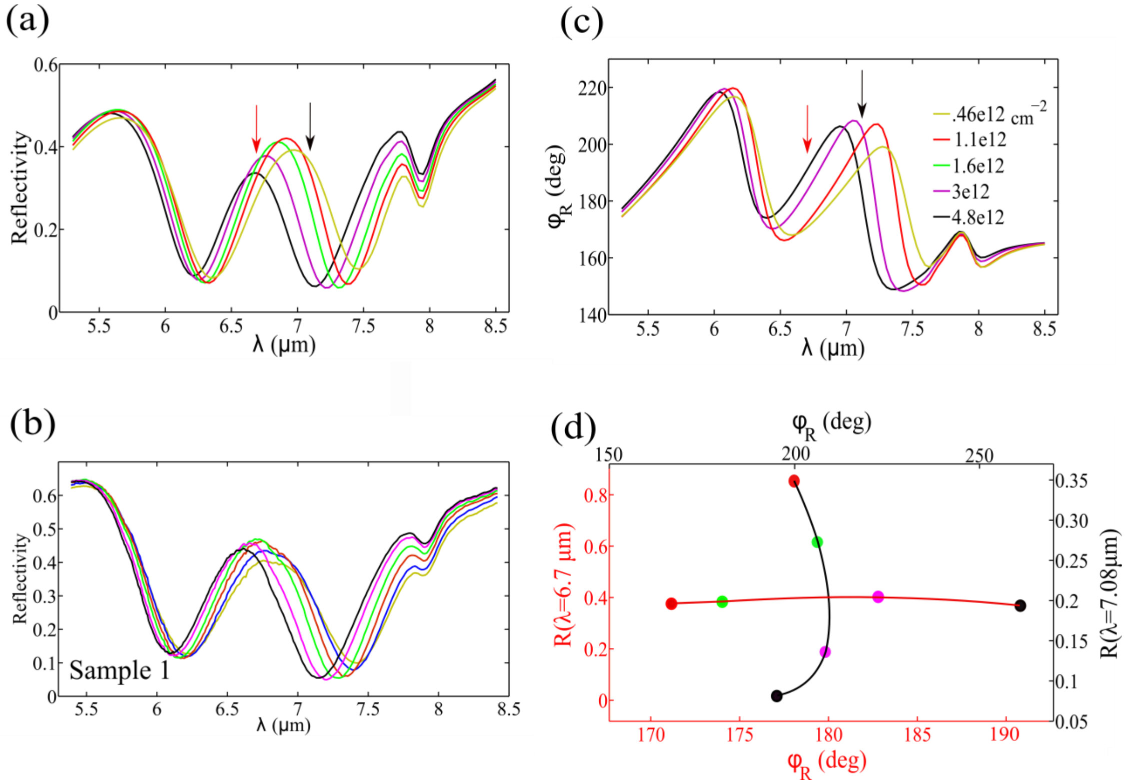

Figure 8.2: Reflectivity of sample 1 with parameters given in Fig 4.2 ($G = 70nm$) from numerical simulations **(a)** and FTIR measurements **(b).** The simulated results for phase of the transmitted light at different graphene doping levels **(c)**. The arrows indicate the spectral positions with constant scattering intensities (red arrows) and phase (black arrows). The simulated reflectivity-phase plane as function of carrier concentration at two different wavelength. **(d)** The red axes corresponds to the wavelength shown with the red arrow ($\lambda_R^{PM} = 6.7\ \mu m$) and similiarly black axes corresponds to black arrows ($\lambda_R^{AM} = 7.08\ \mu m$). The color of the circles correspond to the dopings presented in (c).

transmitted light) nearly pure amplitude modulation occurs as the carrier concentration changes. Specifically, in Figure 8.2d we plot the reflection data for four values of carrier density varying between $n = 1.6e12$ and $n = 4.8e12\ cm^{-2}$ (color-coded circle symbols) for two specific wavelengths ($\lambda_R^{PM} = 6.7\mu m$ and $\lambda_R^{AM} = 7.08\mu m$) in the (ϕ_R, R) phase plane. We observe that, for a fixed wavelength $\lambda = \lambda_R^{PM}$, the reflection phase $\varphi_R(\lambda_R^{PM})$ varies by almost $\Delta\varphi_R \approx 20°$ degrees as the function of n while the reflection amplitude $R(\lambda_R^{PM})$ changes by only 3% for the same variation of carrier density. The implication of this result is that one can develop a narrow-band PM which only affects the phase but not the amplitude of the reflected light. For example, if different elements of the metasurface can be independently controlled, one can envision an active beam steering reflect-array that is based on SLG-functionalized metasurface. Similarly, a narrow-band AM that affects the amplitude but not the phase of the reflected light can be

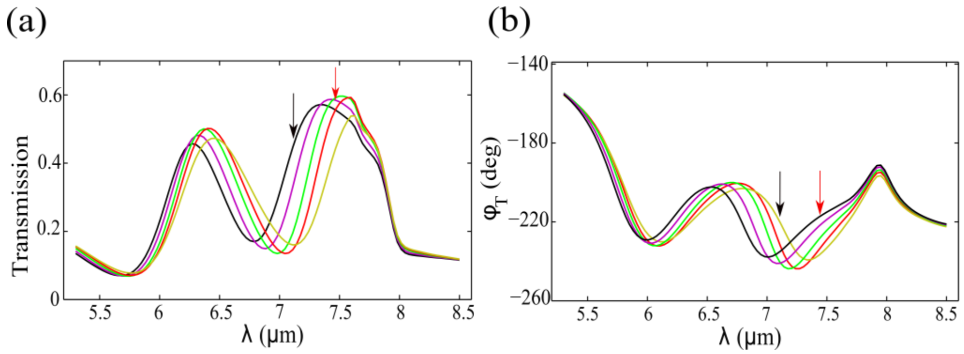

Figure 8.3: Tranmission spectrum of different doping levels from numerical simulations. Intensity **(a)** and the phase **(b)**. The color coding corresponds to the legend in Fig 8.2c.

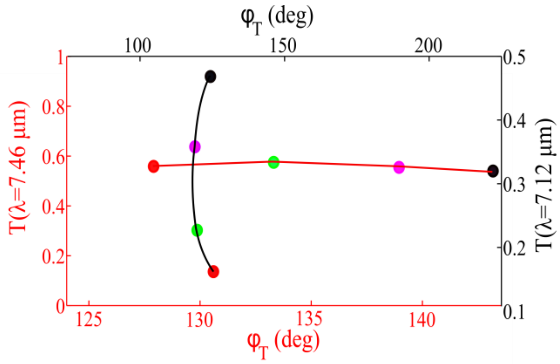

Figure 8.4: Transmission-phase plane for different graphene carrier concentrations at $\lambda_T^{PM} = 7.46\,\mu m$ (red curves/axes) and $\lambda_T^{AM} = 7.12\,\mu m$ (black curves/axes). These wavelengths correspond to the position of the arrows in Fig. 8.3. Graphene doping levels are color-coded according to the legend in Fig 8.2c.

implemented at $\lambda = \lambda_R^{AM}$: according to Figure 8.2d, the reflectance $R(\lambda_R^{AM})$ varies by factor 5 (from $R = 0.07$ to $R = 0.35$) whereas the phase $\phi_R(\lambda_R^{AM})$ changes by only $\Delta\,\varphi_R \approx 16°$degrees for the same variation of graphene's carrier density. Likewise, in Figure 8.4 we plot the transmission for two selected wavelengths ($\lambda_T^{PM} = 7.46\mu m$ and $\lambda_T^{AM} = 7.12\mu m$) in the (ϕ_T, T) phase plane. Phase modulation without amplitude change can be achieved in transmission at $\lambda = \lambda_T^{PM}$: the transmission phase $\varphi_T(\lambda_T^{PM})$ varies by almost $\Delta\,\varphi_T \approx 16°$ degrees as the function of n while the transmission amplitude $T(\lambda_T^{PM})$ changes by only 3% for the same variation of carrier density. Similarly, amplitude modulation without phase change can be achieved in transmission at $\lambda = \lambda_T^{AM}$: the transmission amplitude $T(\lambda_T^{AM})$ changes by a factor 3 (from $T = 15\%$ to $T = 45\%$) while the transmission phase $\varphi_T(\lambda_T^{AM})$ changes by only $\Delta\,\varphi_T \approx 7°$ degrees. By controlling both the amplitude and phase of the individual segments of a metasurface, one can now envision actively controlled planar structures capable of forming infrared holograms[62] and infrared scene projectors of almost unlimited complexity operating in either transmission or reflection.

8.4 CONCLUSION

Numerical simulations, can predict the electromagnetic response of an active graphene metasurface. Graphene was modeled with a surface current that depends on the tangential electric fields and graphene optical conductivity from the random phase approximation. The results of the COMSOL multiphysics simulations were in excellent agreement with the experimentally measured reflectivity. The possibility of independent modulation of amplitude and phase was explored for the metasurface used in chapter 4.

Chapter 9: Conclusions and future outlook

In this dissertation, we explored the possibility of active modulation of mid-IR light using graphene-integrated metasurfaces. Graphene`s electronic and optical properties can be tuned by a rate only limited by the circuit`s time constant which makes it an appealing active materials for high-speed optoelectronics. We studied the modulation of amplitude and phase of the mid-IR light by integrating large-area CVD graphene with plasmonic Fano-resonant metasurfaces which enhance the interaction of light with graphene by up to 3000 times. By applying a back-gating scheme, the reflectivity was modulated by 10 dB at around $\lambda = 7\mu m$. A method was proposed to derive the scattering rate of graphene free carriers from the graphene-induced variation of the optical response. It was shown that the proximity of the Fano resonance to the polaritonic resonance of the SiO_2 can increase the quality factor of the resonance.

A Michelson interferometry setup was utilized to measure the phase modulation by graphene. It was shown that the phase can change by $55°$ at $= 7.7\mu m$. In particular the phase can change by $28°$ while the amplitude stays nearly constant which is inspiring for interesting applications in dynamically reconfigurable holograms and beam steering. The setup can be used as an electrically-calibrated laser interferometry system which is able to detect the motion of an object with sub-micron accuracy. Electrical calibration can be potentially ultra-fast as it does not involve moving parts. Using the experimentally measured phase, it was also demonstrated that the polarization state of the reflected light can be modulated via application of a gate voltage for an incident polarization along 45 degree. This is due to the anisotropic response of the metasurface which only changes the phase for the Y-polarized incident light and not for the X-polarized light.

An electrically-connected metasurface was employed to enhance the responsivity of a metasurface-based graphene photodetector. COMSOL simulation showed that the metasurface increases the graphene absorption from 2% to 40%, while 20% is absorbed in the gap between the drain and source and can be collected efficiently. From an electrostatic simulation, the resistance between the drain and source electrodes was calculated for each unit cell. From circuit theory, an analytic relation for the responsivity of the metasurface-based photodetector was derived. A comparison between a bare-graphene photodetector with a metasurface-based graphene photodetector quantified the performance improvement. Addition of the metasurface improved the photoconductive gain dramatically, which is due to improvement in collection efficiency. This leads to the overall responsivity improvement of ≈ 30000 times.

- One challenge in prototyping and commercialization of the devices presented in this dissertation is the large gate voltages. Future works should be aimed at reducing the gate voltage. One possibility to explore is using a high-k dielectric spacer between the graphene and conductive substrates.

- We were able to achieve $55°$ phase shift which is impressive for a monolayer of active material. However, for advanced applications like beam-steering and dynamic holography a 2π phase shift is necessary. Moreover, the insertion loss was too large (10dB). This calls for better designs that allow 2π phase modulations while keeping the insertion loss at reasonable values.

Appendix A: Nanofabrication processes and recipes:

A.1 SAMPLE FABRICATION PROCESS

The nanofabrication process of the devices covered in this dissertation have been performed in Pickle clean room facilities in university of Texas at Austin. In this appendix, we first review the steps of nanofabrication of graphene-integrated metasurface. Then we provide the detailed recipe for each step.

1. The process starts with e-beam lithography of alignment marks on top of a 2×2 cm^2 sample of Si/SiO$_2$. The lithography defines 4 large alignment marks on the 4 sides of the sample at $(-7.5,0), (7.5,0), (0,-7.5)$ and $(0,-7.5)$ all dimensions in millimeters. Each alignment mark is a cross of two wires with the length and width of $L = 1.5mm$ and $W = 3\mu m$. An array of small crosses $L = 15\mu m$ and $W = 3\mu m$ is defined on an area of $10mm \times 10mm$ in the middle of the sample. The distance between any two small cross are $500\mu m$ in both directions.

2. A CVD graphene patch with the approximate size of $1 \times 1\ cm^2$ is transferred onto the middle of the Si/SiO$_2$ sample. The recipe for the growth and transfer of the CVD graphene is provided in appendix B.

3. An e-beam lithography step, masks large patches of high-quality graphene (areas without ripples, cracks and large area defects sites) of $100 \times 100\mu m^2$ or larger and exposes the area surrounding patch. In Fig. 1A a high-quality graphene patch of $250 \times 250\mu m^2$ is masked by an ebeam-lithography step. The green areas are covered with PMMA resist. The area surrounding the patch are exposed with electron beam green and developed thereby are not covered with resist.

4. An oxygen plasma cleaning step cleans the graphene on the exposed part resulting in isolated patches of high-quality graphene. The power and and oxygen flow rates are set to 70 Watts and 20 sccm respectively. The process time was chosen to be 10 seconds.

5. The PMMA is removed with acetone.

6. An e-beam lithography step is used to fabricate the metasurface.

7. Another e-beam lithography step defines the large drain and source contacts. For photodetector structure of chapter 6, the extended drain and source wires were exposed in the same exposure with metasurface. The large contacts were subsequently exposed on top of these extended wires.

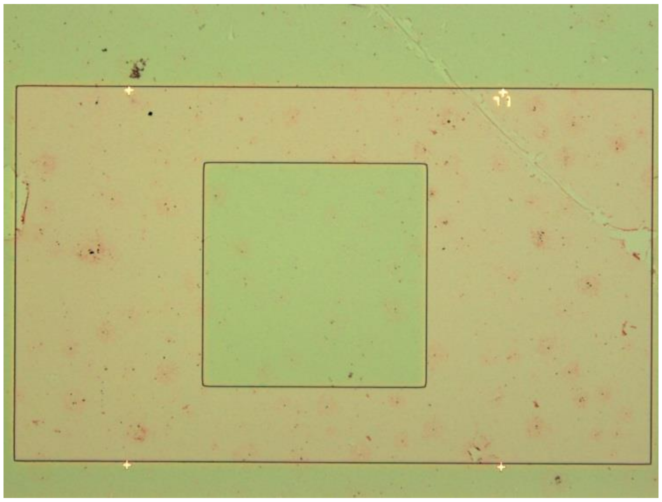

Figure 1A: A high-quality graphene area (the green rectangle) is masked using an e-beam lithography step which follows by an oxygen plasma cleaning step which defines a rectangular isolated graphene patch.

8. The sample is mounted on a chip carrier using an adhesion layer of silver paste.

9. The drain and source contacts of each device are wire-bonded to the separate contact pads of the chip carrier.

10. The chip carrier is mounted on a Faraday cage shown in Fig 2A to protect the graphene devices against electrostatic discharge. Several BNC female connectors are provided to carry the drain, source and gates signals to the voltage source/parametric analyzer.

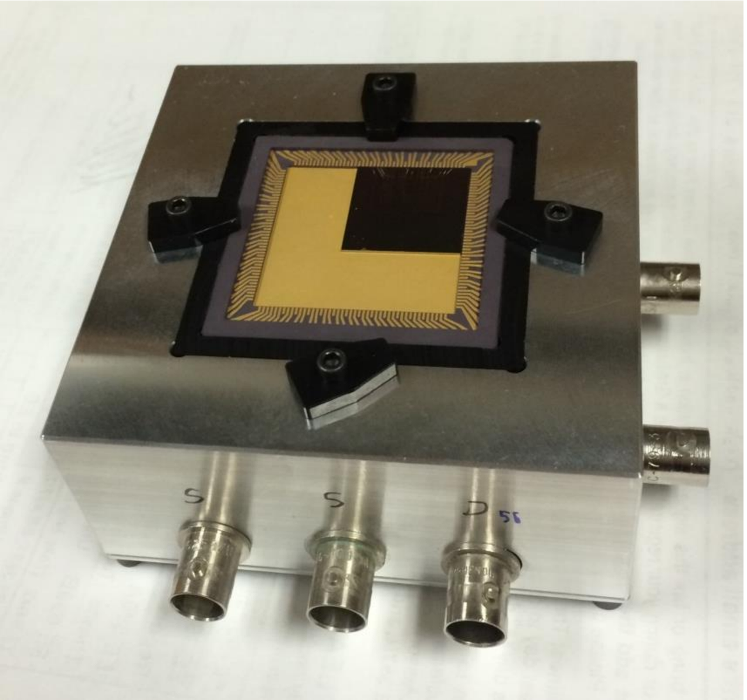

Figure 2A. The bird view of the sample mounted on a chip carrier which is fixed to a Faraday cage. The sample is on the top right corner of the chip carrier and it is wire-bonded to contact pads of the chip carrier. Four black plastic arms clamp the chip carrier to the Faraday cage. Several female BNC connections are provided to carry the signals to the voltage source/parametric analyzer.

A.2 NANOFABRICATION PROCESS

The nanofabrication process is summarized in the schematic in Fig. 3A:

(a) The process starts with spin coating of a Poly(methyl methacrylate) PMMA resist on the substrate (Si/SiO_2/Graphene).
(b) Next the electron beam exposes the targeted area followed by a development step which will define a groove in the exposed regions as depicted in Fig A3(b).
(c) An adhesion layer (Cr/Ti) followed by a noble metal (Au/Ag) are deposited in the ordered mentioned.
(d) The sample is immersed in acetone for several hours which solves the PMMA. Thereby the gold adhering to the PMMA is lifted.

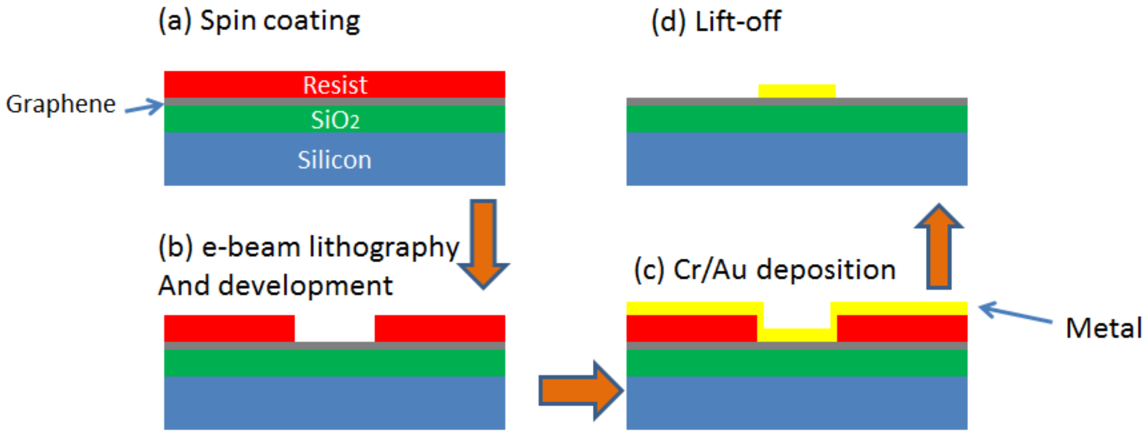

Figure 3A: Steps of nanofabrication process. Step (a)-(d) are used for fabrication of all the samples in this dissertation. The recipe creates graphene-integrated metasurface devices.

We next detail the fabrication recipe for the metasurfaces, crosses and the contacts.

A.3 ELECTRON-BEAM LITHOGRAPHY

A JEOL JBX-6000FS electron-beam lithography (EBL) system was used for all the fabrications in this dissertation. The machine has an accelerating voltage of 50 KV and is capable of patterning 20 nm features for PMMA resist. It incorporates two different objective lenses with maximum field size of 80 and 800 microns respectively.

A.4 NANOFABRICATION RECIPE

(a) Spin coating

Metasurface and crosses: The resist PMMA 950k C2 was spun at 5000 rpm for 1 min followed by a post-bake at 180° for 2 minutes.

Large contact pads:
The resist PMMA 495k A4 was spun at 2000 rpm for 1 min followed by a post-bake at 180° for 2 minutes.

(b) Electron-beam lithography and development

Metasurface and crosses: The exposure current was chosen to be 100PA with dosage of $600\mu C/cm^2$. The development time was 90 seconds and the developer MIBK:IPA (1:3) was kept at 4°.

Large contact pads:
The exposure current was chosen to be 15NA with dosage of $550\mu C/cm^2$. The development time was 40 seconds and developer MIBK:IPA (1:3) was kept at room temperature.

(c) Metallic deposition

The adhesion layer was deposited at the rate of 0.1 A/s (Angstrom per second). For deposition of gold the deposition rate of 0.5 A/s was not exceeded to avoid high temperature in the deposition chamber which would deform the PMMA resist and damage the underlying graphene.

(d) Lift-off

The sample was left in the acetone at room temperature for at least 2 hours. For faster lift-off time, the acetone was put on a hotplate at 45° for at least 15 minutes or until the lift-off is complete. For the photodetector metasurface of chapter 6, due to connectivity of the metasurface in both direction, the sample was sonicated for a few seconds before being removed from acetone to complete the lift-off.

Appendix B: CVD graphene synthesis and transfer[2]

B1. SYNTHESIS

Monolayer graphene was grown on 25-µm thick polycrystalline Cu foils in a hot wall furnace consisting of a 22-mm internal diameter quartz tube heated in a tube furnace. Typically the growth process is composed of the following steps: i) loading the Cu foil into the quartz tube, evacuate, back fill with hydrogen, heat to 1000 °C and maintain a H_2 pressure of 40 mTorr under a 2 sccm flow; ii) stabilize the Cu film at the desired temperatures, up to 1030 °C, and introduce 35 sccm of CH_4 flow for 10 min at a total pressure of 500 mTorr; iii) after exposure to CH_4, the furnace was cooled down to room temperature with rate of 50 °C/min[93].

B2. TRANSFER

The transfer of graphene onto the target substrate (quartz substrate with metamaterial patterns) was performed using dry transfer method that allows to avoid trapping the solutions (used in the transfer processes) between metamolecules, as described elsewhere[126] . Briefly, a poly-(methyl methacrylate) (PMMA) was spin coated (3500 rpm, 1 min) on top of the graphene/Cu foil. A polydimethylsiloxane (PDMS) frame with a hole of about 0.5×0.5 cm^2 size in the center was attached to the top of the graphene/Cu foils. After etching the Cu foil in 0.1 M ammonium persulfate solution, the PDMS/PMMA/graphene system was dried in air and put onto the target substrate. After removing the PDMS mechanically, the sample was put in a vacuum desiccator overnight in order to have better adhesion of graphene to the substrate. Afterwards, PMMA was removed by submerging the sample into acetone. The final graphene/substrate was dries in a vacuum desiccator overnight, and used for spectroscopy measurements.

---

[2] Thanks to Iskandar kholmanov from department of mechanical engineering for the systhesis and transfer of CVD for all the projects in this dissertation and who also provided the recipe detailed in appendix B.

Appendix C: Alignment procedure for the interferometric setup

Fig. C1 shows the steps involved in the alignment procedure. All the optical components have been introduced in the caption at the bottom of the figure. In all the steps, components with the orange color is being aligned while the other component are still. Starting from top left here is the list of steps:

- The Optical path of the laser beam has to be aligned to the optical table. We used two pin-hole far away from each other. (around 2 meters away) One close to the laser and one close to the sample position. We adjusted the height of them to 7 inches and fixed them to the same row of holes on the optical table. We then put the IR camera after the second pinhole on the sample side. By adjusting the height and orientation of the laser, the beam will pass through the center both of the pin-holes producing concentric beams in the IR camera.

- The beam-splitter is inserted in the desired space between the two pin-holes. The IR camera is placed approximately in the right position so that the splitted beam (in arm1) is normal to the original beam. The azimuthal angle of the beam-splitter is adjusted so that the beam is observed in the center of the camera. This gives us an approximate 45 degree.

- A pin-hole is inserted into arm1 and adjusted to the center of the beam by producing concentric pattern in the camera.

- The camera is relocated to the detector position. A mirror on a motorized stage is inserted into arm1. The mirror has to be aligned with the pinhole making sure that the beam is reflected from the mirror in the exact same direction toward the pinhole and the camera. By opening and closing the pin-hole we can test this with the help of the camera.

- Arm 1 is blocked by absorbing material. A mirror is inserted into arm2. Both mirrors should be at the same distance from the beam-slitter. The mirror is aligned with the beam with the help of the pin hole and the camera.

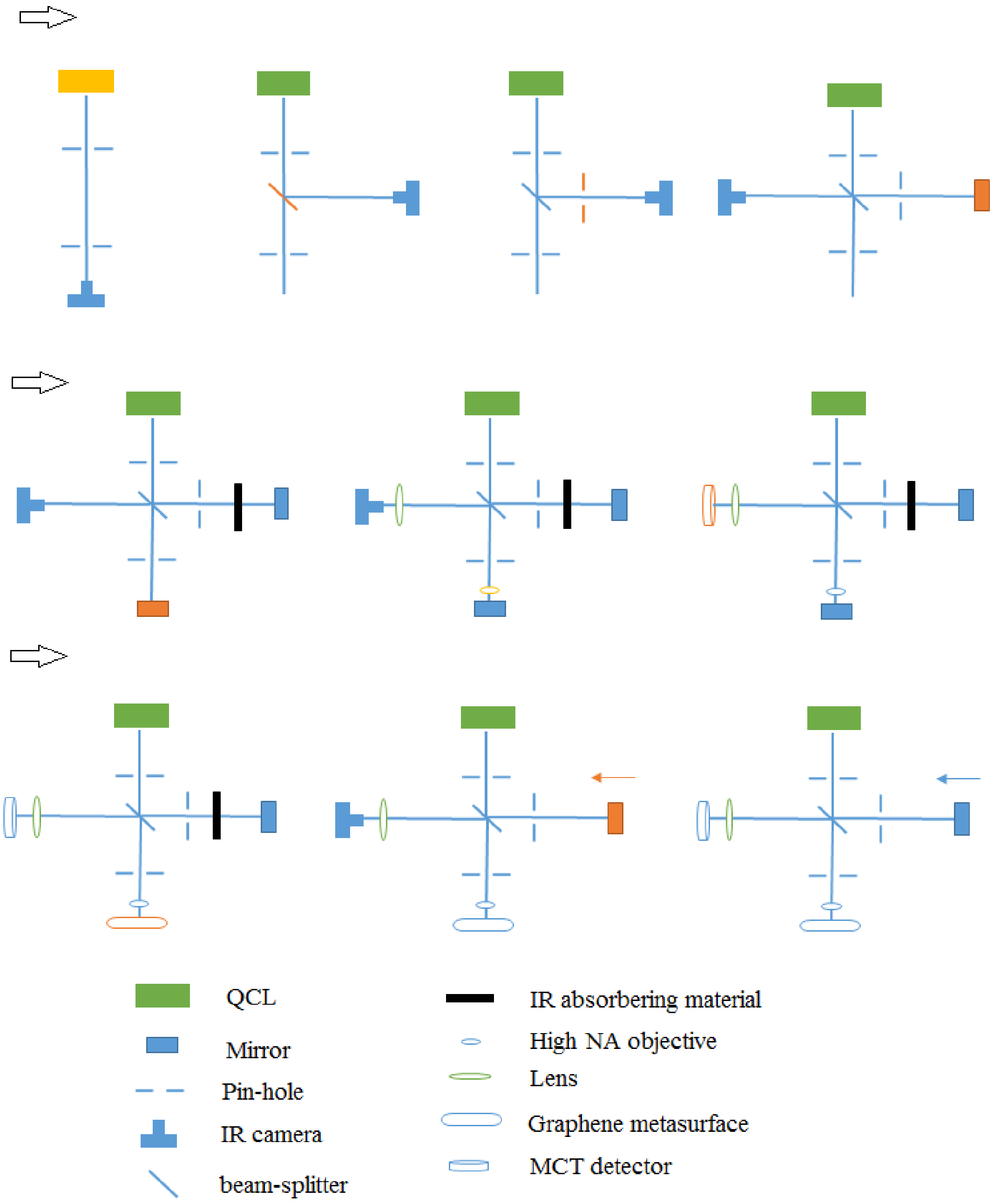

Figure C1: The steps for alignment of a Michelson interferometry setup used in chapter 5. The starting point is from top-left. The arrows show the order of progress. All the optical elements are introduced in the bottom caption. In each step, the element with the orange color is active or is getting aligned while the other components are passive and still.

- A lens is inserted 4 inches from the camera. This is the focal length of the lens. This will not affect out alignment. Next a high numerical objective from ZnSe is inserted around 5mm away from the mirror on arm2. The objective is mounted on a XYZ translation stage with standard micrometers. The objective is aligned to the center of the beam by observing complete circles in the camera in both X and Y translation directions.

- A MCT detector is placed in the focal point of the lens and aligned with the beam by maximizing the measured intensity.

- The graphene metasurface sample is placed in the focal point of the objective. The sample is mounted on a XYZ translation stage with standard micrometers. At this point we focus on the Si/SiO2 substrate surface at 9 micron due to high reflectivity at that SiO2 phonon resonance. We align the sample to the beam by maximizing the measured intensity in the detector.

- By removing the IR absorbing material from arm1, we now use the camera to check the alignment of the reflected beams in arm1 and arm2. By moving the motorized mirror, we should observe interference which is modulation of beam intensity as the mirror is moving. If the modulation is weak then the above steps should be iterated.

- The MCT detector is inserted back and the intensity is measured as a function of mirror position. A good alignment results in large modulation depth of the signal. It should be noted that our laser beam slightly shifts as the wavelength is changing. So for each wavelength alignment should be repeated.

Figure C2 shows the actual setup. A flip mirror was used after the QCL for practical purposes. The graphene sample and the objective are not inserted in the setup yet.

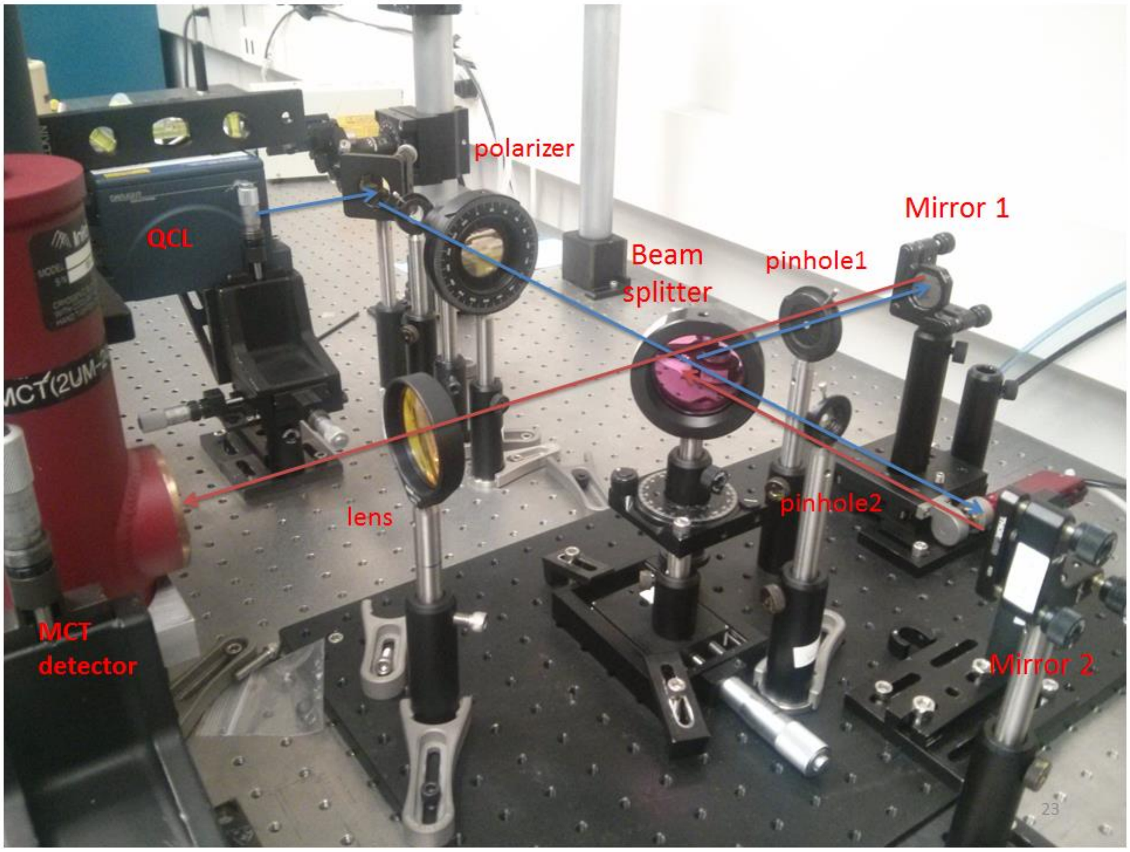

Figure C2: Picture of the setup. All the optical elements are tagged. This is not the final setup and the graphene metasurface, the camera and the objective are not in the setup. But it shows the interferometric Michelson setup with beam splitter, pinholes and mirrors on the two arms.

In Fig C3, the IR camera pictures of the interfered beam for a good and a bad alignment is shown with their corresponding modulation pattern.

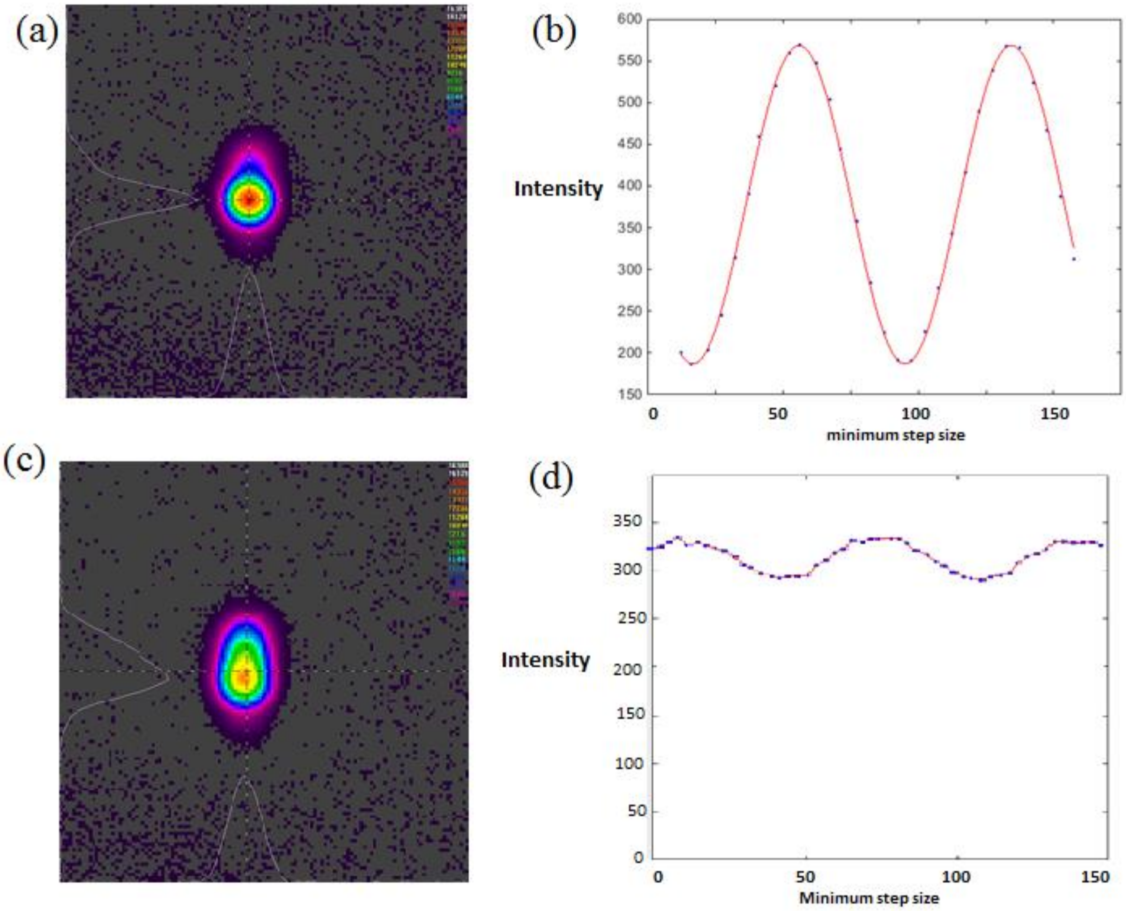

Figure C3: (a,b)The IR camera picture of the interfered beam and the intensity modulation for well aligned beam. A well-rounded pattern is observed in the camera and the modulation depth of the measured intensity as a function of mirror position is large. (c,d) the asymmetric beam and low modulation depth are indicators of poor alignment.

A symmetric interference beam of Fig C3a leads to large modulation depth of Fig. C3b and an asymmetric beam of Fig. C3c leads to small modulation depth of Fig C3d.

Appendix D: Calculation of graphene mobility and carrier collisional times from the electrical transport measurement

Here we provide two different methods that were used to calculate the graphene electrical properties from the transport measurement for samples studied in chapter 4 (section D1) and 5 (section D2). In Fig. D1a the schematic of a graphene-integrated metasurface device is shown with drain, source and backgate contacts and a gate voltage applied between source and back-gate. Figure D1b demonstrates the SEM image of such device. The blue arrows are pointing at graphene edges.

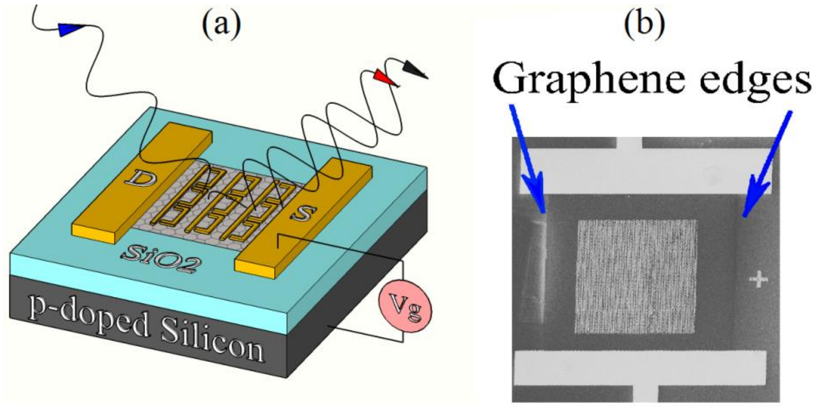

Figure D1: (a) The schematic of a graphene-integrated metasurface device with drain and source and gate connected between source and silicon back-gate. (b) SEM image of a graphene-integrated metasurface device. Graphene edges are marked by blue arrows.

D1: In this section, we calculate the mobility and carrier collisional time as well as the residual charge from the transport measurement data of Fig. D2. The hole mobility μ_h of graphene at room temperature was calculated from the measured electrical conductivity according to $\mu_h = \sigma(n_h)/n_h e \approx 3800\ cm^2/Vs$ where $\sigma(n_h)$ is the electrical conductivity of graphene at the hole concentration of n_h. We used $n_h = 4.8e12\ cm^{-2}$ for this calculation. It should be noted that this calculation ignores the contact resistance between graphene and source/drain which for this case is a good approximation since the contact resistance between chromium and graphene is relatively small compared to graphene resistance. We will calculate this contact resistance in section D2 using a fitting method.

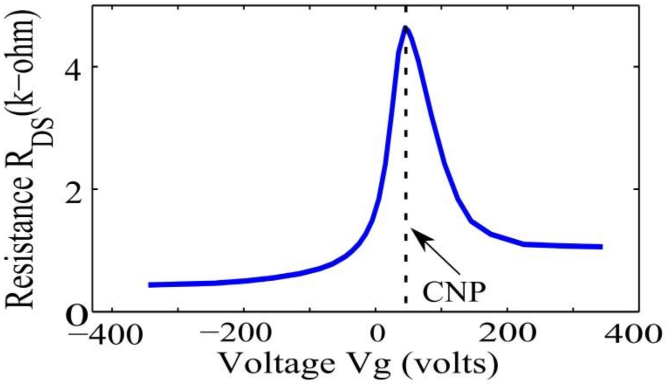

Figure D2: The resistance between the drain and source for the graphene-integrated metasurface device of chapter 4**.**

The carrier collisional time can also be calculated[86] from the measured dc electrical conductivity to be $\tau = \frac{\sigma \hbar^2}{2e^2 E_F} \approx 14 fs$ which is consistent with the value of τ derived using the optical conductivity of graphene as explained in chapter 7. The residual charges at the CNP point was calculated from $n_0 = \frac{\sigma_0 n_{imp} h}{20e^2} = 0.46e12\ cm^{-2}$ where σ_0 is the minimum conductivity from the DC transport measurement and n_{imp} is the SiO2 substrate charge impurity which can be roughly estimated from the graphene mobility[86]. The slight p-doping of the SLG by the SiO_2 substrate is inferred from $V_{CNP} > 0$.

D2: In section D1, the graphene electric properties was calculated directly from the values of resistance at certain Fermi energies. However this approach neglects the contact resistance which is the resistance between graphene and the source/drain contacts. In this section, we derive all the electronic parameters of graphene from fitting to the transport measurement curve.

This approach takes the contact resistance into account. This resistance can be written as [116]: $R_{DS}(V_g) = R_c + R_g = R_c + N_{sq}/e.\mu_h.\sqrt{n_0^2 + [c_g(V_g - V_{CNP})]^2}$ where $N_{sq} = L_g/W_g$ with L_g and W_g being the length and the width of graphene channel.

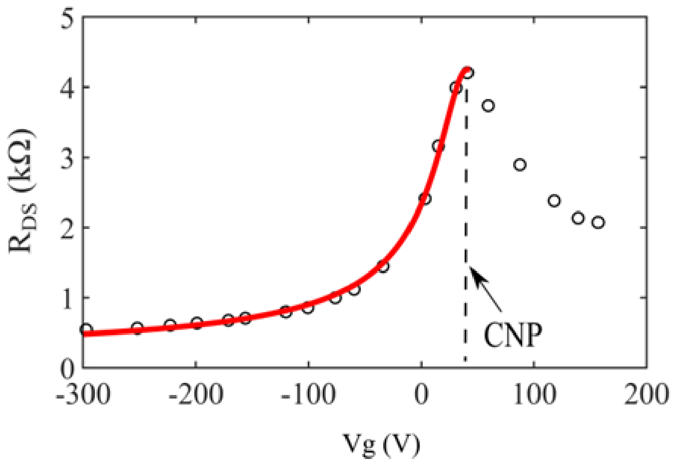

Figure D3: The resistance between the drain and source for the graphene-integrated metasurface device of chapter 5. The red line is the fitting used to determine the contact resistance, mobility and residual charges.

By fitting the experimentally measured resistance in Fig. D3 to R_{DS}, the fitting parameters $R_c = 170\,\Omega$, $n_0 = 4.7e^{11}\ \text{cm}^{-2}$ and $\mu_h = 3600\ \text{cm}^2/\text{Vs}$ can be derived. The charge neutrality point (CNP) $V_g = V_{CNP} = 40\text{V}$ corresponding to $n = n_0$ is identified by the maximum value of $\mathrm{R_{DS}(V_g)}$. The slight p-doping of the SLG by the SiO2 substrate is inferred from $\mathrm{V_{CNP}} > 0$. Due to the breakdown voltage of silicon dioxide at 0.5 GV/m, we vary the back gate voltage in the $-280\mathrm{V} < \mathrm{V_g} < 40\mathrm{V}$ range using "Heathkit 500V PS-3" power supply. The holes' areal concentration can reach the maximum values of $\mathrm{n_h^{max}} \approx 4.0\mathrm{e}12\ \mathrm{cm^{-2}}$ for the peak gate voltage. The red curve in Fig D3 demonstrates the fitted line in the hole regime. The carrier collisional time can be calculated from mobility from $\tau = \frac{\sigma_h \hbar^2}{2e^2 E_F} \approx 13\mathrm{fs}$ where $\sigma_h = n_h e \mu_h$ is the hole conductivity.

References

(1) Pendry, J. B.; Holden, A. J.; Robbins, D. J.; Stewart, W. J. Magnetism from Conductors and Enhanced Nonlinear Phenomena. *IEEE Trans. Microw. Theory Tech.* **1999**, *47*, 2075–2084.

(2) Veselago, V. G. THE ELECTRODYNAMICS OF SUBSTANCES WITH SIMULTANEOUSLY NEGATIVE VALUES OF ϵ AND M. *Sov. Phys. Uspekhi* **1968**, *10* (4), 509–514.

(3) Shelby, R. A.; Smith, D. R.; Schultz, S. Experimental Verification of a Negative Index of Refraction. *Science* **2001**, *292* (5514), 77–79.

(4) Pendry, J. B. Negative Refraction Makes a Perfect Lens. *Phys. Rev. Lett.* **2000**, *85* (18), 3966–3969.

(5) Shalaev, V. M.; Cai, W.; Chettiar, U. K.; Yuan, H.-K.; Sarychev, A. K.; Drachev, V. P.; Kildishev, A. V. Negative Index of Refraction in Optical Metamaterials. *Opt. Lett.* **2005**, *30* (24), 3356.

(6) Holloway, C. L.; Kuester, E. F.; Gordon, J. A.; O'Hara, J.; Booth, J.; Smith, D. R. An Overview of the Theory and Applications of Metasurfaces: The Two-Dimensional Equivalents of Metamaterials. *IEEE Antennas Propag. Mag.* **2012**, *54* (2), 10–35.

(7) Kildishev, A. V.; Boltasseva, A.; Shalaev, V. M. Planar Photonics with Metasurfaces. *Science* **2013**, *339* (6125), 1232009.

(8) Yu, N.; Genevet, P.; Kats, M. A.; Aieta, F.; Tetienne, J.-P.; Capasso, F.; Gaburro, Z. Light Propagation with Phase Discontinuities: Generalized Laws of Reflection and Refraction. *Science* **2011**, *334* (6054), 333–337.

(9) Wu, C.; Khanikaev, A. B.; Shvets, G. Broadband Slow Light Metamaterial Based on a Double-Continuum Fano Resonance. *Phys. Rev. Lett.* **2011**, *106* (10), 107403.

(10) Spinelli, P.; Verschuuren, M. A.; Polman, A. Broadband Omnidirectional Antireflection Coating Based on Subwavelength Surface Mie Resonators. *Nat. Commun.* **2012**, *3*, 692.

(11) Gansel, J. K.; Thiel, M.; Rill, M. S.; Decker, M.; Bade, K.; Saile, V.; Freymann, G. von; Linden, S.; Wegener, M. Gold Helix Photonic Metamaterial as Broadband Circular Polarizer. *Science* **2009**, *325* (5947), 1513–1515.

(12) Zhao, Y.; Belkin, M. A.; Alù, A. Twisted Optical Metamaterials for Planarized Ultrathin Broadband Circular Polarizers. *Nat. Commun.* **2012**, *3*, 870.

(13) Liu, N.; Tang, M. L.; Hentschel, M.; Giessen, H.; Alivisatos, A. P. Nanoantenna-Enhanced Gas Sensing in a Single Tailored Nanofocus. *Nat. Mater.* **2011**, *10* (8), 631–636.

(14) Wu, C.; Khanikaev, A. B.; Adato, R.; Arju, N.; Yanik, A. A.; Altug, H.; Shvets, G. Fano-Resonant Asymmetric Metamaterials for Ultrasensitive Spectroscopy and Identification of Molecular Monolayers. *Nat. Mater.* **2011**, *11* (1), 69–75.

(15) Hao, F.; Sonnefraud, Y.; Dorpe, P. V.; Maier, S. A.; Halas, N. J.; Nordlander, P. Symmetry Breaking in Plasmonic Nanocavities: Subradiant LSPR Sensing and a Tunable Fano Resonance. *Nano Lett.* **2008**, *8* (11), 3983–3988.

(16) Barth, A.; Zscherp, C. What Vibrations Tell about Proteins. *Q. Rev. Biophys.* **2002**, *35* (04), 369–430.

(17) Adato, R.; Yanik, A. A.; Amsden, J. J.; Kaplan, D. L.; Omenetto, F. G.; Hong, M. K.; Erramilli, S.; Altug, H. Ultra-Sensitive Vibrational Spectroscopy of Protein Monolayers

with Plasmonic Nanoantenna Arrays. *Proc. Natl. Acad. Sci.* **2009**, *106* (46), 19227–19232.

(18) Zhang, Y.; Wen, F.; Zhen, Y.-R.; Nordlander, P.; Halas, N. J. Coherent Fano Resonances in a Plasmonic Nanocluster Enhance Optical Four-Wave Mixing. *Proc. Natl. Acad. Sci.* **2013**, *110* (23), 9215–9219.

(19) Klein, M. W.; Enkrich, C.; Wegener, M.; Linden, S. Second-Harmonic Generation from Magnetic Metamaterials. *Science* **2006**, *313* (5786), 502–504.

(20) Liu, X.; Tyler, T.; Starr, T.; Starr, A. F.; Jokerst, N. M.; Padilla, W. J. Taming the Blackbody with Infrared Metamaterials as Selective Thermal Emitters. *Phys. Rev. Lett.* **2011**, *107* (4), 045901.

(21) Aieta, F.; Genevet, P.; Kats, M. A.; Yu, N.; Blanchard, R.; Gaburro, Z.; Capasso, F. Aberration-Free Ultrathin Flat Lenses and Axicons at Telecom Wavelengths Based on Plasmonic Metasurfaces. *Nano Lett.* **2012**, *12* (9), 4932–4936.

(22) Memarzadeh, B.; Mosallaei, H. Array of Planar Plasmonic Scatterers Functioning as Light Concentrator. *Opt. Lett.* **2011**, *36* (13), 2569–2571.

(23) Yu, N.; Aieta, F.; Genevet, P.; Kats, M. A.; Gaburro, Z.; Capasso, F. A Broadband, Background-Free Quarter-Wave Plate Based on Plasmonic Metasurfaces. *Nano Lett.* **2012**, *12* (12), 6328–6333.

(24) Ni, X.; Emani, N. K.; Kildishev, A. V.; Boltasseva, A.; Shalaev, V. M. Broadband Light Bending with Plasmonic Nanoantennas. *Science* **2012**, *335* (6067), 427–427.

(25) Jones, B. F.; Plassmann, P. Digital Infrared Thermal Imaging of Human Skin. *IEEE Eng. Med. Biol. Mag.* **2002**, *21* (6), 41–48.

(26) Merlot, S.; Mustilli, A.-C.; Genty, B.; North, H.; Lefebvre, V.; Sotta, B.; Vavasseur, A.; Giraudat, J. Use of Infrared Thermal Imaging to Isolate Arabidopsis Mutants Defective in Stomatal Regulation. *Plant J.* **2002**, *30* (5), 601–609.

(27) Kosterev, A. A.; Tittel, F. K.; Kohler, R.; Gmachl, C.; Capasso, F.; Sivco, D. L.; Cho, A. Y.; Wehe, S.; Allen, M. G. Thermoelectrically Cooled Quantum-Cascade-Laser-Based Sensor for the Continuous Monitoring of Ambient Atmospheric Carbon Monoxide. *Appl. Opt.* **2002**, *41* (6), 1169–1173.

(28) Fernandez, D. C.; Bhargava, R.; Hewitt, S. M.; Levin, I. W. Infrared Spectroscopic Imaging for Histopathologic Recognition. *Nat. Biotechnol.* **2005**, *23* (4), 469–474.

(29) Bekman, H. H. P. T.; van den Heuvel, J. C.; van Putten, F. J. M.; Schleijpen, R. Development of a Mid-Infrared Laser for Study of Infrared Countermeasures Techniques; 2004; Vol. 5615, pp 27–38.

(30) Bauer, C.; Geiser, P.; Burgmeier, J.; Holl, G.; Schade, W. Pulsed Laser Surface Fragmentation and Mid-Infrared Laser Spectroscopy for Remote Detection of Explosives. *Appl. Phys. B* **2006**, *85* (2-3), 251–256.

(31) Yao, Y.; Hoffman, A. J.; Gmachl, C. F. Mid-Infrared Quantum Cascade Lasers. *Nat. Photonics* **2012**, *6* (7), 432–439.

(32) Rogalski, A. Recent Progress in Infrared Detector Technologies. *Infrared Phys. Technol.* **2011**, *54* (3), 136–154.

(33) Gunapala, S. D.; Bandara, S. V.; Liu, J. K.; Mumolo, J. M.; Ting, D. Z.; Hill, C. J.; Nguyen, J.; Simolon, B.; Woolaway, J.; Wang, S. C.; Li, W.; LeVan, P. D.; Tidrow, M. Z. 1024 × 1024 Format Pixel Co-Located Simultaneously Readable Dual-Band QWIP Focal Plane. *Infrared Phys. Technol.* **2009**, *52* (6), 395–398.

(34) Rogalski, A. Progress in Focal Plane Array Technologies. *Prog. Quantum Electron.* **2012**, *36* (2–3), 342–473.

(35) Haus, H. *Waves and Fields in Optoelectronics*; Prentice-hall, 1984.

(36) Kossyrev, P. A.; Yin, A.; Cloutier, S. G.; Cardimona, D. A.; Huang, D.; Alsing, P. M.; Xu, J. M. Electric Field Tuning of Plasmonic Response of Nanodot Array in Liquid Crystal Matrix. *Nano Lett.* **2005**, *5* (10), 1978–1981.

(37) Berthelot, J.; Bouhelier, A.; Huang, C.; Margueritat, J.; Colas-des-Francs, G.; Finot, E.; Weeber, J.-C.; Dereux, A.; Kostcheev, S.; Ahrach, H. I. E.; Baudrion, A.-L.; Plain, J.; Bachelot, R.; Royer, P.; Wiederrecht, G. P. Tuning of an Optical Dimer Nanoantenna by Electrically Controlling Its Load Impedance. *Nano Lett.* **2009**, *9* (11), 3914–3921.

(38) Xu, G.; Huang, C.-M.; Tazawa, M.; Jin, P.; Chen, D.-M. Nano-Ag on Vanadium Dioxide. II. Thermal Tuning of Surface Plasmon Resonance. *J. Appl. Phys.* **2008**, *104* (5), 053102.

(39) Huang, F.; Baumberg, J. J. Actively Tuned Plasmons on Elastomerically Driven Au Nanoparticle Dimers. *Nano Lett.* **2010**, *10* (5), 1787–1792.

(40) Abb, M.; Albella, P.; Aizpurua, J.; Muskens, O. L. All-Optical Control of a Single Plasmonic Nanoantenna–ITO Hybrid. *Nano Lett.* **2011**, *11* (6), 2457–2463.

(41) Kim, J.; Son, H.; Cho, D. J.; Geng, B.; Regan, W.; Shi, S.; Kim, K.; Zettl, A.; Shen, Y.-R.; Wang, F. Electrical Control of Optical Plasmon Resonance with Graphene. *Nano Lett.* **2012**, *12* (11), 5598–5602.

(42) Majumdar, A.; Kim, J.; Vuckovic, J.; Wang, F. Electrical Control of Silicon Photonic Crystal Cavity by Graphene. *Nano Lett.* **2013**, *13* (2), 515–518.

(43) Jun, Y. C.; Gonzales, E.; Reno, J. L.; Shaner, E. A.; Gabbay, A.; Brener, I. Active Tuning of Mid-Infrared Metamaterials by Electrical Control of Carrier Densities. *Opt. Express* **2012**, *20* (2), 1903–1911.

(44) Tang, L.; Kocabas, S. E.; Latif, S.; Okyay, A. K.; Ly-Gagnon, D.-S.; Saraswat, K. C.; Miller, D. A. B. Nanometre-Scale Germanium Photodetector Enhanced by a near-Infrared Dipole Antenna. *Nat. Photonics* **2008**, *2* (4), 226–229.

(45) Ooi, K. J. A.; Bai, P.; Chu, H. S.; Ang, L. K. Vandium Dioxide Active Plasmonics. In *Photonics Global Conference (PGC), 2012*; 2012; pp 1–4.

(46) Bai, P.; Gu, M.-X.; Wei, X.-C.; Li, E.-P. Electrical Detection of Plasmonic Waves Using an Ultra-Compact Structure via a Nanocavity. *Opt. Express* **2009**, *17* (26), 24349–24357.

(47) Stewart, M. E.; Anderton, C. R.; Thompson, L. B.; Maria, J.; Gray, S. K.; Rogers, J. A.; Nuzzo, R. G. Nanostructured Plasmonic Sensors. *Chem. Rev.* **2008**, *108* (2), 494–521.

(48) Anker, J. N.; Hall, W. P.; Lyandres, O.; Shah, N. C.; Zhao, J.; Van Duyne, R. P. Biosensing with Plasmonic Nanosensors. *Nat. Mater.* **2008**, *7* (6), 442–453.

(49) Liu, N.; Mesch, M.; Weiss, T.; Hentschel, M.; Giessen, H. Infrared Perfect Absorber and Its Application As Plasmonic Sensor. *Nano Lett.* **2010**, *10* (7), 2342–2348.

(50) Lu, Y.-J.; Kim, J.; Chen, H.-Y.; Wu, C.; Dabidian, N.; Sanders, C. E.; Wang, C.-Y.; Lu, M.-Y.; Li, B.-H.; Qiu, X.; Chang, W.-H.; Chen, L.-J.; Shvets, G.; Shih, C.-K.; Gwo, S. Plasmonic Nanolaser Using Epitaxially Grown Silver Film. *Science* **2012**, *337* (6093), 450–453.

(51) Liu, X.; Starr, T.; Starr, A. F.; Padilla, W. J. Infrared Spatial and Frequency Selective Metamaterial with Near-Unity Absorbance. *Phys. Rev. Lett.* **2010**, *104* (20), 207403.

(52) Rizzo, G.; Bettarini, S.; Calderini, G.; Cenci, R.; Forti, F.; Giorgi, M. A.; Morsani, F.; Ratti, L.; Speziali, V.; Manghisoni, M.; Re, V.; Traversi, G.; Bosisio, L. A Novel

Monolithic Active Pixel Detector in Triple Well CMOS Technology with Pixel Level Analog Processing. *Nucl. Instrum. Methods Phys. Res. Sect. Accel. Spectrometers Detect. Assoc. Equip.* **2006**, *565* (1), 195–201.

(53) Sun, B.; Edgar, M. P.; Bowman, R.; Vittert, L. E.; Welsh, S.; Bowman, A.; Padgett, M. J. 3D Computational Imaging with Single-Pixel Detectors. *Science* **2013**, *340* (6134), 844–847.

(54) Pryce, I. M.; Aydin, K.; Kelaita, Y. A.; Briggs, R. M.; Atwater, H. A. Highly Strained Compliant Optical Metamaterials with Large Frequency Tunability. *Nano Lett.* **2010**, *10* (10), 4222–4227.

(55) Chen, H.-T.; Padilla, W. J.; Cich, M. J.; Azad, A. K.; Averitt, R. D.; Taylor, A. J. A Metamaterial Solid-State Terahertz Phase Modulator. *Nat. Photonics* **2009**, *3* (3), 148–151.

(56) Wang, F.; Shen, Y. R. General Properties of Local Plasmons in Metal Nanostructures. *Phys. Rev. Lett.* **2006**, *97* (20), 206806.

(57) Mousavi, S. H.; Kholmanov, I.; Alici, K. B.; Purtseladze, D.; Arju, N.; Tatar, K.; Fozdar, D. Y.; Suk, J. W.; Hao, Y.; Khanikaev, A. B.; Ruoff, R. S.; Shvets, G. Inductive Tuning of Fano-Resonant Metasurfaces Using Plasmonic Response of Graphene in the Mid-Infrared. *Nano Lett.* **2013**, *13* (3), 1111–1117.

(58) Yao, Y.; Kats, M. A.; Shankar, R.; Song, Y.; Kong, J.; Loncar, M.; Capasso, F. Wide Wavelength Tuning of Optical Antennas on Graphene with Nanosecond Response Time. *Nano Lett.* **2014**, *14* (1), 214–219.

(59) Yao, Y.; Kats, M. A.; Genevet, P.; Yu, N.; Song, Y.; Kong, J.; Capasso, F. Broad Electrical Tuning of Graphene-Loaded Plasmonic Antennas. *Nano Lett.* **2013**, *13* (3), 1257–1264.

(60) Schurig, D.; Mock, J. J.; Justice, B. J.; Cummer, S. A.; Pendry, J. B.; Starr, A. F.; Smith, D. R. Metamaterial Electromagnetic Cloak at Microwave Frequencies. *Science* **2006**, *314* (5801), 977–980.

(61) Fang, N.; Lee, H.; Sun, C.; Zhang, X. Sub–Diffraction-Limited Optical Imaging with a Silver Superlens. *Science* **2005**, *308* (5721), 534–537.

(62) Larouche, S.; Tsai, Y.-J.; Tyler, T.; Jokerst, N. M.; Smith, D. R. Infrared Metamaterial Phase Holograms. *Nat. Mater.* **2012**, *11* (5), 450–454.

(63) Ni, X.; Kildishev, A. V.; Shalaev, V. M. Metasurface Holograms for Visible Light. *Nat. Commun.* **2013**, *4*.

(64) Tsai, Y.-J.; Larouche, S.; Tyler, T.; Llopis, A.; Royal, M.; Jokerst, N. M.; Smith, D. R. Arbitrary Birefringent Metamaterials for Holographic Optics at Λ = 1.55 Mm. *Opt. Express* **2013**, *21* (22), 26620–26630.

(65) Walther, B.; Helgert, C.; Rockstuhl, C.; Setzpfandt, F.; Eilenberger, F.; Kley, E.-B.; Lederer, F.; Tünnermann, A.; Pertsch, T. Spatial and Spectral Light Shaping with Metamaterials. *Adv. Mater.* **2012**, *24* (47), 6300–6304.

(66) Huang, L.; Chen, X.; Mühlenbernd, H.; Zhang, H.; Chen, S.; Bai, B.; Tan, Q.; Jin, G.; Cheah, K.-W.; Qiu, C.-W.; Li, J.; Zentgraf, T.; Zhang, S. Three-Dimensional Optical Holography Using a Plasmonic Metasurface. *Nat. Commun.* **2013**, *4*.

(67) Raghunathan, S. B.; Schouten, H. F.; Ubachs, W.; Kim, B. E.; Gan, C. H.; Visser, T. D. Dynamic Beam Steering from a Subwavelength Slit by Selective Excitation of Guided Modes. *Phys. Rev. Lett.* **2013**, *111* (15), 153901.

(68) MCLEOD, J. H. The Axicon: A New Type of Optical Element. *J. Opt. Soc. Am.* **1954**, *44* (8), 592–592.

(69) Lee, S. H.; Choi, M.; Kim, T.-T.; Lee, S.; Liu, M.; Yin, X.; Choi, H. K.; Lee, S. S.; Choi, C.-G.; Choi, S.-Y.; Zhang, X.; Min, B. Switching Terahertz Waves with Gate-Controlled Active Graphene Metamaterials. *Nat. Mater.* **2012**, *11* (11), 936–941.

(70) Peng, F.; Chen, H.; Tripathi, S.; Twieg, R. J.; Wu, S.-T. Fast-Response IR Spatial Light Modulators with a Polymer Network Liquid Crystal; 2015; Vol. 9384, p 93840N–93840N–8.

(71) Yao, Y.; Shankar, R.; Rauter, P.; Song, Y.; Kong, J.; Loncar, M.; Capasso, F. High-Responsivity Mid-Infrared Graphene Detectors with Antenna-Enhanced Photocarrier Generation and Collection. *Nano Lett.* **2014**, *14* (7), 3749–3754.

(72) Gabor, N. M.; Song, J. C. W.; Ma, Q.; Nair, N. L.; Taychatanapat, T.; Watanabe, K.; Taniguchi, T.; Levitov, L. S.; Jarillo-Herrero, P. Hot Carrier–Assisted Intrinsic Photoresponse in Graphene. *Science* **2011**, *334* (6056), 648–652.

(73) Du, X.; Prober, D. E.; Vora, H.; Mckitterick, C. B. Graphene-Based Bolometers. *Graphene 2D Mater.* **2014**, *1* (1).

(74) Liu, C.-H.; Chang, Y.-C.; Norris, T. B.; Zhong, Z. Graphene Photodetectors with Ultra-Broadband and High Responsivity at Room Temperature. *Nat. Nanotechnol.* **2014**, *advance online publication*.

(75) Furchi, M.; Urich, A.; Pospischil, A.; Lilley, G.; Unterrainer, K.; Detz, H.; Klang, P.; Andrews, A. M.; Schrenk, W.; Strasser, G.; Mueller, T. Microcavity-Integrated Graphene Photodetector. *Nano Lett.* **2012**, *12* (6), 2773–2777.

(76) Engel, M.; Steiner, M.; Lombardo, A.; Ferrari, A. C.; Löhneysen, H. v; Avouris, P.; Krupke, R. Light–matter Interaction in a Microcavity-Controlled Graphene Transistor. *Nat. Commun.* **2012**, *3*, 906.

(77) Pospischil, A.; Humer, M.; Furchi, M. M.; Bachmann, D.; Guider, R.; Fromherz, T.; Mueller, T. CMOS-Compatible Graphene Photodetector Covering All Optical Communication Bands. *Nat. Photonics* **2013**, *7* (11), 892–896.

(78) Echtermeyer, T. J.; Britnell, L.; Jasnos, P. K.; Lombardo, A.; Gorbachev, R. V.; Grigorenko, A. N.; Geim, A. K.; Ferrari, A. C.; Novoselov, K. S. Strong Plasmonic Enhancement of Photovoltage in Graphene. *Nat. Commun.* **2011**, *2*, 458.

(79) Freitag, M.; Low, T.; Zhu, W.; Yan, H.; Xia, F.; Avouris, P. Photocurrent in Graphene Harnessed by Tunable Intrinsic Plasmons. *Nat. Commun.* **2013**, *4*.

(80) Konstantatos, G.; Badioli, M.; Gaudreau, L.; Osmond, J.; Bernechea, M.; de Arquer, F. P. G.; Gatti, F.; Koppens, F. H. L. Hybrid Graphene-Quantum Dot Phototransistors with Ultrahigh Gain. *Nat. Nanotechnol.* **2012**, *7* (6), 363–368.

(81) Novoselov, K. S.; Geim, A. K.; Morozov, S. V.; Jiang, D.; Zhang, Y.; Dubonos, S. V.; Grigorieva, I. V.; Firsov, A. A. Electric Field Effect in Atomically Thin Carbon Films. *Science* **2004**, *306* (5696), 666–669.

(82) Fallahazad, B. Dielectric-Graphene Integration and Electron Transport in Graphene Hybrid Structures. Thesis, 2015.

(83) Saito, R.; Dresselhaus, G.; Dresselhaus, M. S. *Physical Properties of Carbon Nanotubes*; PUBLISHED BY IMPERIAL COLLEGE PRESS AND DISTRIBUTED BY WORLD SCIENTIFIC PUBLISHING CO., 1998.

(84) Castro Neto, A. H.; Guinea, F.; Peres, N. M. R.; Novoselov, K. S.; Geim, A. K. The Electronic Properties of Graphene. *Rev. Mod. Phys.* **2009**, *81* (1), 109–162.

(85) Chen, J.-H.; Jang, C.; Xiao, S.; Ishigami, M.; Fuhrer, M. S. Intrinsic and Extrinsic Performance Limits of Graphene Devices on SiO2. *Nat. Nanotechnol.* **2008**, *3* (4), 206–209.

(86) Adam, S.; Hwang, E. H.; Galitski, V. M.; Sarma, S. D. A Self-Consistent Theory for Graphene Transport. *Proc. Natl. Acad. Sci.* **2007**, *104* (47), 18392–18397.

(87) Hwang, E. H.; Das Sarma, S. Acoustic Phonon Scattering Limited Carrier Mobility in Two-Dimensional Extrinsic Graphene. *Phys. Rev. B* **2008**, *77* (11), 115449.

(88) Fratini, S.; Guinea, F. Substrate-Limited Electron Dynamics in Graphene. *Phys. Rev. B* **2008**, *77* (19), 195415.

(89) Nair, R. R.; Blake, P.; Grigorenko, A. N.; Novoselov, K. S.; Booth, T. J.; Stauber, T.; Peres, N. M. R.; Geim, A. K. Fine Structure Constant Defines Visual Transparency of Graphene. *Science* **2008**, *320* (5881), 1308–1308.

(90) Falkovsky, L. A.; Pershoguba, S. S. Optical Far-Infrared Properties of a Graphene Monolayer and Multilayer. *Phys. Rev. B* **2007**, *76* (15), 153410.

(91) Dabidian, N.; Mousavi, S. H.; Kholmanov, I.; Alici, K.; Purtseladze, D.; Arju, N.; Tatar, K.; Suk, J. W.; Hao, Y.; Khanikaev, A. B.; others. Dynamic Inductive Tuning of Fano-Resonant Meta-Surfaces Using Plasmonic Response of Graphene in Mid-Infrared. In *Advanced Electromagnetic Materials in Microwaves and Optics (METAMATERIALS), 2013 7th International Congress on*; IEEE, 2013; pp 196–198.

(92) Eletskii, A. V.; Iskandarova, I. M.; Knizhnik, A. A.; Krasikov, D. N. Graphene: Fabrication Methods and Thermophysical Properties. *Phys.-Uspekhi* **2011**, *54* (3), 227–258.

(93) Li, X.; Cai, W.; An, J.; Kim, S.; Nah, J.; Yang, D.; Piner, R.; Velamakanni, A.; Jung, I.; Tutuc, E.; Banerjee, S. K.; Colombo, L.; Ruoff, R. S. Large-Area Synthesis of High-Quality and Uniform Graphene Films on Copper Foils. *Science* **2009**, *324* (5932), 1312–1314.

(94) Fano, U. Effects of Configuration Interaction on Intensities and Phase Shifts. *Phys. Rev.* **1961**, *124* (6), 1866–1878.

(95) Wu, C.; Arju, N.; Kelp, G.; Fan, J. A.; Dominguez, J.; Gonzales, E.; Tutuc, E.; Brener, I.; Shvets, G. Spectrally Selective Chiral Silicon Metasurfaces Based on Infrared Fano Resonances. *Nat. Commun.* **2014**, *5*.

(96) Ruan, Z.; Fan, S. Temporal Coupled-Mode Theory for Fano Resonance in Light Scattering by a Single Obstacle. *J. Phys. Chem. C* **2010**, *114* (16), 7324–7329.

(97) Khanikaev, A. B.; Wu, C.; Shvets, G. Fano-Resonant Metamaterials and Their Applications. *Nanophotonics* **2013**, *2* (4), 247–264.

(98) Tittl, A.; Mai, P.; Taubert, R.; Dregely, D.; Liu, N.; Giessen, H. Palladium-Based Plasmonic Perfect Absorber in the Visible Wavelength Range and Its Application to Hydrogen Sensing. *Nano Lett.* **2011**, *11* (10), 4366–4369.

(99) Dabidian, N.; Kholmanov, I.; Khanikaev, A. B.; Tatar, K.; Trendafilov, S.; Mousavi, S. H.; Magnuson, C.; Ruoff, R. S.; Shvets, G. Electrical Switching of Infrared Light Using Graphene Integration with Plasmonic Fano Resonant Metasurfaces. *ACS Photonics* **2015**, *2* (2), 216–227.

(100) Zhang, S.; Genov, D. A.; Wang, Y.; Liu, M.; Zhang, X. Plasmon-Induced Transparency in Metamaterials. *Phys. Rev. Lett.* **2008**, *101* (4), 047401.

(101) Khanikaev, A. B.; Mousavi, S. H.; Wu, C.; Dabidian, N.; Alici, K. B.; Shvets, G. Electromagnetically Induced Polarization Conversion. *Opt. Commun.* **2012**, *285* (16), 3423–3427.

(102) Adato, R.; Yanik, A. A.; Altug, H. On Chip Plasmonic Monopole Nano-Antennas and Circuits. *Nano Lett.* **2011**, *11* (12), 5219–5226.

(103) Pendry, J. B.; Holden, A. J.; Robbins, D. J.; Stewart, W. J. Low Frequency Plasmons in Thin-Wire Structures. *J. Phys. Condens. Matter* **1998**, *10* (22), 4785.

(104) Artar, A.; Yanik, A. A.; Altug, H. Multispectral Plasmon Induced Transparency in Coupled Meta-Atoms. *Nano Lett.* **2011**, *11* (4), 1685–1689.

(105) Fei, Z.; Rodin, A. S.; Andreev, G. O.; Bao, W.; McLeod, A. S.; Wagner, M.; Zhang, L. M.; Zhao, Z.; Thiemens, M.; Dominguez, G.; Fogler, M. M.; Neto, A. H. C.; Lau, C. N.; Keilmann, F.; Basov, D. N. Gate-Tuning of Graphene Plasmons Revealed by Infrared Nano-Imaging. *Nature* **2012**, *487* (7405), 82–85.

(106) Li, X.; Zhu, Y.; Cai, W.; Borysiak, M.; Han, B.; Chen, D.; Piner, R. D.; Colombo, L.; Ruoff, R. S. Transfer of Large-Area Graphene Films for High-Performance Transparent Conductive Electrodes. *Nano Lett.* **2009**, *9* (12), 4359–4363.

(107) Kholmanov, I. N.; Magnuson, C. W.; Aliev, A. E.; Li, H.; Zhang, B.; Suk, J. W.; Zhang, L. L.; Peng, E.; Mousavi, S. H.; Khanikaev, A. B.; Piner, R.; Shvets, G.; Ruoff, R. S. Improved Electrical Conductivity of Graphene Films Integrated with Metal Nanowires. *Nano Lett.* **2012**, *12* (11), 5679–5683.

(108) Novoselov, K. S.; Geim, A. K.; Morozov, S. V.; Jiang, D.; Katsnelson, M. I.; Grigorieva, I. V.; Dubonos, S. V.; Firsov, A. A. Two-Dimensional Gas of Massless Dirac Fermions in Graphene. *Nature* **2005**, *438* (7065), 197–200.

(109) Martin, J. Observation of Electron-Hole Puddles in Graphene Using a Scanning Single Electron Transistor. *Nat. Phys* **2007**, *4*, 144–148.

(110) Cai, W.; White, J. S.; Brongersma, M. L. Compact, High-Speed and Power-Efficient Electrooptic Plasmonic Modulators. *Nano Lett.* **2009**, *9* (12), 4403–4411.

(111) Barrios, C. A.; de Almeida, V. R.; Lipson, M. Low-Power-Consumption Short-Length and High-Modulation-Depth Silicon Electrooptic Modulator. *J. Light. Technol.* **2003**, *21* (4), 1089–1098.

(112) Chu, H.-S.; How Gan, C. Active Plasmonic Switching at Mid-Infrared Wavelengths with Graphene Ribbon Arrays. *Appl. Phys. Lett.* **2013**, *102* (23), 231107.

(113) Chen, D.-Z. A.; Chen, G. Measurement of Silicon Dioxide Surface Phonon-Polariton Propagation Length by Attenuated Total Reflection. *Appl. Phys. Lett.* **2007**, *91* (12), 121906.

(114) Vassant, S.; Archambault, A.; Marquier, F.; Pardo, F.; Gennser, U.; Cavanna, A.; Pelouard, J. L.; Greffet, J. J. Epsilon-Near-Zero Mode for Active Optoelectronic Devices. *Phys. Rev. Lett.* **2012**, *109* (23), 237401.

(115) Brar, V. W.; Jang, M. S.; Sherrott, M.; Lopez, J. J.; Atwater, H. A. Highly Confined Tunable Mid-Infrared Plasmonics in Graphene Nanoresonators. *Nano Lett.* **2013**, *13* (6), 2541–2547.

(116) Kim, S.; Nah, J.; Jo, I.; Shahrjerdi, D.; Colombo, L.; Yao, Z.; Tutuc, E.; Banerjee, S. K. Realization of a High Mobility Dual-Gated Graphene Field-Effect Transistor with Al2O3 Dielectric. *Appl. Phys. Lett.* **2009**, *94* (6), 062107.

(117) Lee, Y. G.; Kang, C. G.; Cho, C.; Kim, Y.; Hwang, H. J.; Lee, B. H. Quantitative Analysis of Hysteretic Reactions at the Interface of Graphene and SiO2 Using the Short Pulse I–V Method. *Carbon* **2013**, *60*, 453–460.

(118) Woessner, A.; Lundeberg, M. B.; Gao, Y.; Principi, A.; Alonso-González, P.; Carrega, M.; Watanabe, K.; Taniguchi, T.; Vignale, G.; Polini, M.; Hone, J.; Hillenbrand, R.; Koppens, F. H. L. Highly Confined Low-Loss Plasmons in Graphene–boron Nitride Heterostructures. *Nat. Mater.* **2015**, *14* (4), 421–425.

(119) Delfyett, P. J.; Mandridis, D.; Piracha, M. U.; Nguyen, D.; Kim, K.; Lee, S. Chirped Pulse Laser Sources and Applications. *Prog. Quantum Electron.* **2012**, *36* (4–6), 475–540.

(120) Corrigan, P.; Martini, R.; Whittaker, E. A.; Bethea, C. Quantum Cascade Lasers and the Kruse Model in Free Space Optical Communication. *Opt. Express* **2009**, *17* (6), 4355.

(121) Li, Y.-M.; An, I.; Nguyen, H. V.; Wronski, C. R.; Collins, R. W. Thin-Film Coalescence in Hydrogenated Amorphous Silicon Probed by Spectroscopic Ellipsometry with Millisecond-Scale Resolution. *Phys. Rev. Lett.* **1992**, *68* (18), 2814–2817.

(122) Urich, A.; Unterrainer, K.; Mueller, T. Intrinsic Response Time of Graphene Photodetectors. *Nano Lett.* **2011**, *11* (7), 2804–2808.

(123) Rana, F. Electron-Hole Generation and Recombination Rates for Coulomb Scattering in Graphene. *Phys. Rev. B* **2007**, *76* (15), 155431.

(124) Tielrooij, K. J.; Song, J. C. W.; Jensen, S. A.; Centeno, A.; Pesquera, A.; Zurutuza Elorza, A.; Bonn, M.; Levitov, L. S.; Koppens, F. H. L. Photoexcitation Cascade and Multiple Hot-Carrier Generation in Graphene. *Nat. Phys.* **2013**, *9* (4), 248–252.

(125) Palik, E. *Handbook of Optical Constants of Solids*; Academic Press, 1997.

(126) Suk, J. W.; Kitt, A.; Magnuson, C. W.; Hao, Y.; Ahmed, S.; An, J.; Swan, A. K.; Goldberg, B. B.; Ruoff, R. S. Transfer of CVD-Grown Monolayer Graphene onto Arbitrary Substrates. *ACS Nano* **2011**, *5* (9), 6916–6924.